Université d'Ottawa · University of Ottawa

PERMISSION DE REPRODUIRE ET DE DISTRIBUER LA THÈSE

PERMISSION TO REPRODUCE AND DISTRIBUTE THE THESIS

NOM DE L'AUTEUR / NAME OF AUTHOR:	ZENG, Xiaodong
ADRESSE POSTALE / MAILING ADDRESS:	17-362 MCARTHUR AVENUE VANIER ON K1L6N7
GRADE / DEGREE:	**ANNÉE D'OBTENTION / YEAR GRANTED**
M.Sc. (Physics)	2003
TITRE DE LA THÈSE / TITLE OF THESIS: CHARACTERIZATION AND APPLICATION OF BRILLOUIN SCATTERING BASED DISTRIBUTED FIBER OPTIC	

L'auteur permet, par la présente, la consultation et le prêt de cette thèse en conformité avec les règlements établis par le bibliothécaire en chef de l'Université d'Ottawa. L'auteur autorise aussi l'Université d'Ottawa, ses successeurs et cessionnaires, à reproduire cet exemplaire par photograhie ou photocopie pour fins de prêt ou de vente au prix coûtant aux bibliothèques ou aux chercheurs qui en feront la demande.

Les droits de publication par tout autre moyen et pour vente au public demeureront la propriété de l'auteur de la thèse sous réserve des règlements de l'Université d'Ottawa en matière de publication de thèses.

The author hereby permits the consultation and the lending of this thesis pursuant to the regulations established by the Chief Librarian of the University of Ottawa. The author also authorizes the University of Ottawa, its successors and assignees, to make reproductions of this copy by photographic means or by photocopying and to lend or sell such reproductions at cost to libraries and to scholars requesting them.

The right to publish the thesis by other means and to sell it to the public is reserved to the author, subject to the regulations of the University of Ottawa governing the publication of theses.

N.B. LE MASCULIN COMPREND ÉGALEMENT LE FÉMININ

Feb. 19, 2003

DATE

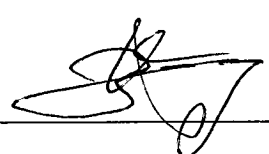

(AUTEUR) SIGNATURE (AUTHOR)

Université d'Ottawa · University of Ottawa

Université d'Ottawa · University of Ottawa

FACULTÉ DES ÉTUDES SUPÉRIEURES ET POSTDOCTORALES

FACULTY OF GRADUATE AND POSTDOCTORAL STUDIES

ZENG, Xiaodong
AUTEUR DE LA THÈSE - AUTHOR OF THESIS

M.Sc. (Physics)
GRADE - DEGREE

Physics
FACULTÉ, ÉCOLE, DÉPARTEMENT - FACULTY, SCHOOL, DEPARTMENT

TITRE DE LA THÈSE - TITLE OF THE THESIS

Characterization and Application of Brillouin Scattering Based Distributed Fiber Optic Sensor

Xiaoyi Bao and Liang Chen
DIRECTEUR DE LA THÈSE - THESIS SUPERVISOR

EXAMINATEURS DE LA THÈSE - THESIS EXAMINERS

T. Brabec

S. Mihailov

J. Armitage

J.-M. De Koninck, Ph.D.
LE DOYEN DE LA FACULTÉ DES ÉTUDES SUPÉRIEURES ET POSTDOCTORALES

SIGNATURE

DEAN OF THE FACULTY OF GRADUATE AND POSTDOCTORAL STUDIES

Characterization and Application of Brillouin Scattering Based Distributed Fiber Optic Sensor

by

Xiaodong Zeng

Thesis submitted to
The Faculty of Graduate and Postdoctoral Studies
in partial fulfillment of the requirements for the Degree of

Master of Science

Ottawa-Carleton Institute for Physics
University of Ottawa
Ottawa, Canada
February 2003

Vita

Full name: Xiaodong Zeng

University attended: Nankai University (Tianjin, China)
B.Sc. (Physics) 1978 – 1982
University of New Brunswick, Jan. – Aug. 2000
University of Ottawa, Aug. 2000 – 2002

Publications:

X. Zeng, X. Bao, C. Y. Chhoa, T. W. Bremner, A. W. Brown, M. D. DeMerchant, G. Ferrier, A. L. Kalamkarov, and A. V. Georgiades, "Strain measurement in a concrete beam using the Brillouin scattering based distributed fiber sensor with single mode fibers embedded in GFRP rod and bonded to steel reinforcing bars", ***Applied Optics*, 41** (24), p. 5105 – 5114 2002.

X. Zeng, Q. Yu, G. Ferrier, and X. Bao, "Strain and temperature monitoring of a concrete structure using a distributed Brillouin scattering sensor", in *proceedings of the 1st International Workshop on Structural Health Monitoring of Innovative Civil Engineering Structures,* Winnipeg, Canada, in print 2002.

X. Zeng, Q. Yu, G. Ferrier, X. Bao, R. E. Steffen, and M. Bowman, "Strain Measurement of the Load Test on the Rollinsford Bridge Using the Distributed Brillouin Sensor", *1st International Workshop on Structural Health Monitoring of Innovative Civil Engineering Structures,* Winnipeg, Canada, in print 2002.

X. Zeng, X. Bao, Q. Yu, G. Ferrier, and G. Wu, "Structural health monitoring of a nuclear reactor wall with a distributed Brillouin sensor", in ***proceedings of the** 1st World Congress on Biomimetics and Artificial Muscles*, Albuquerque, USA, Dec. 9-11 2002.

X. Zeng, X. Bao, G. Ferrier, Q. Yu, R. E. Steffen, and M. Bowman, "Load Test of the Rollinsford Bridge Using the Distributed Brillouin Sensor", in ***proceedings of the** 1st World Congress on Biomimetics and Artificial Muscles*, Albuquerque, USA, Dec. 9-11 2002.

X. Bao, C. Huang, and **X. Zeng**, "Simultaneous strain and temperature monitoring of the composite cure with a Brillouin-scattering-based distributed sensor", ***Optical Engineering*, 41** (7), p. 1496 - 1501 2002.

Z. Liu, G. Ferrier, X. Bao, **X. Zeng**, Q. Yu, A. Kim, "Brillouin Scattering Based Distributed Fiber Optic Temperature Sensing for Fire Detection" presented at 7th International Symposium on Fire Safety Science, Worcester, Massachusetts, USA, June 2002.

Abstract

Brillouin scattering based distributed fiber optic sensing as a novel technique has attracted much attention in both research and application for the past ten years. The fiber optic group at the University of Ottawa has developed an advanced automatic Brillouin sensing system and improved it continuously. This thesis presents the characterization and optimization of this sensing system and a series of successful applications both in the laboratory and in the field.

Several parameters have been studied around the pulse generation subsystem: such as, bias, leakage, PW voltage, pulsewidth, and repetition frequency. Bias is found to be the most important parameter. We also discuss the relationships between the system repeatability and control parameters such as bias, polarization states, averages and frequency lock methods.

Four successful applications of the distributed Brillouin sensing system are reported in the thesis. They are strain measurement in a reinforced concrete beam, simultaneous strain and temperature monitoring of composite curing process, strain and temperature monitoring of a concrete structure, and temperature compensated strain measurement of the load test on the Rollinsford Bridge.

Acknowledgements

First of all, I would like to thank my supervisors, Dr. Xiaoyi Bao and Dr. Liang Chen, for introducing me to fiber optics. Their guidance, support and encouragement are indispensable with this project.

I would like to express my gratefulness to all the members composing the jury: Prof. John Armitage, Dr. Stephen Mihailov, and Prof. Thomas Brabec, for their evaluation of this work.

The contribution of my excellent partners, Mr. Qinrong Yu and Mr. Graham Ferrier is gratefully appreciated. Their participation is very important for this investigation in both reconstruction of the distributed Brillouin sensing system and the field applications.

I wish to thank ISIS Canada (Intelligent Sensing and Innovative Structures), NSERC (Natural Science and Engineering Research Council of Canada), CFI (Canada Foundation of Innovation) and University of Ottawa for their financial support of this work and Hydro Qu bec for their cooperation.

I want to thank all members in our fiber optic group at University of Ottawa. The help of Dr. Ping Lu, Mr. Guilin Wu, Dr. Dongfeng Liu, Dr. Lufan Zou, Mr. David Waddy, Dr. Chao Huang, Dr. Shahraam Afshaarvahid, and Mr. Khalid Al-qadi are appreciated.

The contribution of Ms. Chia Yee Chhoa, Dr. Anthony W. Brown, Dr. Michael D. DeMerchant in UNB are also acknowledged. I appreciate the support and cooperation of Dr. Robert E. Steffen, Ms. Martha Bowman, and Dr. Marc Demers in fiber installation of field tests.

Finally, I'd like to thank my wife, Huanmin and my son, Eric for their patience and understanding throughout the process in finishing this project.

Contents

List of Figures

List of Tables

List of Acronyms

AEEO	Lehrstuhl für Allgemeine Elektrotechnik und Elektrooptik (Ruhr-University)
APE™	Annealed Proton Exchange
AOM	Acousto-Optic Modulator
BOFDA	Brillouin Optical Frequency Domain Analysis
BOTDA	Brillouin Optical Time-Domain Analysis
BOTDR	Brillouin Optical Time-Domain Reflectometry
CTE	Coefficient of Thermal Expansion
CW	Continuous-Wave
DAC	Digital-to-Analogue Converter
DFB	Distributed feedback laser
DFB-LD	Distributed feedback laser diode
DBS	Distributed Brillouin Sensing
EDFA	Erbium-Doped Fiber Amplifier
EFPI	Extrinsic Fabry-Perot Interferometer
EM	Electro-Magnetic
EOM	Electro-Optic Modulator
EPFL	Swiss Federal Institute of Technology (Lausanne)
ERS	Electrical Resistance Strain (gauge)
FBG	Fiber Bragg Grating
FM	Frequency Modulation
FRP	Fiber-Reinforced Polymer
FWHM	Full Width at Half Maximum
FWM	Four-Wave Mixing
GPIB	General-purpose interface bus
GFRP	Glass Fiber Reinforced Polymer
HPC	High-Performance Concrete

IFFT	Inverse Fast Fourier Transform
$LiNbO_3$	Lithium Niobate
LPR	Landau Placzek ratio
LVDT	Linear Varying Displacement Transducer
MS	Mechanical Strain (gauge)
MZM	Mach-Zehnder (single output) Modulator
Nd: YAG	Neodymium-doped Yttrium-Aluminum Garnet
NEBT	New England Bulb Tee
NHDOT	New Hampshire Department of Transportation
NIBS	Noise Initiated Brillouin Scattering
NTT	Nippon Telegraph and Telephone
NWA	Network analyzer
OTDA	Optical Time Domain Analysis
OTDR	Optical Time-Domain Reflectometry
ORC	Optoelectronics Research Center (University of Southampton)
PM	Polarization-Maintaining
PMD	Polarization Mode Dispersion
PW	Pulse Width
SBS	Stimulated Brillouin Scattering
SNR	Signal-to-Noise Ratio
SOP	State of Polarization
SPM	Self-Phase Modulation
SRS	Stimulated Raman Scattering
TEC	Thermoelectric Cooler
UNB	University of New Brunswick
UO	University of Ottawa
XPM	Cross Phase Modulation
YBBM	Y-fed Balanced Bridge (dual output) Modulator

Chapter 1

Introduction

Fiber optic sensing, an emerging technology, has received a lot of attention in applied research in recent years. One of the important advantages of fiber optic sensors is their ability to provide passive sensing in a wide range of physical fields [Udd 1991]. This thesis will present the improvement and application of a Distributed Brillouin Sensing system developed in our group. This chapter provides a concise profile about fiber optic sensors and distributed fiber optic sensors.

1.1 Fiber optic sensors and applications

Fiber optic sensors have been developed for strain, temperature, vibration, displacement, rotation, pressure, sound, flow, viscosity, light intensity, as well as chemical, biomedical, and electrical variables [Udd, 1995; Kersey, 1996; Krohn, 2000]. Comparing to conventional sensors, such as electrical resistance strain (ERS) gauges and vibrating wire strain gauges, fiber optic sensors have many characteristic advantages. These include immunity to electromagnetic interference, low attenuation, lightweight and small size, multiplexing capability, remotable, and distributed measurement. These advantages give fiber optic sensors broad application areas compared with conventional sensors. No electromagnetic interference makes fiber optic sensors more stable; low attenuation makes long distance operation possible; small size and weight are suitable for non-destructive evaluation techniques; remote access allows access into normally inaccessible areas; multiplexing capability of some fiber optic sensors allows many sensors to be installed along a single optical fiber. Distributed sensing provides locations, temperature/strain over large structures, which is unavailable in any conventional sensors.

Fiber optic sensors can be normally divided into three basic categories, intensity-modulated, phase-modulated, and wavelength-modulated sensors [Krohn 2000]. Intensity-modulated sensors generally detect a change in received light intensity associated with physical perturbations of temperature, strain or displacement. The phase-modulated sensors are based on interferometers, which compare the phase of light in the sensing and reference fibers. A wavelength-modulated sensor measures wavelength change associated with strain, temperature or displacement. A typical application of wavelength modulation is accomplished with fiber Bragg gratings.

According to the style of operations, fiber optic sensors can be separated into localized sensors and distributed sensors. Most common localized (point) sensors are the sensor systems based on fiber Bragg grating (FBG) and extrinsic Fabry-Perot (or Michelson) interferometers (EFPIs of EMIs), similar to conventional electrical gauges.

Distributed fiber sensors normally indicate the sensor systems based on Rayleigh, Raman, and Brillouin reflectometry. Using multiplexing technologies, a network of point sensors also can be used to make quasi-distributed measurement.

1.2 Distributed fiber optic sensors

Most fiber optic sensor systems are localized, since the physical locations and the number of measuring points are fixed when the system is installed. However, distributed fiber optic sensors can measure a physical parameter at any arbitrary point along an optical sensing fiber. This is one important advantage of distributed fiber optic sensors.

Distributed fiber optic sensors can be simply divided into two different categories, fully distributed fiber optic sensors and quasi-distributed fiber optic sensors. Fully distributed optic sensors based on scattering phenomena in optical fibers such as Rayleigh, Raman or Brillouin scattering [Gysel 1990; Udd 1991; Agrawal 1995], allow measurements to be taken along the whole fiber length and uses the fiber itself as the sensing medium. Spatial information along the length of the optical fiber can be obtained through Optical Time Domain Analysis (OTDA) by measuring propagation times of optical pulses traveling in the fiber [Bao 2001].

Fully distributed fiber optic sensors can therefore monitor continuous rather than discrete points of the physical parameters. This type of sensor has tremendous potential for structural monitoring. A quasi-distributed fiber optic sensor can be made by multiplexing several point sensors on an optical fiber to form a sensing array or a network configuration. This kind of sensors measures a finite number of localized points rather than continuum distribution.

The advantages of monitoring continuum distributions have made distributed fiber optic sensors most attractive in many areas of application [Udd 1991]. Typical examples are health and structure monitoring for large structures, such as bridges, power stations, dams, ships, pipelines, oil or storage tanks, spacecrafts or airplanes. In addition embedded sensors in composite materials can evaluate stress, vibration, strain, and temperature in real time.

1.3 Fully distributed fiber optic sensors

Rayleigh scattering is an elastic scattering process engendered by structural fluctuations of medium density, which causes attenuation of the forward propagating signal in optical fibers. In the Rayleigh scattering process the scattered power is proportional to the incident power; no energy is transferred to the glass and no frequency change happens in the scattered light. Rayleigh scattering based on the Optical Time-Domain Reflectometry (OTDR) technique has been used for several distributed sensing applications, such as fiber loss. Because the dependance of the Rayleigh scattering intensity with temperature is too weak for normal optical fiber to result in an effective sensor, the practical application of the sensor is limited. A successful sample was proposed by Hartog [Hartog 1983] with special liquid core fibers.

Raman and Brillouin scattering are nonlinear (inelastic) processes that result in energy exchange between electromagnetic field and optical mediums. It was found that Raman scattering has a lower gain coefficient causing Raman scattered power about 30dB less than Rayleigh and 10 dB less than that of Brillouin scattering and so is generally observed with powerful optical pulses. Distributed temperature sensing using the temperature dependence of Raman scattering was first demonstrated in the mid-1980s and has been developed into a

commercial instrument [Udd 1991]. Kersey reported a distributed Raman sensor with 1°C temperature accuracy and 1m resolutions on a 10km sensing fiber [Kersey 1996].

Distributed Brillouin sensors are another fully distributed fiber optic sensors based on the nonlinear Brillouin Scattering process. Backward propagating scattered light will experience a frequency shift that is proportional to the speed of the acoustic phonons. Since the frequency shift depends linearly on the changing of outside physical conditions, such as strain and temperature, these parameters can be measured by analyzing the Brillouin loss spectrum of the fiber in the time domain [Bao et al 1995].

Followings are brief descriptions of the works presented in this thesis:

Stimulated Brillouin scattering and application of the Distributed Brillouin sensors are the main focus of this thesis.

Chapter 2 describes the theoretical background of the Brillouin scattering based distributed sensing and the configuration of UO's distributed Brillouin sensor system.

Chapter 3 reviews the research and applications of distributed Brillouin sensing.

Chapter 4 describes characterization and optimization of the distributed Brillouin sensor system, some experiments were done to find optimum parameters, such as the bias of Electro-Optic Modulator (EOM), PW (pulse width) voltage, amplitude of electrical pulse, repetition rate, polarization states, and laser frequency lock model, as well the repeatability of the system.

Chapter 5 describes the application of a distributed Brillouin sensing system in the lab with high spatial resolution and measurement accuracy. In this experiment the strain distribution of a concrete beam was measured for one-point and two-point loading patterns with single mode optical fiber embedded in pultruded* glass fiber reinforced polymer (GFRP) rod and bonded to steel reinforcing bars. Test results of the distributed Brillouin sensing (DBS) system are compared with that of conventional strain gauges and show good agreements.

Chapter 6 describes in-situ strain and temperature monitoring during the curing process of composite panels. We have presented test results on the Brillouin frequency shift measured by

an optical sensing fiber embedded within a 16-ply composite panel during the heat-up, isothermal hold and cool-down stages of the curing process. By deducting the temperature effects, the average strain profile along the mid-plane of the composite panel at various stages of the curing process can be obtained. The thermal response of the solidified composite during cooling is also profiled.

Chapter 7 presents two successful field applications of distributed Brillouin sensor. One is strain and temperature monitoring of a nuclear containment structure with distributed Brillouin sensing system. The other is the first temperature compensated strain measurement during the load testing of the Rollinsford Bridge with our DBS system. These two experiments provide useful experiences in fiber installation, temperature compensation, data analyzing, and test design for future applications.

Finally, **Chapter 8** summarizes the conclusion of the thesis and gives author's suggestions for future research.

Note*: the word "pultruded" means something produced by pulling it through machine and formed into long stretch, just like the rod, meanwhile pultrusion was the process of doing it.

Chapter 2

Brillouin Scattering Based Distributed Sensing

This chapter will present background on the Brillouin scattering phenomenon, the details of experimental system developed by our fiber optics group based on BOTDA technique and the operation of the system.

2.1 Optical nonlinear phenomena

In linear optics one assumes that an optical disturbance propagating through an optical medium could be described by a linear wave equation when light intensity is low. The response of any dielectric to light becomes nonlinear for intense electromagnetic fields [Agrawal 1995]. The origin of the nonlinear response is related to anharmonic motion of bound electrons under the influence of an applied field.

The total electric polarization P induced by electric dipoles in the medium is the key to study physics of nonlinear optics, and it can be expressed as a power series of applied electric field E

$$P_i = \varepsilon_0[\chi_{ij}^{(1)}E_j + \chi_{ijk}^{(2)}E_jE_k + \chi_{ijkl}^{(3)}E_jE_kE_l + ...]. \qquad (2.1)$$

where ε_0 is the vacuum permittivity and $\chi^{(j)}$ is jth order susceptibility and a tensor of rank j+1. The various-order of susceptibilities are the key parameters to describe the nonlinear coupling between incident waves and the generation of new frequency radiation through the induced nonlinear electric polarization of the medium. The linear susceptibility $\chi^{(1)}$ represents the dominant contribution to P (with the linear component $P^{(1)}(\omega) = \varepsilon_0\chi^{(1)}(\omega)E(\omega)$) and its effects are included through the refractive index n and the attenuation coefficient α. The second-order susceptibility $\chi^{(2)}$ is responsible sum-frequency generation and second-harmonic

generation. $\chi^{(3)}$ is responsible for phenomena such as four-wave mixing and nonlinear refraction, it is the third-order nonlinear polarization related to $\mathbf{P}^{(3)}(\omega = \omega_1 + \omega_2 + \omega_3) = \varepsilon_0\chi^{(3)}(\omega_1,\omega_2,\omega_3)\boldsymbol{E}(\omega_1)\boldsymbol{E}(\omega_2)\boldsymbol{E}(\omega_3)$. It is the cause of the intensity dependent refractive index in the fiber expressed with

$$\tilde{n}(\omega,|E|^2) = n(\omega) + n_2|E|^2, \tag{2.2}$$

where $n(\omega)$ is a linear part of refractive index, $|E|^2$ is the optical intensity inside the fiber, and n_2 is the nonlinear refractive index related to $\chi^{(3)}$.

The wave coupling phenomena in parametric effects are not restricted only to electromagnetic wave. If one of the participating electromagnetic waves can be replaced by material excitations (elastic vibrations in crystals or molecular vibrations). This is the case for Raman and Brillouin effects that are resulted form the interaction of the light waves with phonons in optical fibers and results in an energy exchange between the electromagnetic field and the optical medium. The nonlinear Brillouin scattering process (with the Stokes frequency shift about 13 GHz at 1319 nm) is the fundamental to the distributed Brillouin sensing technique. Raman scattering process (the Stokes shift of about 13 THz) can only be observed with powerful incident optical power (>1W). Because it has a two orders lower gain coefficient than that of the Brillouin scattering, one can ignore the impact of Raman scattering to the distributed Brillouin sensing technique.

The $\chi^{(3)}$ is also related to self-phase modulation (SPM), cross-phase modulation (XPM), and four-wave mixing (FWM). They arise from the nonlinear polarization and causes nonlinear refraction, where the refractive index is dependent on the optical power and becomes a function of the electric field [Agrawal 1995].

SPM refers to the self-induced phase shift experienced by an optical field during its propagation in fibers. Its magnitude can be obtained through the phase of optical field changes of $\varphi = (n + n_2|E|^2)k_0L$, where $k_0 = 2\pi/\lambda$ and L is the fiber length. The intensity-dependent nonlinear phase shift $\varphi_{NL} = n_2k_0L|E|^2$ is due to SPM. The main effect of SPM is to broaden the spectrum of optical pulses propagating through the optical fiber.

XPM effects occur when two optical fields co-propagate simultaneously and affect each other through the intensity dependence of the refractive index [Agrawal 1995]. It refers to the nonlinear phase shift of an optical field induced by a copropagating field at a different wavelength. XPM origin can be understood by noting the total electric field E in equation 2.1, $E = (1/2)\hat{x}[E_1 \exp(-i\omega_1 t) + E_2 \exp(-i\omega_2 t) + c.c.]$, when two optical fields at frequencies ω_1 and ω_2, polarized along the x axis, copropagate simultaneously inside the fiber. The nonlinear phase shift for the field at ω_1 is obtained by $\varphi_{NL} = n_2 k_0 L[|E_1|^2 + 2|E_2|^2]$, where all terms that generate polarization at frequencies other than ω_1 and ω_2 have been neglected because of their non-phase-matched character and the two terms are due to SPM and XPM respectively

When three light waves with frequencies ω_1, ω_2, and ω_3 propagate through an optical fiber simultaneously, a fourth wave with a frequency ω_4 may be generated under certain conditions that is known as four-wave mixing. In general, the frequency of a FWM product is given by $\omega_{ijk} = \omega_i + \omega_j - \omega_k$, where i, j, k = 1, 2 or 3 with $j \neq k$. The experiment shows that FWM can lead to spectral broadening whose magnitude increases with an increase in the incident power and can lead to crosstalk in multichannel communication systems [Agrawal 1995]. FWM arises due to the nonlinear response of bound electrons to applied optical fields. The induced polarization in the medium is not linear in the applied field. Its magnitude is governed by the nonlinear susceptibilities as shown in Eq. (2.1). FWM involves the third-order polarization

$$\mathbf{P}_{\mathrm{NL}} = \varepsilon_0 \chi^{(3)} \vdots \mathbf{EEE}, \tag{2.3}$$

The threshold power for FWM is expected to be lower than the Raman threshold if the phase matching is achieved. However, SRS dominates for long fibers practically. That is so because it is difficult to maintain phase matching in fiber over long lengths as a result of variations in the core diameter [Agrawal 1995].

SPM and XPM effects can be negligible in the Brillouin scattering process because of the relatively low peak powers associated with the Stokes and pump pulses and relative long pulse width (ns scale) [Agrawal 1995].

In stimulated Brillouin scattering (SBS) process, the forward and backward propagating components associated with the pump and Stokes waves present simultaneously. Higher-order

Stokes waves may be generated through cascade SBS, a process in which each successive Stokes component pumps the next-order Stokes component after its power becomes large enough to reach the Brillouin threshold. At the same time, anti-Stokes components are also generated through four-wave mixing between the copropagating pump and Stokes waves. The number of Stokes and the anti-Stokes components depends on the pump power. Enhanced Brillouin scattering can be observed if both of the pump and probe waves have strong powers running under CW operation, then both Stokes and anti-Stokes will get amplification. Such a case can happen if we enhance fiber endface reflection. However, here we used fiber index matching gel to eliminate such effects, because this is not useful for distributed sensor system.

2.2 Scattering phenomena in optical fibers

When the light travels in any media, transmission, reflection, absorption, and scattering may occur due to the interaction between light and media. In this study we focus on the scattering of light, which is a small fraction of the input light. Rayleigh, Raman, and Brillouin scattering are three main scattering phenomena. From scattering theory, Kaiser and Maier gave the number of photons per mode scattered per unit length

$$\frac{dN_S}{dz} = AN_I(N_S + 1) \tag{2.4}$$

where A is a constant determined the magnitude of the scattering process. N_S and N_I are scattered and incident photon numbers, respectively. If the incident light is strong, a large number of scattered photons are generated ($N_S >> 1$). The relationship between the numbers of incident and scattered photons can be expressed as

$$N_S = N_S(0)\exp(AN_I L) \tag{2.5}$$

where L is the length over which scattering occurs. This is known as the stimulated scattering regime because the presence of a significant amount of scattered light stimulates the production of more. The scattered intensity will exponentially increase with the increasing of the incident intensity. As the intensity of the incident light decreases and $N_S << 1$, the equation 2.4 is simplified to

$$N_S = AN_I L. \tag{2.6}$$

One can find that the scattering is proportional to the incident intensity and the interaction length. The scattering is known as spontaneous scattering.

Rayleigh scattering, the strongest scattering phenomenon in optical fibers, is a linear (elastic) scattering process in which the scattered power is proportional to the incident power, no energy is transferred to the glass, and no frequency change happens in the scattered light. Normally, the inhomogeneities of the refractive index of the optical media (due to the manufacture process) or structural fluctuation of the medium density are responsible to these scattering phenomena.

The refractive index variations caused by the density differences of an acoustic wave traveling through a transparent material can also scatter light. Since the density variations of an acoustic wave are periodic and travel in the media, the scattering takes place for a given direction and induces a frequency shift of the scattered light. Therefore Raman and Brillouin scattering are inelastic processes that result in energy exchange between electromagnetic field and optical mediums. Brillouin scattering arises from density fluctuation related to pressure variations in the medium in which traveling of acoustic waves is caused by molecular thermal agitation [Agrawal1995]. The inelastic interaction between optical photons and acoustic phonons leads to a frequency shift of the scattered phonons directly dependent on the characteristic of the sound velocity of the medium. Raman scattering comes from the inelastic interaction between light wave and the vibration states of molecules. Optical phonons generated by thermal agitation involve in the Raman scattering process.

Using the quantum-mechanical theory, both Raman and Brillouin scattering processes involve the same process in which a photon of the incident field is annihilated to create a photon at a lower frequency (belonging to the Stokes wave) and a phonon with the right energy and momentum to conserve the energy and the momentum. Of course, a higher-energy photon at the so-called anti-Stokes frequency can also be created if a phonon of right energy and momentum is available [Agrawal1995]. Both scattering processes result in a loss of power at the incident frequency and constitute a loss mechanism for optical fibers. One of major differences between them is that optical phonons participate in Raman scattering, whereas acoustic phonons participate in Brillouin scattering.

2.2.1 Spontaneous and stimulated Brillouin scattering

The spontaneous Brillouin scattering is a linear process ($N_S << 1$). It occurs when a weak, but high-coherence incident light interacts with an acoustic wave generated by the incident light in an optical fiber. The fluctuations of refractive index are due to the presence of the acoustic phonons within the optical fiber core [Tang, 1966]. The speed of sound V_A with which an acoustic wave travels in the optical media causes moving periodic variations in the material density that results in periodic variations in the refractive index. The pump light grating scatters through Bragg diffraction and experiences a frequency downshifted due to the Doppler effect. The scattering process can be thought of as the annihilation of a pump photon that creates an anti-Stokes photon, while the creation of an acoustic phonon creates a Stokes photon according to the quantum mechanism. Since either energy or momentum should be conserved in each scattering event, the frequencies and wave vectors of the incident light, the acoustic wave and the scattered wave must satisfy the relations [Agrawal, 1995] as shown in equation 2.7.

For Stokes wave:

$$\begin{aligned} \omega_S &= \omega_P - \omega_A \\ \vec{k}_S &= \vec{k}_P - \vec{k}_A \end{aligned} \tag{2.7}$$

For Anti-Stokes wave:

$$\begin{aligned} \omega_{AS} &= \omega_P + \omega_A \\ \vec{k}_{AS} &= \vec{k}_P + \vec{k}_A \end{aligned}$$

where ω is the angular frequency, $\vec{k}$ is the wave vector, the subscripts *A, P, S, AS* represent the acoustic, pump, Stokes, and anti-Stokes wave, respectively. If θ represents the angle between the pump and Stokes waves and V_A is the acoustic velocity, a dispersion relation between the frequency and wave vector of the acoustic wave can be expressed as [Smith 1999]

$$\omega_A = \left|\vec{k}_A\right| V_A = 2V_A \left|\vec{k}_P\right| \sin(\theta/2) \tag{2.8}$$

Equation 2.8 indicates the dependence of the frequency shift for Stokes wave on the scattering angle. In a single mode optical fiber, scattering is in the forward ($\theta=0$) and the backward direction ($\theta = \pi$). In the forward direction the frequency shift vanishes and in the backward

direction it is a maximum that predict both spontaneous Brillouin scattering and SBS can only occur in the backward direction. Parker et al. give the frequency shift ν_B in the backward direction

$$\nu_B = \frac{\omega_A}{2\pi} = \frac{2nV_A}{\lambda} \tag{2.9}$$

where λ is the pump wavelength and n is the refractive index [Parker et al. 1997]. As the acoustic velocity is about 6000m/s and $n \approx 1.46$ for optical fibers, Brillouin shift will be about 11GHz at 1550nm and 12.8GHz at 1320nm, respectively. We can find Brillouin shift is a function of both the acoustic velocity of the optical media and the refractive index. Since these two parameters are strain and temperature dependent, it predicts that distributed sensing based on Brillouin scattering is available [Smith et al. 1999b]. The Brillouin gain coefficient $g_B(\nu)$ characterizes the growth of the Stokes wave and the peak gain value at the frequency $\nu = \nu_B$. The spectral width $\Delta\nu_B$ of the Brillouin scattering light is related to the damping time of acoustic waves that are assumed to decay exponentially or the acoustic phonon lifetime τ_A.

$$\Delta\nu_B = \frac{1}{\pi\tau_A} \tag{2.10}$$

The Brillouin gain coefficient has a Lorentzian spectral profile given by

$$g_B(\nu) = \frac{g_B(\nu_B)}{1+\left[\frac{2(\nu-\nu_B)}{\Delta\nu_B}\right]^2} \tag{2.11}$$

where $g_B(\nu_B)$ is the peak value of the gain coefficient at $\nu = \nu_B$. It can be expressed as

$$g_B(\nu_B) = \frac{2\pi n^7 p_{12}^2}{c\lambda^2 \rho V_A \Delta\nu_B} \tag{2.12}$$

where p_{12}, ρ, and λ are the longitudinal photoelastic coefficient, the material density, and the pump wavelength, respectively [Agrawal 1995]. For most optical fibers, the peak value of the Brillouin gain is on the order of $(1\sim 5)\times 10^{-11}$ m/W [Smith 1999]. Since it is about two orders

greater than that of the Raman scattering, Brillouin scattering is thought of the dominant nonlinear scattering process in optical fibers.

Once the Brillouin threshold power is reached, stimulated Brillouin scattering (SBS) is generated which is related to electrostriction through $\chi^{(3)}$.

When a dielectric is governed by an applied electric field, it will feel an internal stress that is proportional to the square of the electric field [Vanderlinde 1993]. That phenomenon is known as electrostriction. The electrostrictive pressure p_{el} can be expressed as a function of the electric field intensity

$$p_{el} = -\frac{1}{2}\gamma |E|^2 \tag{2.13}$$

where $\gamma = \rho_0 \partial\varepsilon / \partial\rho = n^4 \varepsilon_0 p_{12}$ is the electrostrictive coefficient, ρ_0 is average value of the medium density, and ε is the dielectric constant. The longitudinal photoelastic coefficient p_{12} is important for Brillouin scattering as it relates the mechanical strain in the axial direction to the radial electric field [Brown 2000]. The stress (pressure) within a dielectric medium generated by an inhomogeneous electric field will result in the local variations of the material density and consequently to an increase of the refractive index in the medium. The density variation of the dielectric resulting from an acoustic wave implies a pressure variation $\Delta p = K\Delta\rho / \rho$ and a variation of the dielectric susceptibility

$$\Delta\chi = \frac{\gamma}{\varepsilon_0}\frac{\Delta\rho}{\rho} \tag{2.14}$$

Because of the periodic nature of the acoustic wave, the refractive index of the dielectric will undergo a periodic variation.

SBS can be presented as a three-wave interaction process between an incident light, optically induced acoustic phonons and the scattered light (Stokes) wave. The incident light wave is scattered by sound wave (acoustic phonons) via Bragg diffraction. The scattered light wave then interacts with incident light to produce a moving interference pattern that creates more phonons by electrostriction resulting in a continuous scattering process.

When the incident light intensity is greater than a threshold power, a large number of scattered phonons will be generated. The scattered light intensity will rise exponentially with the increasing of the intensity of the incident light with the highest gain around the Brillouin frequency, while the spectral shape will narrow and Gaussian profile will replace Lorentzian profile [Gaeta and Boyd 1991].

2.2.2 Effect of Brillouin amplification

As described above, when incident light travels within an optical fiber, electrostrictive effect will create a large amount of acoustic phonons acting as a phonon generator for SBS. Whenever the beat frequency between the incident and Stokes wave couples to the acoustic wave, the Stokes wave gets amplified, while the anti-Stokes wave suffers depletion. Actually, Brillouin amplification can be obtained by an external signal with an optical frequency near the frequency of the Stokes wave naturally scattered by the fiber. If we named the incident light as pump signal, this external signal can usually be called probe signal. A probe-pump technique using two counter-propagating lasers at two ends of an optical fiber in an experimental setup can greatly increase the coupling between pump and Stokes wave that is the Brillouin optical time-domain analysis (BOTDA) sensing system first introduced in NTT [Horiguchi and Tateda 1989]. When the Brillouin frequency is matched by the frequency difference between probe and pump, the intensity of the Stokes wave will be greatly amplified.

The physical process of Brillouin amplification can be thought of as a nonlinear interaction between the probe and pump waves through an acoustic wave. The beat field resulting from the interference of the pump and Stokes waves generates an acoustic wave through the process of electrostriction. The acoustic wave will result in a periodic modulation of the refractive index of the fiber, which grating scatters the pump through Bragg diffraction. Scattered light suffers a frequency downshift due to the Doppler effect induced by the index grating traveling with the acoustic velocity.

The nonlinear interaction between the pump, probe, and acoustic waves introduces Brillouin gain over an optical fiber. From Maxwell's equations and Navier-Stokes equation

for the acoustic field in the optical media we can derive three equations to describe SBS process with the slowly varying envelope approximation [Kaiser and Maier 1972; Horiguchi et al. 1989; Afshaarvahid and Munch 2001]

$$\begin{aligned}
&\left(\frac{\partial}{\partial t}+\Omega\right)Q=-ig_1E_pE_s^*,\\
&\left(\frac{\partial}{\partial z}+\frac{n}{c}\cdot\frac{\partial}{\partial t}\right)E_s=-ig_2Q^*E_p+\frac{1}{2}\alpha E_s,\\
&\left(\frac{\partial}{\partial z}-\frac{n}{c}\cdot\frac{\partial}{\partial t}\right)E_p=ig_2QE_s-\frac{1}{2}\alpha E_p.
\end{aligned} \tag{2.15}$$

where E_p, E_s, and Q are pump, Stokes, and acoustic fields, respectively. The g_1 and g_2 are coupling constants. $\Omega=1/2\tau+i\Delta\omega$. Here $1/2\tau$ is the damping rate, $\Delta\omega$ is the detuning frequency, and α is the linear fiber attenuation coefficient. Ignoring $\partial/\partial t$ for the steady state regime, the equation 2.21 can be written to

$$\begin{aligned}
\frac{\partial}{\partial z}E_p&=\left(\frac{g_1g_2}{\Omega}\right)|E_s|^2E_p-\frac{1}{2}\alpha E_p\\
\frac{\partial}{\partial z}E_s&=\left(\frac{g_1g_2}{\Omega^*}\right)|E_p|^2E_s+\frac{1}{2}\alpha E_s
\end{aligned} \tag{2.16}$$

On the other hand, assuming zero feedback in the system and taking the limit of the instantaneous phonon response, the SBS dynamics in a single mode fiber can be described by the following two equations between the pump and the Stokes intensities [Chen and Bao 1998]

$$\begin{aligned}
\left[\frac{n}{c}\left(\frac{\partial}{\partial t}\right)+\frac{\partial}{\partial z}\right]I_p&=(-\alpha-g_BI_s)I_p\\
\left[\frac{n}{c}\left(\frac{\partial}{\partial t}\right)-\frac{\partial}{\partial z}\right]I_s&=(-\alpha+g_BI_p)I_s
\end{aligned} \tag{2.17}$$

where I_p and I_s are the intensities of the pump and the Stokes waves in the fiber, g_B is the Brillouin gain coefficient, c is the speed of light in vacuum, and n is the refractive index of the fiber. Neglecting the time dependence of the system and the dynamic response of the acoustic waves we can easily derive the steady state coupling equation [Pannell et al.1993].

$$\frac{dI_p}{dz} = -\alpha I_p \pm g_B I_s I_p$$
$$\frac{dI_s}{dz} = \alpha I_s \pm g_B I_s I_p \tag{2.18}$$

where the symbol "$\pm$" represents the case of Brillouin loss or gain, respectively. If a pulse beam at frequency $\nu_0 + \nu_B$ is used for the pump wave and a cw laser beam with frequency ν_0 for the probe that is about ν_B less than the pump, it is the Brillouin gain case with a power transfer from the pulsed wave to the cw wave. Reversing the two laser frequencies for Brillouin loss case, an increase in the Brillouin scattered light can be obtained by a transfer of power from the cw probe to the pump pulse.

Agrawal summarized most of the works about SBS in his *Nonlinear Fiber Optics* [Agrawal 1995]. Unfortunately, an incorrect analytical solution listed in his book. Chen and Bao provided correct solutions for the steady state SBS both analytically and numerically, as well the threshold condition in single mode fiber [Chen and Bao 1998]. The exact solution is left in integral form, because no closed form solution for the integral was found

$$\Sigma(z) = \sqrt{\left(\Sigma_0^2 - \Delta_0^2\right) \cdot \exp\left\{\left(g_B/\alpha\right)\left[\Delta(z) - \Delta_0\right]\right\} + \Delta^2(z)} \tag{2.19}$$

$$\int_{\Delta_0}^{\Delta(z)} \frac{dx}{\sqrt{\left(\Sigma_0^2 - \Delta_0^2\right) \cdot \exp\left[\left(g_B/\alpha\right)\left(x - \Delta_0\right) + x^2\right]}} = -\alpha z \tag{2.20}$$

where $\Delta = I_p - I_s$ and $\Sigma = I_p + I_s$ are introduced, Δ_0 and Σ_0 are the corresponding values at the origin $(z = 0)$.

Smith analytically solved the Brillouin loss steady-state coupled wave equations by neglecting any increases in the pump power [Smith 1999]. Brillouin power as a function of the frequency difference between the pump and probe lasers is given by

$$P(\nu) = P_{CW} e^{-\alpha L}[1 - \exp(-g_B(\nu) P_P \frac{L_{eff}}{A_{eff}})] \tag{2.21}$$

where P_{cw} and P_p are the input probe and pump laser powers, respectively; A_{eff} is the effective area of the fiber core and L_{eff} is the effective length of the fiber expressed as

$$L_{eff} = \frac{1}{\alpha}(1 - e^{-\alpha L}). \quad (2.22)$$

In this case, the signal power is defined as the power difference between the measured power and the power when the gain is equal to zero ($\nu >> \nu_B$ or $\nu << \nu_B$) and is measured where the pump was launched into the sensing fiber.

2.3 Principles of Brillouin loss based distributed sensing

Brillouin spectrum measurement of an optical fiber is the foundation of distributed sensing. It can be fulfilled with many different system configurations that will be presented in chapter 3. The fundamental structure of a Brillouin loss based distributed sensor include two lasers for counter-propagation, a pulse generation subsystem, an optical fiber as the sensing medium, and a detecting subsystem to receive backscattered optical signal.

2.3.1 System configuration

A Brillouin loss based distributed fiber optic sensing system has been developed in our fiber optics group. It's a BOTDA system and the configuration is shown in Figure 2.1. The system is based on the interaction of a pulsed laser beam and a counter-propagating continuous wave laser beam. The signal detection occurs at the pump end of the system for both Brillouin gain or loss operation. The difference between the two operations is shown in Figure2.2 and Figure 2.3. Due to low depletion of the pump power with Brillouin loss, the system performance of Brillouin loss based distributed sensing was improved to the total sensing length of 51km [Bao et al. 1995].

The light sources of the Brillouin loss system (Figure 2.1) are two tunable CW Nd: YAG laser operating at 1319 to provide two count-propagating light waves for the probe-pump approach: one laser is CW operation; the other one operates in the pulse mode by optical modulator.

The optical pulse works as a probe to locate the sensing position along the fiber and provides the spatial resolution of the system with the pulse duration. The Brillouin signal

measured by the system is a CW signal measured as a function of the time to indicate the interaction between the CW and pulse signal and the pulse arrival time. An optical circulator is used for 1) to take the Brillouin interaction signal from the sensing fiber, 2) to send the pulsed beam to the sensing fiber. AC coupled detector is used to strip the DC signal component resulted from the CW background.

Spatial polarization noise is an important error source of the distributed Brillouin sensing system (detailed discussion in Chapter 4). There are two orthogonal polarization modes supported by a single mode fiber. The polarized output light of two lasers can be transferred from one mode to the other through mode coupling by small perturbations to the fiber. Since traveling through a sensing fiber, the states of polarization (SOP) from two lasers can be matched in some regions, but perpendicular in other regions. When both pump and Stokes light have same polarization states, the highest scattered signal can be detected. To minimize the errors coming from different polarization states, we use the polarization scrambler to average out the polarization dependence in the Brillouin signal.

A variable attenuator was added to deal with the power dependence of the Brillouin spectrum in the test. The most important function of this component is to limit the CW probe power under the SBS threshold that prevents the feedback enhanced Brillouin effect to deplete the Brillouin amplification of the system.

An optical isolator is used between the CW laser arm and the sensing fiber to avoid the feedback of the Stokes from the laser-cavity mirror back into the fiber.

Beat frequency is measured by a frequency counter with a phase locked loop to lock the beat frequency at the Brillouin frequency within 10 Hz between two lasers. A data acquisition system is used to record the electrical signal over time. The sequence mode, a most important feature of the digitizer, allows up to 2000 waveforms to be averaged with 25 μs dead time between "segments" [Brown 2000]. The built in waveform processing calculates the average of all segments rapidly. The overall acquisition time for each measured point along the fiber is shorter than setting the beat frequency of the lasers on the frequency counter.

A computer is used to control the DBS system operation and data acquisition automatically via 100 Mb/s Ethernet card, IEEE 488.2 general-purpose interface bus (GPIB) card, digital to analog converters (DACs), and single bit digital outputs, to connect the various devices and

data acquisition. The Ethernet interface with the data acquisition unit in a digitizer provides high-speed connection. The frequency counter, power meter, and polarization controller were connected to the computer with the GPIB card. A multifunction I/O board is used to provide the DACs and digital outputs for controlling the simple devices.

2.3.2 System operation

The Brillouin gain or loss process is a typical Brillouin amplification process that requires interference between two counter-propagating optical waves. Brillouin amplification is not observable when two optical waves have orthogonal polarization states.

For the Brillouin loss process within a single mode optical fiber, a pulsed light wave from the pump laser at frequency ν_1 interacts with the counter-propagating CW light wave from the probe laser with frequency ν_2 and a copropagating acoustic wave of frequency ν_2 - ν_1. The power is transferred from the CW light wave to the pulsed light wave and the acoustic wave in this three wave mixing process. The coupling between the two optical waves occurs due to diffraction from the refractive index perturbation produced by the acoustic field, while energy is supplied to the acoustic wave as a result of the interference pattern between the two light waves through the process of electrostriction.

This probe-pump approach of Brillouin amplification should work under SBS threshold to prevent the counter-propagating Stokes wave generated by the CW light wave to disturb the desired CW depletion signal. That is why a tunable attenuator is placed in the CW laser side to control the probe power.

When pulse stream propagates through an optical fiber, the CW power is transferred to the pulsed wave whenever the frequency difference between two lasers is matched the Brillouin frequency ν_B of the fiber ($\nu_B = \nu_2 - \nu_1$ and $\nu_2 > \nu_1$). At the Brillouin frequency, the acoustic wavelength is half of the mean optical wavelength that is simply the condition for Bragg diffraction of the light from the acoustic wave. The acoustic velocity (and hence the Brillouin frequency) is dependent on the temperature/strain of the fiber, so by measuring the frequency

difference between two lasers at which maximum Brillouin loss occurs, that temperature/strain can be detected [Bao et al. 1995].

The spatial information can be obtained using optical time domain analysis (OTDA) of the probe signal [DeMerchant et al. 1998]. For any given instant, the moving optical pulse can only be in one location. Any point along the fiber is possible to generate a signal only at the instant that the pulse passes through it. By recording the pump beam power level over time and matching each instant in time to a unique location in the fiber, the Brillouin loss at each location can be obtained. The equation 2.23 shows the relation of the pulse round-trip propagating time t, a given distance d from the pulse injection point, and the refractive index n of the fiber.

$$t = \frac{2nd}{c} \tag{2.23}$$

The Brillouin shift measured at any particular point is not an exact value at that point, but rather it represents the composition of all frequency shifts covered by the pulse width (gauge length). The strain or temperature at one spatial position along the optical sensing fiber is determined by finding an average value within a chosen spatial resolution.

2.3.3 Time domain waveform

For any location along the fiber, the Brillouin frequency can be determined uniquely, while for any beat frequency, there is a time domain waveform trace along the entire fiber. Whenever the beat frequency between two lasers is changed, the control software of the system will acquire a set of time domain data, which represents the variation of cw power level as the optical pulse travels through the sensing fiber.

2.3.4 Frequency spectrum

Determining the Brillouin shift ν_B along the entire sensing fiber is a key step to produce the strain and temperature that can be obtained by the frequency domain analysis [DeMerchant et al. 1998]. Since the total scattered power is actually spread over a frequency shifts range

centered about ν_B rather than a single frequency, the frequency domain analysis is performed by fitting the test points to a profile to the signal spectrum [Bao et al 1993a; Horiguchi et al 1995]. Once the Brillouin frequency ν_B is obtained, we can easily convert to a temperature or strain measurement using the calibration constants of the fiber. Normally we assume the spectrum have a Lorentzian shape and fit the profiles to the signal spectrum

$$g(\nu) = \frac{g_B}{1+4\left[\frac{\nu-\nu_B}{\Delta\nu_B}\right]^2} \tag{2.24}$$

where g_B, ν_B, and $\Delta\nu_B$ are the peak gain, the central frequency shift, and the linewidth, respectively as shown in Figure 2.4. From Figure 2.4, the central frequency ν_B is the Brillouin shift of the fiber, the peak gain g_B is the maximum gain value at central frequency ν_B, and the linewidth $\Delta\nu_B$ is the full width at half maximum (FWHM) of the spectral peak. Bao et al. found that by using extremely short optical pulsewidth or high incident laser powers, the shapes of the Brillouin gain spectrum deviate from Lorentzian [Bao et al 1999]. Additional parameters are defined to characterize the resulting spectral shape in these cases [DeMerchant 2000].

2.4 Application of Brillouin loss based distributed sensing

Distributed sensing can be applied to measure parameters of strain, temperature, vibration, displacement, rotation, pressure, sound, flow, viscosity, light intensity, as well chemical, biomedical, and electrical variables [Udd, 1995; Kersey, 1996; Krohn, 2000]. However, the most important applications are strain and temperature measurement that have been employed in civil engineering and aerospace area. In this section we focus on strain and temperature measurement.

Brillouin shift is related to the refractive index n and acoustic velocity V_A, both of them are strain and temperature dependent on the sensing fiber $\nu_B = 2nV_A/\lambda \propto T \,\&\, \varepsilon$ [Smith 1999]. The thermal effect induced density changes. A slight temperature dependence of the refractive index of silica fiber also contributes to Brillouin shift on temperature [DeMerchant 2000]. The

refractive index is strain dependant due to the elasto-optic effect and acoustic velocity is affected by strain induced density changes and the strain dependent nature of the modulus of elasticity of silica material.

Smith presented the Brillouin shift as a higher order function of strain theoretically [Smith 1999].

$$\nu_B(\varepsilon) = \frac{2n_0\left(1-\frac{n_0^2}{2}p\varepsilon\right)}{\lambda}\sqrt{\frac{E_{C0}(1-p_r)(1+\alpha_C\varepsilon)(1+\varepsilon)(1-p_r\varepsilon)^2}{\rho_0(1+p_r)(1-2p_r)}} \tag{2.25}$$

where n_0 is the zero strain value of the refractive index. $p_r = \varepsilon_{rad}/\varepsilon = (\delta r/r_0)/(\delta L/L_0)$ is Poisson ratio, p = 0.21 is the photoelastic coefficient, ε_{rad} is the radial strain, r_0 and L_0 are unstrained fiber core radius and unstrained fiber length, respectively. $E_{C0} = 67.5GPa$ is the zero strain value of the core's modulus, and α_C has a value of 8.6. The unstrained density of the core/cladding ρ_0 is assumed to be 2200 kg/m^3 [Shand 1958].

However, Brillouin shift can be approximated by simple linear relationships to both strain and temperature over the range of practically achievable conditions as shown in equation 2.26 and 2.27.

$$\nu_B(\varepsilon) = \nu_B(\varepsilon_0) + \frac{d\nu_B(\varepsilon)}{d\varepsilon}\cdot(\varepsilon-\varepsilon_0) \tag{2.26}$$

$$\nu_B(T) = \nu_B(T_0) + \frac{d\nu_B(T)}{dT}\cdot(T-T_0) \tag{2.27}$$

where ε is strain and T (°C) is temperature, ε_0 and T_0 are values at an arbitrary reference fiber state, for example, zero strain and room temperature states. The slopes $d\nu_B(\varepsilon)/d\varepsilon = 0.056MHz/\mu\varepsilon$ ($\mu\varepsilon$ is the strain unit, i.e. μm/m) and $d\nu_B(T)/dT = 1.2MHz/°C$ are Brillouin shift/strain coefficient and Brillouin shift/temperature coefficient, respectively. Actually, both of them should be determined experimentally through the system calibrations in the lab for different optical fibers. From above equations, it is easy to derive

$$T = C_T[\nu_B(T) - \nu_B(T_0)] + T_0$$
$$\varepsilon = C_\varepsilon[\nu_B(\varepsilon) - \nu_B(\varepsilon_0)] + \varepsilon_0 \quad (2.28)$$

where C_T is temperature/Brillouin shift coefficient and C_ε is strain/Brillouin shift coefficient. We obtained the value of 0.819°C/MHz for C_T and the value of 17.09 με/MHz for C_ε at 1319 nm light source with the conventional SMF-28 fibers from the fiber calibration in the lab.

Since Brillouin shift ν_B is dependent on both strain and temperature as shown in equation 2.29, it is very difficult from unique measured parameter ν_B to determine whether observed changes are due to strain or temperature effects. Therefore, a normal sensing system is limited to measure either strain or temperature but not both at the same time, although in most case the impact of strain and temperature are present simultaneously.

$$\nu_B = \nu_{B0} + \frac{\partial \nu}{\partial T} T + \frac{\partial \nu}{\partial \varepsilon} \varepsilon \quad (2.29)$$

where ν_{B0} is the Brillouin frequency at a temperature of 0°C and a strain of 0 με. One can easily de-couple temperature and strain measurements by simply using a loose fiber (strain free) for temperature sensing, maintaining same environment temperature in a strain measurement or introducing a piece of reference fiber for temperature compensation.

Once the Brillouin shift is obtained from the measurement, one can easily calculate strain or temperature using equation 2.28. Figure 2.5 and Figure 2.6 illustrate a load test that can show the relation between strain and Brillouin shift. A four-meter long section of PVC buffered single mode fiber was loaded with a weight of 500g that caused the variation of Brillouin frequency in Figure 2.5. This frequency change is corresponded to a uniform strain of 2600 με generated over the 4m sensing fiber from Z_1 to Z_2 in Figure 2.6. The positions along a fiber are obtained from

$$Z = \frac{C\Delta t}{2n} \quad (2.30)$$

where Δt is the time interval from launching the pulsed light to receiving the scattered light at the end of the optical fiber. Z is the distance from the position (Z_1) where pulsed light is launched to the position (Z_2) where the scattered light is generated. C is the speed of light in a vacuum and n is the refractive index of the optical fiber.

2.5 Fitting of the experimental data

The software "sensortool" developed by our group can provide a number of ways to get Brillouin spectrum. Using this software, one can choose the most suitable profile to fit the experimental data depending on the spectrum characteristics. The Marquardt-Levenburg algorithm [Press et al. 1996] for curve fitting is used to perform non-linear least squares fitting Brillouin spectrum.

A Lorentzian profile was initially used to fit all of the simple Brillouin gain spectrum data with good results [DeMerchant 2000]. The form of the function was

$$g(\nu) = \frac{g_B}{1 + 4\left[\frac{\nu - \nu_B}{\Delta\nu_B}\right]^2} + g_0 \tag{2.31}$$

where g_0 used to provide an offset to the entire gain spectrum. However, due to the increasingly shorter duration probe pulses being used to improve spatial resolution, the evolution of the sensing system design over the lifetime of the project ultimately required a new spectral shape to be adopted. It was found the spectral width grows larger with the duration of the probe pulses growing shorter and the Brillouin spectrum becomes broader near Gaussian shape [Smith 1999]. Smith suggested accommodating the potential variation of the spectral shape with Pseudo-Voigt profile

$$g(\nu) = g_B\left[\frac{\beta}{1 + \left[\frac{2(\nu - \nu_B)}{\Delta\nu_B}\right]^2} + (1-\beta)\exp\left[-In(2)\left[\frac{2(\nu - \nu_B)}{\Delta\nu_B}\right]^2\right]\right] + g_0 \tag{2.32}$$

This profile is formed from a combination of a Lorentzian and a Gaussian. Where the shape factor β determines the relative contributions of the Lorentzian and Gaussian portions of the profile. When β has a value of zero, the spectrum is a pure Gaussian shape. One can find the Pseudo-Voight profile provides a quantitative description of the single peak Brillouin loss spectrum and is easy for analysis.

For a complex spectrum, a number of curve fitting methods can be used depending on different experimental conditions, such as localized peak fitting, multiple peak fitting, and spectrum centroid analysis. Our group devised the spectrum centroid method of analysis that seeks to determine a Brillouin shift represented the average strain of a fiber section subjected to a continuous strain distribution [DeMerchant 2000]. The method involves finding the centroid of the area under the gain spectrum along the pump-probe frequency difference axis. It becomes the standard method of complex spectra analysis for many applications. The centroid of the entire spectrum can be expressed as

$$\bar{\nu} = \lim_{N\to\infty} \frac{\sum_{i=0}^{N} A_i \nu_{B_i}}{\sum_{i=0}^{N} A_i}, \tag{2.33}$$

where A_i is the area under each peak. This method has been used to get the average strain reading in the later part of the strain/temperature measurement.

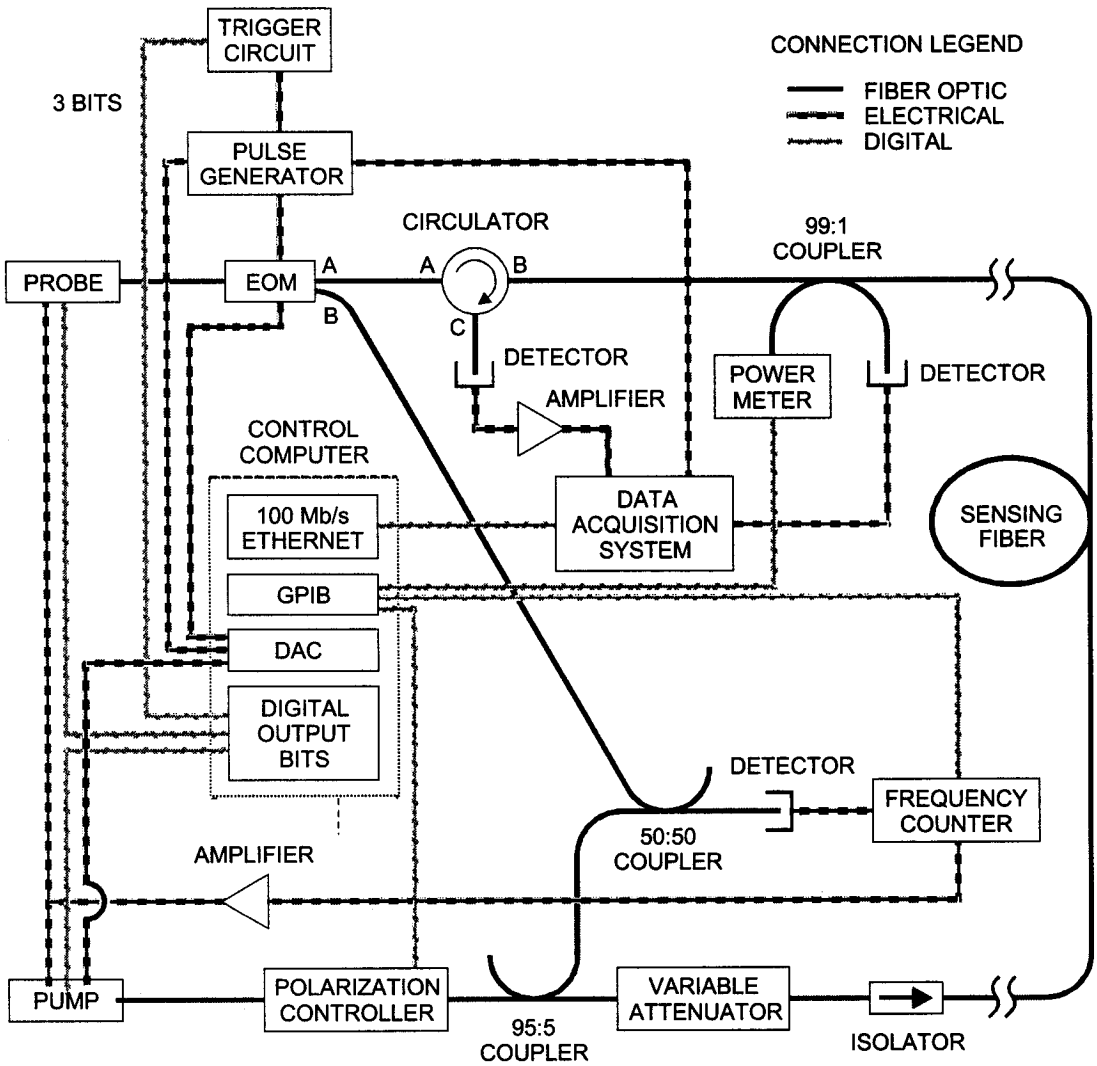

Figure 2.1 Configuration of the Brillouin scattering based distributed sensing system.

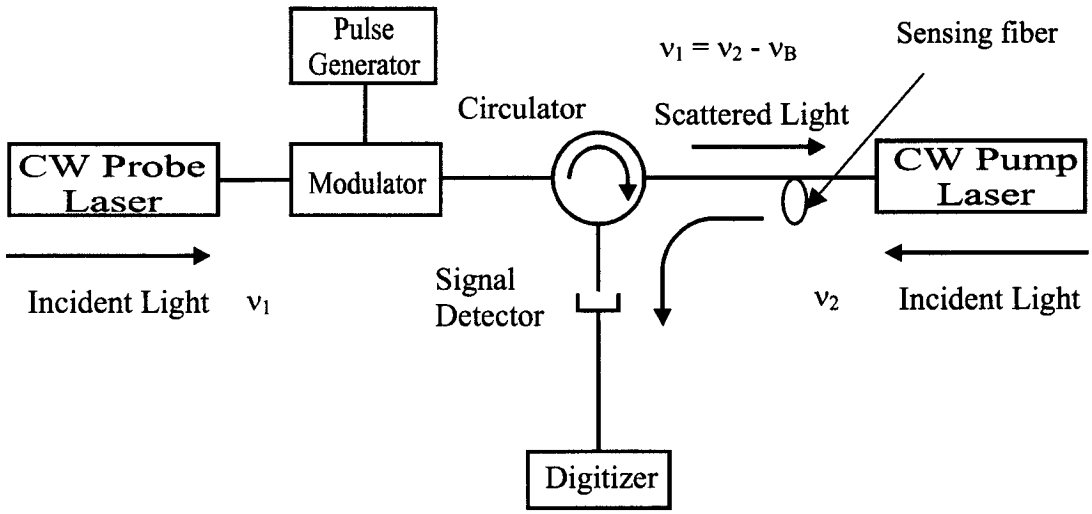

Figure 2.2 Brillouin loss based distributed sensing system used two lasers to generate Brillouin amplification. When the frequency difference between two lasers matches $\nu_1 = \nu_2 - \nu_B$ the probe pulse is amplified by depletion of the pump power.

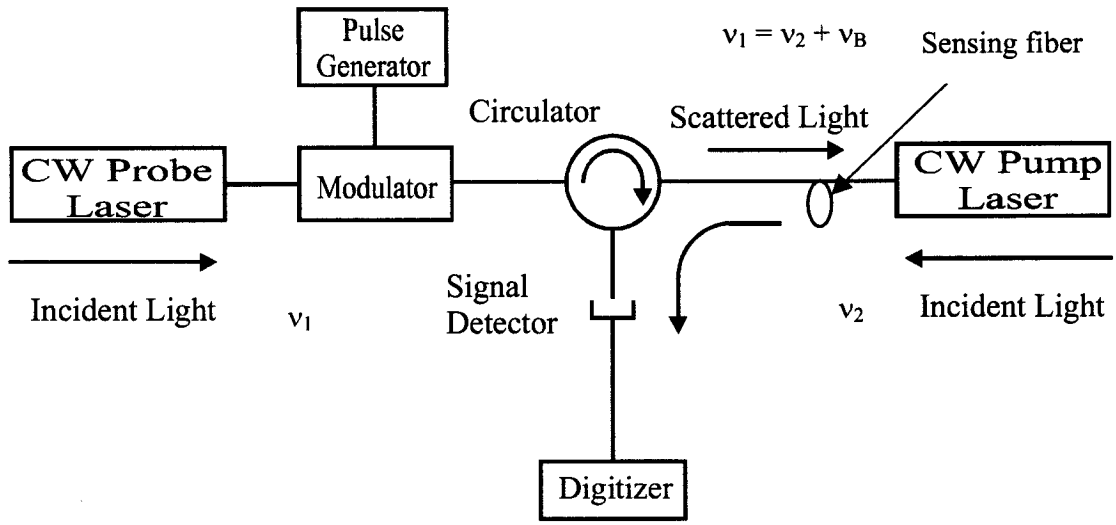

Figure 2.3 Brillouin gain based distributed sensing system also used two lasers to generate Brillouin amplification. When $\nu_1 = \nu_2 + \nu_B$ the Brillouin signal is amplified by depletion of the pump pulse.

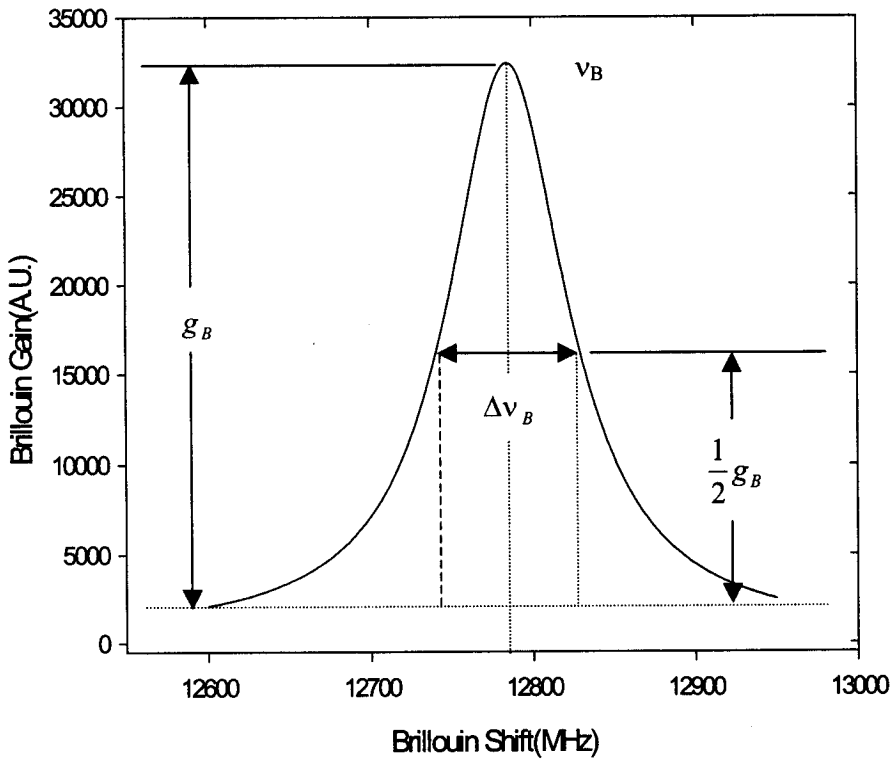

Figure 2.4 A typical Brillouin gain spectrum with a Lorentzian distribution.

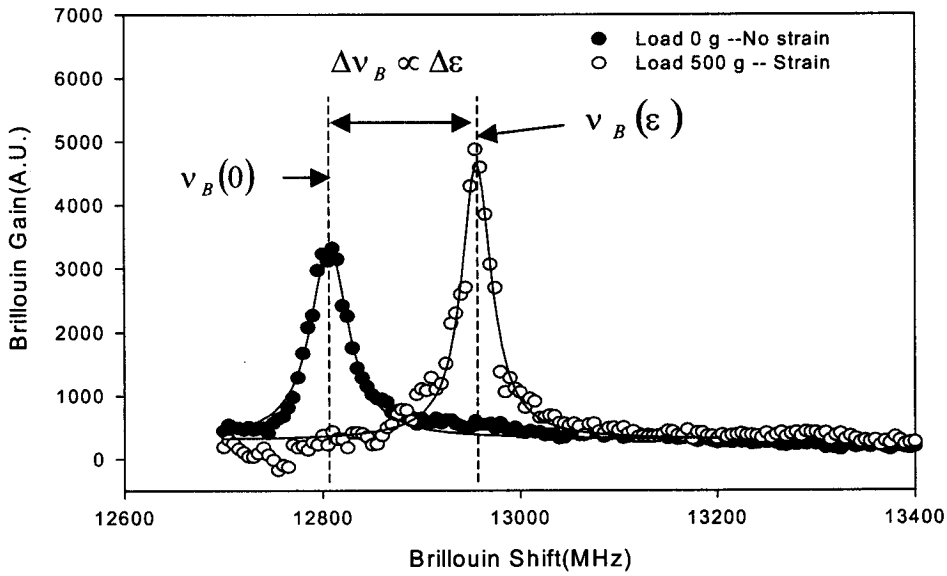

Figure 2.5 A PVC buffered single mode fiber was loaded with a weight of 500 g causing the variation of Brillouin frequency.

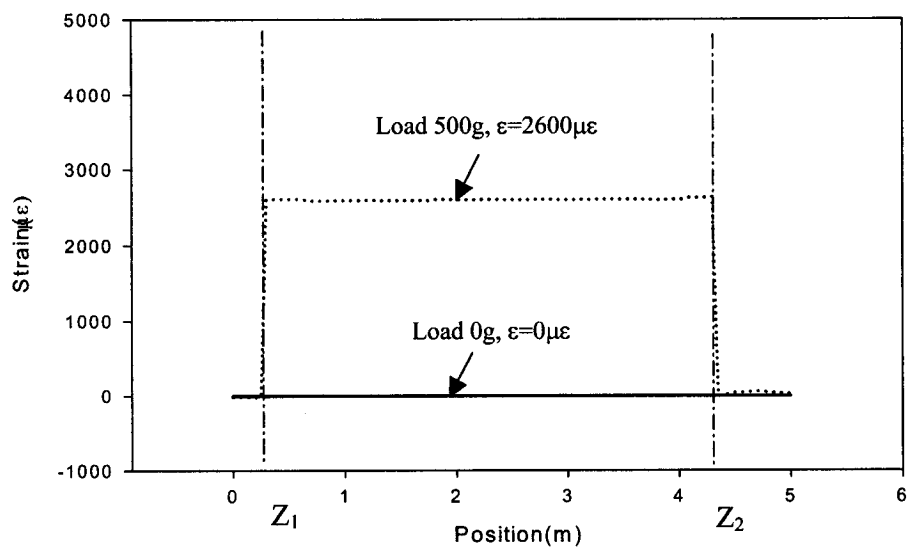

Figure 2.6 Under a weight of 500 g, a uniform strain of 2600 με is generated over the sensing fiber from Z_1 to Z_2.

Chapter 3

Review of Distributed Brillouin Sensing

This chapter will provide a brief overview of the research and history of distributed Brillouin sensors. Several important techniques and configurations of the distributed Brillouin sensing system are also introduced.

3.1 Distributed sensors based on Brillouin scattering

Stimulated Brillouin scattering was first observed in 1964 [Chiao et al. 1964] and since then it has been studied extensively [Agrawal 1995]. Using Brillouin scattering, Rich and Pinnow investigated material properties of optical fibers in 1974 [Rich and Pinnow 1974]. Two years later, optical time domain reflectometry (OTDR) was first reported by Barnoski and Jensen in 1976 [Barnoski and Jensen 1976]. Since distributed sensing techniques allow measurements to be taken along the optical fiber and the spatial information along the fiber is determined with OTDR, it has become an important milestone in the history of development for distributed fiber optic sensors.

3.1.1 Brillouin optical time domain analysis (BOTDA)

The first distributed sensing based on Brillouin scattering was proposed in Nippon Telegraph and Telephone (NTT) in 1989. Horiguchi and his colleagues showed the linear relationship between the Brillouin frequency shift of optical fiber and applied strains. It can be used to measure the Brillouin gain spectrum of an optical fiber in a distributed manner, named Brillouin optical time domain analysis (BOTDA) [Horiguchi, et al. 1989; Horiguchi and

Tateda 1989]. Their initial experimental system included two Nd: YAG CW lasers operated at 1319nm as shown in Figure 3.1, launching a short pump pulse (through an Acousto-Optic Modulator (AOM)) into one end of the sensing fiber and a CW beam into the other end. The frequency difference between the two lasers could be adjusted over several gigahertz ranges while the CW beam would experience power amplification when the frequency difference matched the Brillouin frequency of the fiber. The gain as a function of positions along the fiber could be determined by the time dependance of the detected CW light. So the BOTDA technique could provide temperature or strain distribution along the entire optical fiber.

Almost at the same time, Culverhouse reported the linear relationship between Brillouin shift and temperature in a single mode fiber using a Fabry-Perot interferometer at the University of Kent in England. They found two different fibers had different temperature frequency coefficients, 6.4MHz/°C and 2.67MHz/°C. They showed a clear prospect of a distributed temperature sensor [Culverhouse, et al. 1989].

Kurashima et al demonstrated distributed temperature measurement on a 1.2km long optical fiber with 3°C temperature accuracy and 100m spatial resolution using NTT's BOTDA system [Kurashima, et al 1990].

Several years later, a research group at the University of Kent did many early experimental works on distributed Brillouin sensing using their own BOTDA system and achieved significantly better results. The distributed temperature measurement using Brillouin gain in a 22 km optical fiber was reported by Bao et al. with 1°C temperature accuracy and 10m spatial resolutions [Bao, Webb and Jackson 1993a].

The second development in BOTDA was the use of Brillouin loss based distributed sensing rather than Brillouin gain system. The difference between the gain and loss approach is that the pulsed beam is amplified at the expense of the CW beam; hence the intensity of the CW beam will be reduced [Bao, Webb and Jackson 1993b]. Using the Brillouin loss technique, the system performance was improved with a 32 km sensing length, 1°C temperature accuracy, and 5m spatial resolutions.

Dr. Bao and her colleagues also made distributed strain measurements using the Brillouin loss setup. It resulted in a 5 m spatial resolution and a 20 με strain measurement accuracy in a 22 km optical fiber [Bao, Webb and Jackson 1994a]. They also first reported the Brillouin

loss based simultaneous strain and temperature measurement using two parallel laying sections of an optical fiber; one section subjected to both strain and temperature effects while the other to temperature only [Bao, Webb and Jackson 1994a]. The measurement accuracies were 20 με for strain and 2°C for temperature with a 5 m spatial resolution. Because the pulse signal is not depleted, longer sensing length is available in Brillouin loss mechanism. The 51 km sensing length with 5m spatial resolutions and 1°C temperature measurement accuracy has been reported [Bao, et al. 1995].

Several theoretical studies demonstrated by the research group in the University of Kent focused on the Brillouin amplification process, particularly analytic solutions of the coupled wave equations for Brillouin gain and loss [Bao, et al. 1995] and on the estimation of the Brillouin frequency from noisy spectral data. For fitting spectral data to a theoretical distribution, Dhliwayo, et al. did statistical analysis of temperature measurement errors [Dhliwayo, et al. 1996].

3.1.2 Brillouin optical time domain reflectometry (BOTDR)

In 1992, Kurashima and colleagues at NTT developed a new distributed sensing configuration named as Brillouin optical time domain reflectometry (BOTDR) using coherent detection of the spontaneous Brillouin scattered light rather than detecting a Brillouin amplification signal directly [Kurashima, et al. 1993; Horiguchi et al. 1992]. The basic configuration of BOTDR is illustrated in Figure 3.2. This is a one laser distributed sensing system. The performance of initial BOTDA system was improved by increasing the total sensing length to 11km with 3°C temperature measurement accuracy and 100m spatial resolution. An advantage of this BOTDR system was one end access to the sensing fiber, but a drawback was a wide bandwidth coherent detector of 13 GHz.

A further improvement was reported in 1993 when NTT began to move from BOTDA to BOTDR systems. Shimizu et al. modified the initial BOTDR system by appending a frequency shifter, a second AOM in a ring configuration, into the local oscillator signal. By shifting the frequency at the Brillouin frequency, a much lower bandwidth detector could be used in the BOTDR system [Shimizu, et al. 1993]. There were three obvious benefits: lower

cost and better frequency stability due to one laser, and lack of signal distortion from pump depletion or pulse amplification at the expense of signal strength [Horiguchi, et al. 1995]

The BOTDR system developed by NTT was commercialized and sold as AQ8602 Optical Fiber Strain/Loss Analyzer by the Ando Electric Company, Ltd. The unit has a 100 με strain measurement accuracy and 1-2 m spatial resolution on a 25 km sensing fiber length [Technical leaflet of AQ8602].

3.1.3 Single laser BOTDA configuration

A novel configuration for a distributed Brillouin sensor was developed by the research group at the metrology lab (MET-EPFL) in the Swiss Federal Institute of Technology, Switzerland using a single laser [Niklès, et al. 1994]. The key component of this setup is a $LiNbO_3$ guided-wave intensity modulator (EOM). In this configuration, the light wave of a 1.32 μm diode-pumped single frequency Nd: YAG laser was first split by a coupler. One output of the coupler was injected into the sensing fiber while the light from the other output was launched into the EOM, which was driven by a microwave generator. When a single frequency light is modulated at a frequency ν_m, the modulation gives new frequency lines symmetrical around the incident light or carrier frequency ν_0 in the spectrum, named modulation sidebands. When the modulation frequency ν_m is equal to the Brillouin frequency ν_B, the first-order sidebands can interact with the incident lightwave through Brillouin scattering process, provide that they propagate in opposite directions [Niklès, et al. 1997].

The researchers of the MET - EPFL group made two important improvements to their single laser BOTDA system in 1997. One was using a 1.55 μm laser to replace 1.32 μm diode-pumped single frequency Nd: YAG laser, the other was to make the system single ended [Fellay, et al. 1997]. The simplified configuration of this system was shown in Figure 3.3. By switching to the 1.55 μm light source, the system could use higher pulse power (up to 6 W) in sensing fiber using the Erbium-Doped Fiber Amplifier (EDFA) and fiber has lower attenuation at this wavelength.

The single laser BOTDA system has been packaged into an instrument LASBI 9800 with 1°C temperature measurement accuracy, 20 με strain accuracy, and 1 m spatial resolution for less than 10 km sensing fibers. The system has been used on strain measurement for strong tensile load on a telecommunication cable, temperature distribution measurement on a 60 kV electrical cable, and structural monitoring of a concrete slab on the top of a hydroelectric dam at Luzzone in the Swiss Alps [Thévenaz, et al. 1998].

3.1.4 Brillouin optical frequency domain analysis (BOFDA)

Frequency domain analysis was introduced for fault detection in optical fibers in 1986 [Ghafoori-Shiraz and Okoshi 1986]. A decade later, a new distributed fiber optic sensor based on Brillouin optical frequency domain analysis (BOFDA) was developed by Lehrstuhl für Allgemeine Elektrotechnik und Elektrooptik (AEEO) at Ruhr-University, Germany. The basic configuration of a BOFDA system is provided in Figure 3.4.

BOFDA is based on the measurement of a complex baseband transfer function, which relates the amplitudes of counterpropagating pump and Stokes waves along a sensing fiber [Garus, et al. 1997]. The lasers and fibers are the same as in the previous described approaches. An amplitude EOM was used to modulate the light of the probe laser with a variable modulation frequency f_m. The output signals were fed to a network analyzer (NWA) to determine the baseband transfer function of the sensing fiber. The digitized output signal of the NWA was fed to a signal processor to get the inverse fast Fourier transform (IFFT) [Garus, et al. 1997].

For sensing length and spatial resolution, BOFDA has no disadvantages compared with a BOTDA system. Since the discrete Fourier transform induces additional averaging effects for uncorrelated noise signals, the noise level of BOFDA system is lower than that of BODTA system under same total measurement time. Two drawbacks of the BOFDA system are the relatively long measurement time (since BOFDA system needs more effective averaging time) and the temperature and strain must be constant during the measurement that is impossible to achieve in the field test. Garus, et al. reported the initial test results with the

BOFDA system on an 11km sensing fiber with 1.4m spatial resolution, 1.5°C temperature accuracy and 40 με strain accuracy in 1997.

3.1.5 Landau Placzek ratio

The relation of intensities of the central Rayleigh component (I_R) and the sum of the Brillouin components (I_B) in an optical fiber was first investigated in 1934 [Landau and Placzek 1934]. The ratio I_R / I_B known as the Landau Placzek ratio (LPR) was found for a liquid: $I_R / I_B = (C_P - C_V)/C_V$, where C_P and C_V are the specific heats at constant pressure and constant volume, respectively. It was found experimentally that Landau Placzek ratio in an optical fibre is temperature dependent [Bansal and Doremus 1986].

Wait and Newson in the Optoelectronics Research Center (ORC) at the University of Southampton demonstrated that the Rayleigh/spontaneous Brillouin ratio was used as a temperature sensing mechanism in a distributed sensor system [Wait and Newson 1996; 1997]. Temperature dependent LPR combined with the frequency dependence of the Brillouin backscattering on both strain and temperature indicates a method for simultaneous strain and temperature measurement.

The experimental setup was similar to a single-ended, single laser BOTDA system. The light source of their setup was a distributed feedback laser (DFB) providing about 0.9 mW at 1537 nm. The injection beam of the DFB was modulated to broaden its effective linewidth by an AOM that was gated to produce 6 μs pulses with a 160 μs period and 22ns rise time. The source linewidth was approximately 2 GHz. The output signal from AOM was amplified by an erbium doped fiber amplifier (EDFA). The output was collimated and directed through the scanning Fabry Perot (FP) to separate the Rayleigh and Brillouin components. Lees, et al. reported the initial temperature measurement results over 12.9 km sensing fiber with 2.9°C accuracy and 40 m spatial resolution [Lees, et al. 1997].

3.1.6 Noise initiated Brillouin scattering

The research group at King's College in London reported a technique referred to Noise Initiated Brillouin scattering (NIBS) in 1997. Since Brillouin shifts are both temperature and strain dependent, for simultaneous determination of temperature and strain distribution, the cross-sensitivity of these two parameters should be separated. Parker and colleagues solved strain and temperature effects by simultaneously measuring noise-initiated Brillouin scattering power and frequency shift in optical fibers [Parker, et al. 1997; Parker, et al. 1998]. To normalize the nonlinear Brillouin signal, they presented a new technique to solve this problem through mathematically combining the Stokes and anti-Stokes powers to produce a linear effective power.

3.1.7 Correlation technique

As presented previously, most distributed Brillouin sensing systems use pulsed sources for the probe beam. However, a problem is that the pulsed approach limits the spatial resolution of the Brillouin sensor [Hotate and Tanaka 2001]. The use of an optical pulse stream with the pulse width shorter than the acoustic damping time (or the life time of a phonon) causes the suppression of the Brillouin gain that deteriorates the measurement accuracy. DeMerchant found it is difficult to get the spatial resolution of a Brillouin sensor to better than 10 cm (equivalent to 1ns pulsewidth) [DeMerchant et al 1998].

The researchers of the University of Tokyo introduced a spatial resolution improvement of distributed Brillouin sensing using the Correlation-Based Continuous-Wave technique in 1999 [Hotate and Hasegawa 1999]. This technique is based on manipulating the shape of the optical coherence function of the system and creates a position-selective generation of stimulated Brillouin sensing. The spatial resolution of 1 cm has been achieved for a partly stretched fiber [Hotate and Tanaka 2002].

Their experimental setup is configured as a loop type interferometer shown in Figure 3.5. Using a 3dB coupler, the CW light of a 1.55 μm distributed feedback laser diode (DFB-LD) was divided into probe and pump lightwaves. The frequency of one beam is downshifted by applying a microwave signal to a modulator. The EOMs are used to change the waveform of the frequency modulation or the phase of the beams. Through changing the frequency of the probe modulator, the system creates a Brillouin gain spectrum. By varying the frequency of both probe and pump lightwaves, they shift the correlation peak along the fiber, and obtain Brillouin gain spectrum data as a function of the position [Hotate and Tanaka 2002]. At the position where the correlation peak takes place, the frequencies of the two beams change synchronously and the frequency difference between two beams is kept constant. In this case, the Brillouin gain spectrum takes the same shape of an intrinsic spectrum without the modulation. On the other hand, at the other position where the correlation is low, the frequency of the probe relative to the pump changes continuously, and that results in the suppression of the gain. Stimulated Brillouin Sensing (SBS) was only triggered by the interference at the locations in the fiber where the sensing fiber was under strain, so the high correlation occurs between the probe and pump lightwaves at the spot [Hotate and Hasegawa 1999]. The spatial information was achieved by scanning modulation frequencies for each beat frequency.

3.2 Work of Dr. Bao's fiber optics group

We developed a two-laser BOTDA system based on the research of Dr. Bao at the University of Kent. Many improvements have been obtained over last several years. The system has been used for monitoring strain and temperature distributions on structure and materials, and achieved significant improvements on spatial resolution, measurement accuracy, and conducted field tests.

An automated distributed temperature and strain sensor system based on the Brillouin loss principle was constructed in 1998 (Figure 3.6) with 50 cm spatial resolution and 15 με strain accuracy on a 100 m sensing fiber. To the best of our knowledge, this was the finest spatial

resolution ever achieved with a Brillouin scattering based distributed sensing system at that time [DeMerchant et al.1998; Brown et al. 1998].

Then, DeMerchant et al. reported spatial resolution of 40 cm in the testing of a sensing fiber attached to a simple structural member [DeMerchant et al.1999a]. They reported realistic structural testing rather than simply measuring stretched sections of the sensing fiber for the first time [DeMerchant et al.1999b]. The strain distribution on a simple cantilever beam was measured to an accuracy of better than 50 με with 400mm spatial resolution. The spatial resolution of our DBS system was improved to 10 cm for temperature/strain measurements in 1999 [Brown et al. 1999]

Another important work of our fiber optics group focused on simultaneous strain and temperature distribution measurement with DBS system. There were several techniques developed for DBS systems to separate strain and temperature information, but those were limited theoretically to spatial resolutions approaching 5-10 meters, due to spontaneous scattering used. Smith et al. presented a new technique that could be used at a shorter spatial resolution with pump-probe approach. The relationships between the Brillouin shift and power with respect to strain and temperature were determined for a polarization maintaining (PM) fiber. The experimental results achieved strain and temperature resolution of 178 με and 3.9°C respectively at a spatial resolution of 3.5 m that was a much better performance than previous efforts [Smith 1999; Smith et al. 1999a].

Smith calculated the pulse dependence of the linewidth showing good agreement with experimental results for long pulsewidth (>100 ns) [Smith 1999; Smith et al 1999b]. The experimental results from 10 to 160 ns tended to be narrower than predicted, particularly at the short pulse end of the range due to the steady-state condition in the coupled wave equation. Bao et al made further investigations at pulse widths below 10ns which showed that the linewidth would reach a maximum around 5 ns and was sharply narrowed at pulsewidths below this [Bao et al. 1999]. Lecoeuche et al. using numerical simulations at the University of Kent offered a possible explanation for this result. The effect could be explained by pumping of the phonon field outside of the pulse by EOM's light leakage caused by a non-infinite extinction ratio [Lecoeuche et al. 2000].

An important application of our DBS system was tensile and compressive strain measurement of a steel beam in the lab and field in 2000 [Bao et al 2001]. The strain measurement accuracy was ±10 με in the lab with non-uniform distributed strain and ±5 με for uniform strain. Temperature-compensation [Bao et al. 1994b] was taken into account for strain measurement due to sunlight radiation in the outdoor environment.

We also conducted strain measurement in a concrete beam with single mode fibers embedded in glass fiber reinforced polymer (GFRP) rods and bonded to steel reinforcing bars in 2000 [Zeng et al. 2002]. The strain distributions were measured for one-point and two-point loading patterns for both optical fibers embedded in GFRP rods and those bonded to steel reinforcing bars. In the one-point loading, the strain deviations were ±7 με and ±15 με for fiber embedded in the GFRP rod and bonded to steel reinforcing bars respectively, and ±20 με for the two-point loading. The spatial resolution was 50 cm with 5 cm read-out resolution. Further experimental investigations are given in Chapter 5.

Bao et al. reported the first application for a distributed Brillouin sensor in a composite curing process [Bao, Huang and Zeng 2002]. The DBS system was applied to monitor the strain and temperature variations during the processing of a 177°C – cure carbon fiber/epoxy composite with 15 cm spatial resolution. An optical fiber was embedded within the mid-ply of 16-ply panel to measure in-situ temperature and in-plane strain simultaneously. A net strain profile corresponding to the different stages of the curing process was generated [Huang et al. 2001]. The details are depicted in Chapter 6 of this thesis.

Health monitoring of civil structures is one of many focuses in application of distributed fiber optic sensors. Zeng et al. presented the preliminary results of strain and temperature monitoring of a nuclear containment structure with their DBS system [Zeng et al. 2002a]. The experiment was remotely conducted for 12 hours in the field with total 1.1 km fiber length in 2001. An 18 cm spatial resolution and ±50 με strain resolution were achieved. The details of this experiment are demonstrated in Chapter 7.

The first temperature compensated strain measurement with the distributed Brillouin sensor was applied by our group in the load test on the Rollinsford Bridge, Rollinsford NH [Zeng et al. 2002b]. The strain distribution of the bridge deck as a function of the loading, location and time has been monitored continuously during load tests of the bridge with a 15 cm spatial

resolution. The strain resolution is ±25με (μm/m). The details of this experiment are also discussed in Chapter 7.

A new application of our DBS system is fire detection that requires remote surveillance combined with short response times to minimize and isolate the impact of a potentially hazardous fire. Distributed Brillouin sensing is thought to be most appropriate for fire detection due to its enormous potential for monitoring remote locations with increased temperature sensitivity. However, fire detection requires the processing time of several seconds instead of the order of minutes that the DBS system operates in normal applications. We presented the Brillouin scattering based distributed temperature sensing for fire detection at 7th International Symposium on Fire Safety Science, Worcester, Massachusetts, USA, in June 2002 [Liu et al. 2002]. By directly measuring the intensity of the Brillouin gain/loss signal versus time, the Brillouin system can respond more quickly to changes in fiber temperature, while maintaining good spatial and temperature resolution and high signal-to-noise ratio (SNR>20dB). In this experiment, a setup including DBS system was used for measuring the Brillouin intensity versus time for real-time temperature measurements. An 11 km single mode fiber was interrogated by 20 ns pulses (2 m spatial resolution) to monitor the temperature variations in a 10 m sensing fiber. Test results showed the potential for applying DBS technique in practical fire detection schemes through the use of a threshold temperature that corresponds to the maximum Brillouin intensity.

3.3 Development in past five years

In section 3.1 we had introduced several configurations and techniques of distributed Brillouin sensors in the past fifteen years. More research groups have involved in distributed Brillouin sensing on theoretical research, system developments, error analysis, and technical applications in the past five years. These applications involve many fields, especially in the civil engineering area. A brief summary is given in this section.

3.3.1 Simultaneous strain and temperature measurement

Simultaneous strain and temperature measurement was one of new focuses in past several years. Using a spontaneous Brillouin sensor, Parker et al. at King's College reported their test results with 100 με strain resolutions, 4°C temperature resolution, and 40m spatial resolutions over a 1.2 km sensing fiber in 1998 [Parker, et al. 1998]. Both in 1999, the experimental results were achieved in Bao's group shown strain and temperature resolution of 178 με and 3.9°C respectively at a spatial resolution of 3.5 m on 50 m PM fiber [Smith 1999; Smith et al. 1999a]; NTT's results of separating temperature and strain over a 100m fiber with a 1m spatial resolution were 260 με and 11°C [Ohno et al. 1999]. Simultaneous measurement of strain and temperature was demonstrated by ORC with 290 με and 4°C accuracy and a 10 m spatial resolution on 15 km fiber length [Kee et al. 2000a]. A new research group at National Chiao-Tung University (NCTU) in Taiwan provided the test results with 5°C and 60 με resolutions and 2 m spatial resolution in a 3.7 km large-effective-area nonzero dispersion-shifted fiber [Lee et al. 2001]. Simultaneous strain and temperature measurement results achieved by different research group are summarized in Table 3.1.

Table 3.1 Summary of simultaneous strain and temperature test results achieved

Research Group	Achieved Time	Strain Resolution	Temperature Resolution	Spatial Resolution	Fiber Length	Mechanisms
King's U	1998	100 με	4°C	40 m	1.2 k m	NIBS
Bao	1999	178με	3.9°C	3.5 m	50 m	BOTDA
NTT	1999	260με	11°C	1 m	100 m	BOTDR
ORC	2000	290με	4°C	10 m	15 km	LPR
NCTU	2001	60με	5°C	2 m	3.7 km	BOTDR

3.3.2 Improvement of the theory and systems

The works of both Dr. Bao's fiber optics group and the research group at NTT have been focused on improvement of the distributed Brillouin sensing system and field applications for recent years. The details of the works by Dr. Bao's fiber optics group will be presented in the following chapters.

NTT improved their BOTDR Optical Fiber Strain Sensor/Loss Analyzer. They used a new configuration for Brillouin scattered signal detection that had no frequency-shifting device required [NTT NEWS RELEASE 2001]. The detection of the scattered light, namely, optical and electrical heterodyne detection include two steps. Similar to the approach used with the conventional sensor, Brillouin scattered light was first detected. An electrical intermediate output that was over 10 GHz frequency range was extracted. Second, using an electric local oscillator, the intermediate output was heterodyne-detected electrically. The new sensors have strain accuracy of 0.003% (30 με) and reduced the required measurement time from approximately 10 minutes to 5 minutes. The sensing length was kept on 10 km similar to that of the conventional sensors with 1m spatial resolution.

Lee and Chi at National Chiao-Tung University in Taiwan investigated SBS threshold of various types of fibers both theoretically and experimentally using BOTDR. The fibers included standard single mode fiber (SMF), large-effective-area dispersion-shifted fiber (LEAF), True Wave/Reduced Slope fiber (TWF), and conventional dispersion-shift fiber (DSF). The reported SBS threshold differences are 2.06, 1.10, and 1.09 dB for LEAF/SMF, SMF/DSF, and DSF/TWF, respectively [Lee and Chi 2000].

A spontaneous Brillouin-based distributed temperature sensing system using a short-pulsewidth laser source at 1.5 μm was introduced by Kee et al at the Optoelectronics Research Center (ORC), University of Southampton, UK in 2000 [Kee et al 2000b]. A 35 cm spatial resolution and 4.3°C temperature resolution were achieved over 1 km single mode fiber. In 2001, Maughan et al at ORC reported a calibrated 27-km distributed fiber temperature sensor based on microwave heterodyne detection of spontaneous Brillouin backscattered power. The spatial resolution was 20m and the rms errors in power were 1%-1.2%, corresponding to a temperature error of between 2.8 K and 3.4 K over 27 km optical fibers [Maughan et al

2001a]. At the same time, they presented 57-km single-ended spontaneous Brillouin-based distributed fiber temperature sensor using microwave coherent detection [Maughan et al 2001b]. The rms error in frequency measurements was less than 3 MHz at the far end of the sensing fiber with a spatial resolution of 20m. The overall frequency dependence on temperature was 1.07 ± 0.06 MHz/K.

Loayssa et al at Universidad Pública de Navarra, Spain introduced a new technique for SBS spectral characterization. This technique can provide accurate measurements of the amplitude and phase of the both Brillouin gain and loss spectra with high frequency resolution and stability. The working principle was based on translating the Brillouin spectral information from the optical to the electrical domain. Since the Brillouin spectra were scanned by sweeping an electrical rather than optical carrier, the frequency resolutions of the measurements could be in kilohertz range. The experimental setup relied on a Brillouin-erbium fiber laser to generate the optical signals [Loayssa et al. 2001].

Hotate and his colleagues at the University of Tokyo improved their correlation-based continuous wave technique of fiber Brillouin distributed strain sensing with cm order spatial resolution. The testing results show the technique is applicable to smart structures of materials to monitor strain distribution [Hotate and Tanaka 2001; Tanaka and Hotate 2002; Hotate and Tanaka 2002]

A novel frequency-domain approach to distributed fiber-optic Brillouin sensing was presented and numerically analyzed by Bernini et al in Italy. An integral equation, which related the Brillouin gain to Brillouin signal directly, was derived in the frequency domain. Based on this result, a new technique for the quantitative reconstruction of temperature-strain profiles along an optical fiber was developed [Bernini et al. 2002].

Fotiadi et al. performed numerical simulations to obtain statistical and spectral characteristics of SBS initiated by Gaussian noise in single-mode fibers [Fotiadi et al. 2002]. They gave a clear physical insight into the one-dimensional model of the experimental spectra of SBS power and revealed how the probability function of Stokes power, the power-correlation function, and the SBS spectra evolve as key parameters of the model vary, leading to a modification of Stokes field statistics.

In order to obtain a clear picture of the developing history of BDS, we summarize the distributed Brillouin sensing systems developed by several research groups in Table 3.2.

Table 3.2 Summary of the development of distributed Brillouin sensing systems

Group	Time	Function	Mechanism	Accuracy
NTT	1990	T	BOTDA	3°C, 100m, 1.2km
	1992	T	BOTDR	3°C, 100m, 11km
	1997	ε		60με, 1m, 10km
	2001	ε		30με, 1m, 10km
Bao	1993	T	BODTA	1°C, 10m, 22km
	1993	T	(Brillouin loss)	1°C, 5m, 32km
	1994	ε		20με, 5m, 22km
	1994	T + ε		2°C, 20με, 5m, 22km
	1995	T		1°C, 5m, 51km
	1998	ε		15με, 0.5m, 100m
	1999	ε		50με, 0.4m, 100m
	2001	ε		10με, 0.5m
	2002	ε		25με, 15cm
EPFL	1998	T, ε	BOTDA (One laser)	1°C, 20με, 1m, 10km
AEEO	1997	T, ε	BOFDA	1.5°C, 40με, 1.4m, 11km
ORC	1997	T	LPR	2.9°C, 40m, 12.9km
	2000	T		4.3°C, 34cm, 1km
	2001	T		2.8-3.4K, 20m, 27km
King's	1997	T+ε	NIBS	4°C, 100με, 40m, 1.2km
Tokyo	1999	ε	Correlation	45cm, 28m

3.3.3 Field application

There are many research groups who have produced theoretical and experimental works on distributed Brillouin sensing in recent years. However, most of experiments were conducted in the laboratory, only a few of them were carried out on real structural monitoring and in the field. Table 3.3 presents the realistic applications done by several research groups.

Table 3.3 Applications of Distributed Brillouin sensing

Group	Application	Specification
Bao	7 m Steel Beam	Compression, tension Temperature compensation Resolution: 0.5m, ±10με
	Concrete Beam	Compression, tension; one and two point load; FRP rod, Steel bar Resolution: 0.5 m,±7 ~ 20με
	Composite Curing Process	Strain and temperature variations Resolution: 0.5 m
	Nuclear Containment Structure	Strain, Temperature, 1.1km fiber Resolution: 18 cm, ±50με
	Rollinsford Bridge	Load test, Strain, T compensation Resolution: 15 cm, ±25με
	Fire Detection	Real-time T measurements, 11km fiber, 2m resolution
EPFL	60 kV Electrical Power Cable*	Temperature, destructive overheats, localized hot spots #
	Concrete Setting Temperature, A slab of Dam, Swiss Alps *	Two-dimensional temperature distribution #
	Temperature Change of Deep Waters Bed of the Lake of Geneva, Swiss* *[Thévenaz, et al. 1998]	Temperature change with seasonal conditions # Resolution: 1m, ±20με, ± 1°C
NTT	Concrete Beam [Kurashima et al. 1997]	10×0.4×0.5m length, 5 tons Load test, Distributed strain measurement Resolution: 1m, ±60με
	An Aluminum Tube [Kurashima et al. 1997]	60mm diameter, 18m length Strain distribution for several loads Resolution: 1m, ±60με
	Nippon Challenge's Yacht [Ohno et al. 2001]	Hull-damage detection, Strain distribution Resolution: 1m, ±30με
	River Levee [Ohno et al. 2001]	Long term strain monitor, detecting the collapse Resolution: 1m, ±30με
	Concrete Structures [Ohno et al. 2001]	Embedded fiber, Strain distribution Resolution: 1m, ±30με
U of Tokyo	Smart Materials [Tanaka and Hotate 2002]	Acryl ring, strain distribution, load test, ϕ15.7cm, thickness 32.nn, width 4cm, spatial resolution 1cm
KAIST Korea	8m Aluminum Beam [Kim et al. 2001]	Three-point Bending experiment, Resolution: 16.8με, temperature influence 20με/°C

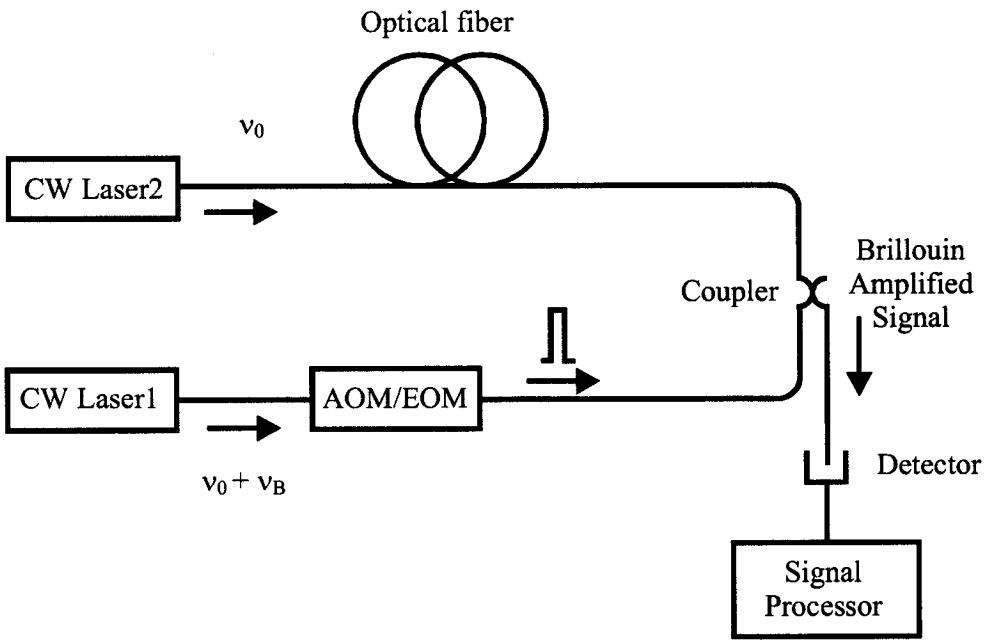

Figure 3.1 BOTDA configuration.

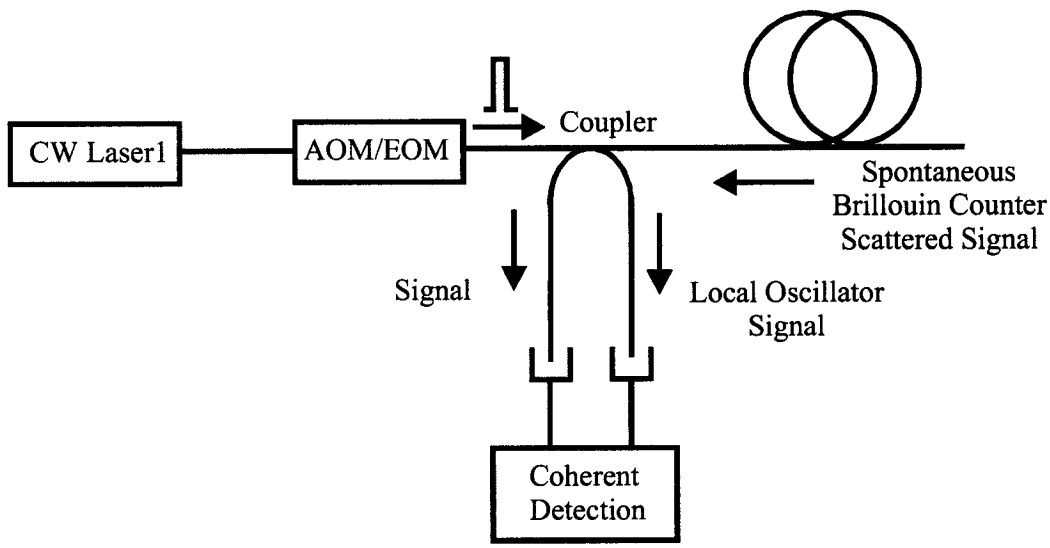

Figure 3.2 BOTDR configuration

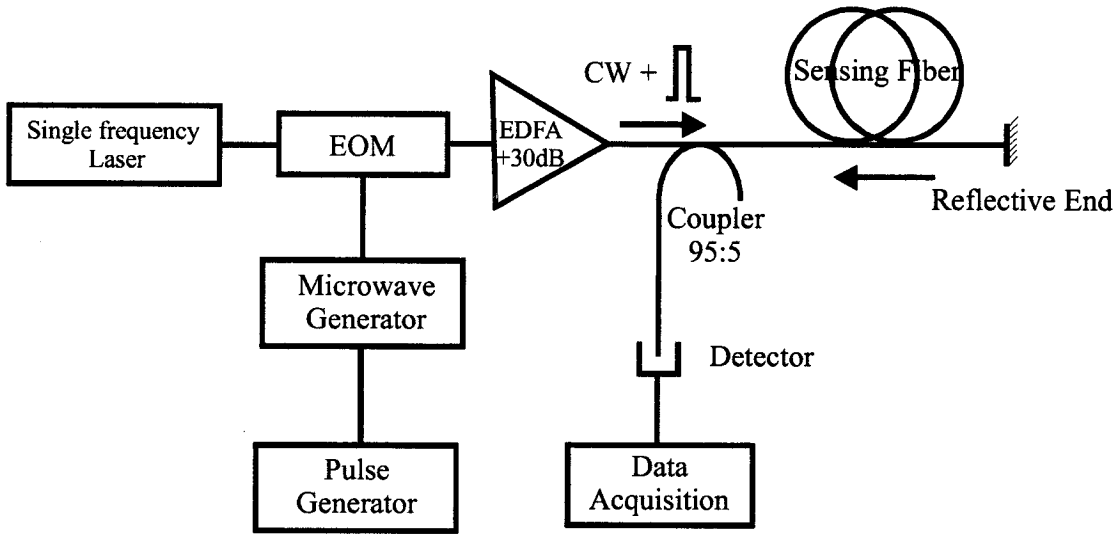

Figure 3.3 Single laser, single-ended BOTDA system

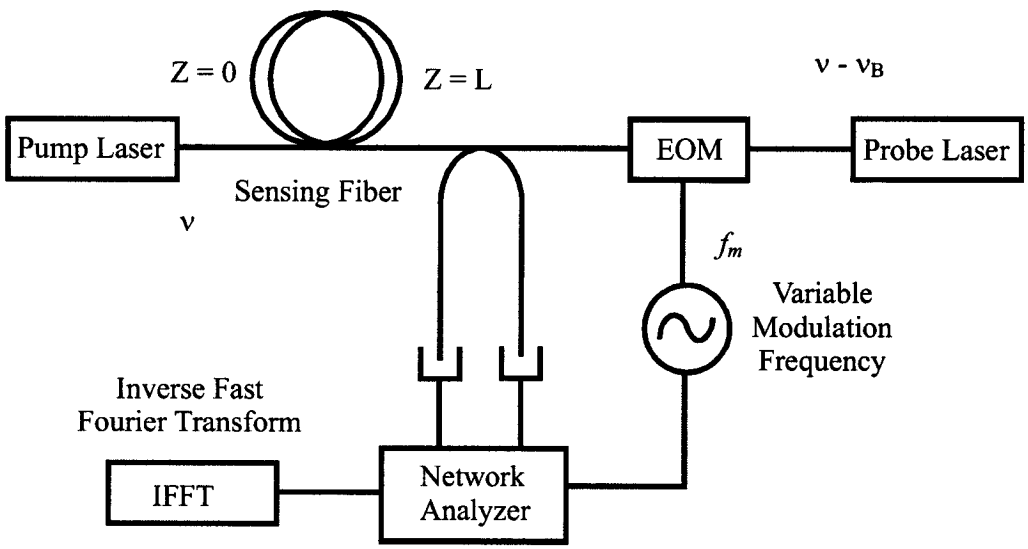

Figure 3.4 Basic configuration of a BOFDA system

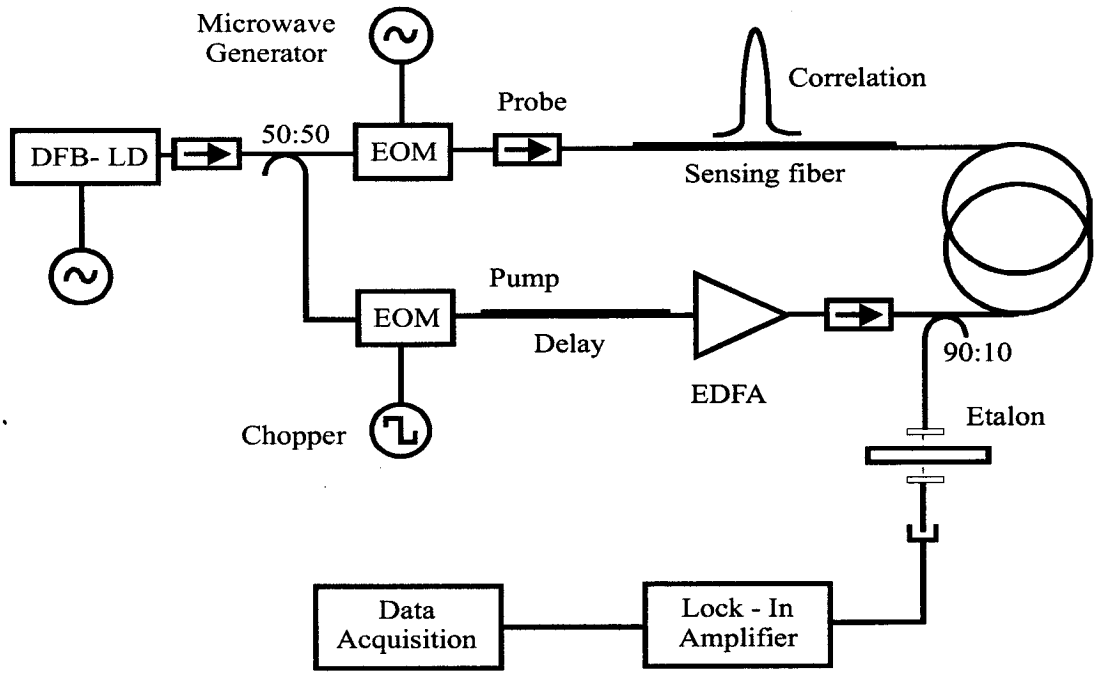

Figure 3.5 Distributed Brillouin sensing base on the Correlation Technique

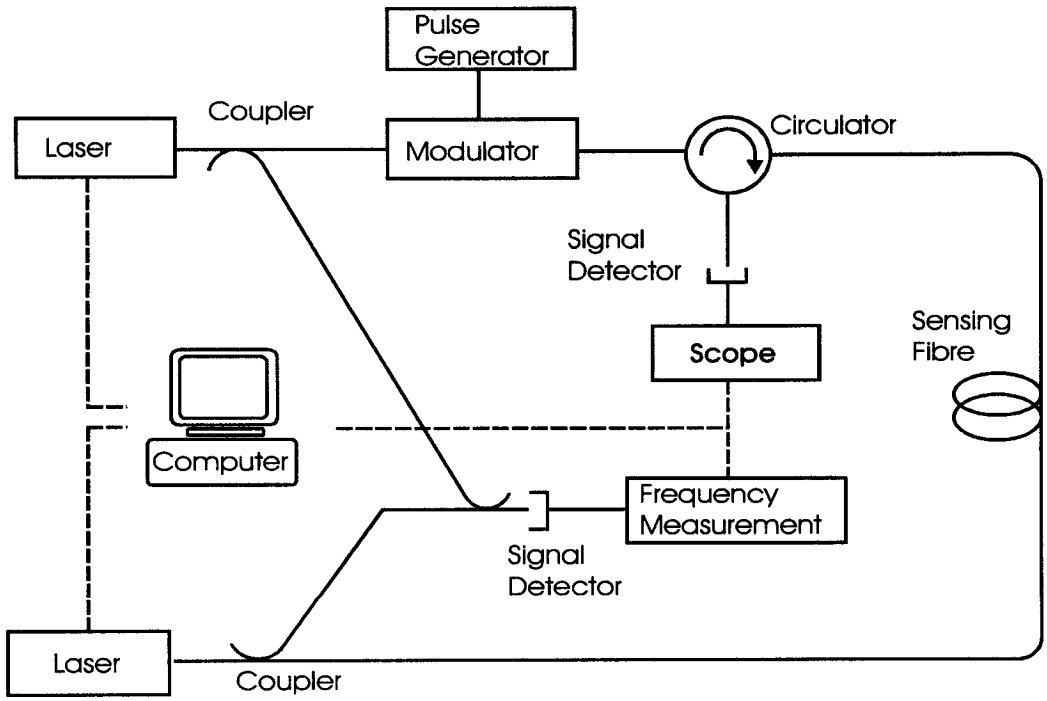

Figure 3.6 Initial automatic Brillouin loss based BOTDA system developed in our group

Chapter 4

Characterization and Optimization of Distributed Brillouin Sensing System

To evaluate the performance of an equipment or a measurement system, it is important to examine its measurement accuracy and repeatability. The performance of the distributed Brillouin sensing (DBS) system is related to a few factors, such as stability of laser sources and electrical power supplies, the noise of the detectors, polarization states of the light beams, Signal-to-Noise Ratio (SNR), bias level of the Electro-Optic Modulator (EOM) and the pulsewidth of the pulse generator. In this study we focus on some parameters around pulse generation subsystem and study measurement uncertainty and repeatability of DBS system.

4.1 Introduction

The UO's DBS system is made of four major subsystems. They are laser control, pulse generation, sensing, and computer control subsystems. Pulse generation subsystem consists of all components required to generate and monitor laser pulses in DBS system [DeMerchant 2000]. Figure 4.1 shows the configuration of this subsystem.

In this subsystem an AVTECH high-speed pulse generator is used as a driver for a 12 GHz electro-optic modulator working at 1319 nm. A 10MHz function generator provides an electrical trigger to the pulses. The EOM produces optical pulses from a CW input light beam by modulating the amplitude of the beam in response to the electrical pulse from the pulse generator. Four main parameters will impact the performance of the pulse generation subsystem. They are bias of EOM, pulsewidth, amplitude and repetition frequency of optical pulses.

We could manually preset the amplitude and repetition frequency of output pulses before the DBS system start working. The pulsewidth of electrical trigger pulse and output optical pulse are adjusted with the pulse width (PW) voltage provided by the computer board. The computer also controls the electrical bias of EOM. Both PW voltage and bias can be set and held steady with the software developed by our fiber optics group. The amount of probe power allowed through the EOM could be controlled by EOM bias when no pulse is being emitted. Higher bias settings in the linear region increase the signal level at the expense of distorting the time domain waveforms [DeMerchant 2000].

The determination of the optimum value of the EOM bias was one of the main purposes of this project; that is a bias level to generate optical pulses in channel A with a biggest SNR, while maintaining reasonable optical power (>160 nW) in channel B. It was found when the power of channel B is lower than 160 nW, the frequency counter fails to function properly. As expected, bias was found playing a very important role for the performance of the system. Bias changes will induce the variations of SNR, the optical pulsewidth, peak powers, and leakages of the pulse in two channels. One can see that at the bias setting corresponding the biggest SNR in channel A, the Brillouin sensing system has optimum performance.

The second goal of this study was to find the relationships among the major EOM output parameters (such as peak power, leakage, pulsewidth and extinction ratio) and the controllable variables (for example, bias, PW voltage, amplitude, and RF frequency). The third goal was to evaluate the performance of DBS system in terms of repeatability, the influence of different bias, comparison of one-and-two-laser frequency locking on the measurement accuracy.

4.2 Experimental research on EOM

4.2.1 Classification and application of EOM

EOM allow us to electrically control the amplitude (intensity) and phase of an optical beam. They are normally used in communication and measurement systems. There are three ways to modulate the light through electro-optic modulators: amplitude, frequency, and phase.

Amplitude modulators can be further grouped into analog and digital devices. In conformity with the operating types, EOM can be separated into bulk modulators and integrated optic modulators. Made with waveguide technology integrated optic modulators are wavelength specific, fibers pigtailed and compact.

The simplest integrated modulator is the phase modulator that consists of an optical waveguide between two electrodes. When a voltage is applied to the electrodes, the refractive index of the waveguide will change due to the electric field in that region. It results in a delay of several optical periods of the light passing through the EOM as defined [UTP 1997]:

$$\Delta\Phi = \pi \cdot \frac{V}{V_\pi} \tag{4.1}$$

where $\Delta\Phi$ is optical phase shifts, V is the voltage applied to the electrodes, and V_π is the switching voltage at which the delay is half a cycle of the light.

Phase modulators can be used to mode lock a laser or to stabilize the frequency of a laser beam. It is most important that phase modulation cannot be separated from frequency modulation. The instantaneous frequency of a periodic signal is defined as the time derivative of the overall phase of the signal [Udd 1991].

$$f(t) \equiv \frac{1}{2\pi} \cdot \frac{d\Phi(t)}{dt} = \frac{1}{2\pi}\left[\omega + \frac{d\phi(t)}{dt}\right] \tag{4.2}$$

where $f(t)$ is the instantaneous frequency, ω is the optical frequency, and $\phi(t) = m \cdot \sin \Omega t$ is the signal's global phase. Here m is the phase-modulation index. For a given phase modulation, sinusoidal phase modulation results in sinusoidal frequency modulation at a fixed frequency Ω with a $\pi/2$ phase lag and a peak-to-peak excursion of $2m\Omega$. This frequency modulation property makes phase modulation useful in laser mode locking [Siegman 1986].

Amplitude modulators have two major forms: the Mach-Zehnder (single output) Modulator (MZM) and Y-fed Balanced Bridge (dual output) Modulator (YBBM). Normally amplitude modulators can produce a pulse stream from a CW laser beam.

A Uniphase Y- balanced bridge modulator (YBBM) is used in UO's DBS system. It's a typical integrated optical amplitude (intensity) modulator with Mach-Zehnder interferometer configuration. For this reason, we will discuss integrated optic modulators in the following sections.

4.2.2 Working Principle of EOM

The EOM works on the principle of the linear electro optic effect that produces a change in the refractive index, which is proportional to an applied external electric field [Yariv 1984]. The effect of an applied electric field on the refractive index of a crystal has the form:

$$\Delta n = n_0^3 r \frac{E}{2} \tag{4.3}$$

where Δn is the change of the refractive index, E is an applied electric field, n_0 is initial refractive index that is not disturbed, and r is the appropriate element in the electro-optic tensor.

Integrated optic modulators are made of waveguides in materials that exhibited the electro optic effect. Lithium niobate ($LiNbO_3$) is one of the most suitable materials for infrared fiber optic applications, because of its high electro optic coefficient. Replacing the lithium with Annealed Proton Exchange (APE^{TM}) or titanium-diffused, a waveguide can be formed in the lithium niobate substrate. Waveguides are formed when carefully dimensioned areas of the niobate substrate are processed, forming regions of higher refractive index [UTP 1997].

The integrated optic phase modulator is the simplest modulator. It is constructed with setting a dielectric optical waveguide between two electrodes by which the refractive index can be controlled via the linear electro optic effect (Figure 4.2). When a voltage is applied to the electrodes, an electric field is formed that causes a change of the refractive index in the waveguide. Light traveling through the waveguide will experience a propagation delay equivalent to the phase change in the output light. The phase change can be written as:

$$\Delta\Phi = \omega\Delta t = (\Delta n \omega L)/c \tag{4.4}$$

where Δn is the change refractive index, ω is the optical frequency, Δt is a change of the propagation delay, L is the interaction length, and c is the speed of light in vacuum.

The configuration of Mach Zehnder Modulator (MZM) and Y Balanced Bridge Modulator (YBBM) are shown in Figure 4.3 and Figure 4.4. Integrated amplitude modulators are constructed by patterning a Mach-Zehnder interferometer on a $LiNbO_3$ substrate. In comparison with phase modulators, amplitude modulators differ in two important ways. First, a V_{Bias} electrode is used to control the output power. Second, the input optical waveguide is separated into two paths as the two arms of the Mach-Zehnder interferometer and then recombined before output. Opposite electric fields increase the refractive index in one path while decrease it in another path, causing a relative phase shift in opposite directions. The relationship between the output optical power P_{out}, input power P_{in}, and the phase change $\Delta\Phi$ for an ideal integrated amplitude modulator is written as

$$P_{out} = \frac{P_{in}}{2}[1 + \cos(\Delta\Phi)] \tag{4.5}$$

For linear operation, amplitude modulators are normally biased at the half-power point as shown in Figure 4.5.

The difference between the Y Balanced Bridge Modulator and the Mach Zehnder Modulator is a 3dB coupler designed at the recombination point. This coupler provides a complementary optical output at two output fiber pigtails. Both outputs can be used for signal transmission. An important benefit of the second output is that it can be used for a feedback control system to monitor and stabilize possible thermal drift and minimize harmonic distortion.

As shown in Figure 4.4 and Figure 3.1, in the UO's DBS system the input PM fiber of Y Balanced Bridge Modulator connects directly to the CW laser. When a negative electrical trigger pulse is applied to EOM's RF electrode, we can get complementary optical outputs at two output pigtails; a positive pulse is used for probe signal while a negative pulse can be used as the power tap for the beatnote. Since no tap power is necessary between the laser and EOM, this method can reduce the insertion loss of a directional coupler and its connectors [Brown 2000].

4.2.3 Experimental setup

In order to study the performance of the Y Balanced Bridge EOM in UO's DBS system, an experimental apparatus was used in this project as shown in Figure 4.6. The light source was a tunable Nd: YAG laser beam operating at 1319 nm with 200mW peak output power. The complementary optical pulses were created using a Uniphase YBBM modulator driven by an AVTECK AVMP-2-EW pulse generator. Bias is provided by a stable DC power supply. An attenuator was used for protection; making sure that a limited, safe optical signal reached the detectors. Peak power, leakage and pulsewidth of the optical pulses from EOM's two output fiber pigtails were analyzed with a Tektronix TDS784A oscilloscope.

There are four major variables in this project: bias for EOM, input pulsewidth, amplitude, and repetition frequency of the electrical trigger pulse. Table 4.1 showed the details of those variables. Six electrical trigger pulsewidth were chosen in this experiment: 1ns, 5ns, 10ns, 20ns, 40ns, and 60ns.

Table 4.1 Variables and operating range

Variables	Operating Range
Bias	0 ~ ±15V DC
Electrical Pulsewidth	0.2 ~ 100 ns for AVTECH AVPP-1-C 0.3 ~ 2.0 ns for AVTECH AVMP-2-EW-
Amplitude	0 ~ 10V for AVTECH AVPP-1-C 0 ~ 20V for AVTECH AVMP-2-EW-
Repetition Frequency	1 ~ 10MHz

4.2.4 Experimental results

The test was performed for one and half months. During the test, some interesting relationships were found between the peak power, leakage, pulsewidth, and extinction ratio.

The extinction ratio is defined as the ratio of two optical power levels, $r_e = P_1 / P_2$, where P_1 is the optical power level generated when the light source is "on," and P_2, the leakage is the power level generated when the light source is "off." (*Note:* The extinction ratio may be expressed as a fraction or in dB). In this test, P_1 is the peak value of optical powers at one of the output channels of the EOM and P_2 is the leakage of the same channel. From Figure 4.7 to Figure 4.12, we can find the peak power, leakage and extinction ratio are changed periodically with the bias. It is because of the electric field applied to the two paths of the waveguide on the lithium niobate crystal are different with the bias. The light traveling through this material will experience a change in propagation delay. The output power is changed periodically with input power multiplied by $[1+\cos(\Delta\phi)]/2$ as expressed in section 4.2.2. The details will be discussed in following sections.

The role of bias

From Figure 4.7 and Figure 4.8 we find the complementary peak powers and leakages of optical pulses for both channel A and channel B. The peak powers and leakages changed periodically with the bias. The periodicity is around 10.5V. Those results were obtained in the lab with fixed repetition frequency of the trigger pulses at 10kHz, amplitude of 8V and pulsewidth of 1ns.

The very interesting relationship between peak power, leakage, and shape of the optical pulse for the EOM's output were illustrated in Figure 4.9. Here optical pulsewidth was set to 1ns, while the repetition frequency is at 10kHz, and amplitude at 8V. First we see that at any point along the horizontal direction when the peak output is bigger than leakage we get a positive pulse, otherwise we will get negative pulse. Second, around maximum and minimum power points: 1.8V, 7V, and 12.9V, very broad optical pulsewidth can be found. There is no optical pulse appearance at two curves crossed points, since the peak power is equal to the leakage. Third, near half-power point, we get highest pulse power with given pulsewidth. For linear operation, an amplitude EOM is often biased at the half-power point. Fourth, as bias voltage drifts to cross the minimum power (around 2.8V and 14V), we get the minimum

leakage and maximum extinction ratios, which is the best operation point for our distributed Brillouin sensing system.

Figure 4.10 represents the relationship between the peak power, leakage, and extinction ratio for EOM's output channel A and channel B. One important point is that the bias voltage for maximum output is not the same as the voltage for the high extinction ratio. The highest output power corresponds to the minimum extinction ratio, and the bias voltage for maximum extinction ratio is the same as the bias voltage for minimum leakage power. The best working bias is 2.8V for channel A and 8.5V for channel B. Around those points the trade-off for peak outputs, minimum leakages and best extinction ratios is optimized.

Figure 4.11 illustrates peak powers, leakages, and extinction ratios for channel A and channel B for the case of 5ns pulsewidth. The best extinction ratio points are –8.5V and +2.8V for channel A and –2.7V and +8.5V for channel B.

Table 4.2 provides the bias values at the highest extinction ratio for different optical pulsewidth. Obviously the bias voltages of 2.8V (channel A) and 8.5V (channel B) are the best choices for high extinction ratio.

Table 4.2 Bias for the highest extinction ratio with different pulsewidth

Pulsewidth	Channel A		Channel B	
	Bias (V)	Extinction ratio	Bias (V)	Extinction ratio
1ns	2.8	225	8.5	68
5ns	2.8, - 8.5	380	8.5, - 2.7	82.5
10ns	2.8	320	8.5	300
20ns	3.5	185	8.5	300
40ns	2.8	410	8.5	330
60ns	2.8	290	8.2	340

Bias and pulsewidth

From the experiment, we have noticed that optical pulsewidth changes with biases for small pulsewidth (< 2ns) when the electrical pulsewidth and driving power are fixed. Since it is difficult to set a Brillouin sensor to better than 1 ns temporal accuracy [DeMerchant et al. 1998], we chose 1ns electrical pulsewidth as the shortest pulsewidth. Amplitude of the trigger pulse was fixed at 12 volts and 10kHz repetition frequency was used. The optical pulse widths at the EOM's two output pigtails were recorded with bias changing from 0 to 10 V as shown in Figure 4.12. We can see that optical pulsewidth changes periodically with bias in every 5V and were inversely proportional to bias. The pulsewidth jumping points around 5V were pulse polarity changing points. The pulsewidths are only about 0.75ns at the bias of 2.8 V for channel A and 8.5 V for channel B when we set the electrical pulsewidth at 1ns.

It's well known that any electrical or optical pulses do not have a rectangular shape. They have both rise and fall times that will be 5~20 percent of the pulsewidth in the small pulsewidth case (< 2ns). Table 4.3 compares the rise time and fall time of two pulse generators used in this project. When the pulsewidth is small enough (shorter than the sum of rise time and fall time), a thin triangular will replace the trapezoid. In this case, a big measurement error will be induced from the peak power drifts and variation of the optical pulsewidth.

Table 4.3 Comparison of rise time and fall time of two pulse generators

Pulse generator	AVP-AV- (0.3-2ns)	AVMP-2 (5-100ns)
Rise time T_r	≤ 100 ps	≤ 100 ps
Fall time T_f	≤ 200 ps	≤ 135 ps
Polarity	Positive and negative	

Note: the rise and fall time are the interval between the 20% and 80% amplitude points on the leading and trailing edges of a pulse.

Table 4.4 compares the percentage of $(T_r + T_f)/FWHM$ and maximum relative errors of the optical pulsewidth around the polarity changing points of the optical pulses. The same

variation tendency can be found for both of them and are inversely proportional to the electrical pulsewidth.

When the electrical pulsewidth is longer than 10 ns, the pulse shape is nearly rectangular and the changes of the optical pulsewidth with the bias can be normally neglected except where the pulse changes polarities. When the electrical pulsewidth is smaller than 2 ns, the pulse shape is a thin trapezoid or triangle and the errors of the optical pulsewidth are larger than twenty-five percent. This will be an important error source of the sensing system.

Table 4.4 Percentage of $(T_r + T_f)/FWHM$ and relative errors of the optical Pulsewidth around the polarity changing points of the optical pulses

Electrical pulsewidth ($FWHM$)	$\frac{T_r + T_f}{FWHM} \cdot \%$	$\Delta\%$
1 ns	30%	60%
2 ns	15%	25%
5ns	4.7%	10%
10 ns	2.35%	5%

Note: $\Delta\%$ is the maximum relative errors of the optical pulsewidth around the optical pulse polarity changing points.

The power of an optical pulse is proportional to the area under the profile of the pulse shape. For the rectangular pulse case, the peak power variation with the bias does not cause an obvious change of the pulsewidth. However, for the triangular or trapezoid pulse shape, any variation of the peak power with the bias will cause the fluctuation of the optical pulse duration. This is the main cause of the pulsewidth variation with the bias, and the shorter the electrical pulsewidth, the larger fluctuation of the optical pulsewidth. Furthermore, the biggest pulsewidth error takes place around the pulse polarity changing points. It is due to the EOM biasing occurring at a nonlinear working region.

PW voltage and pulsewidth

A near linear relationship between electrical pulsewidth and the PW voltages can be found in Figure 4.13. In this case we used a WAVETEK Model 29 10MHz DDS function generator providing the electrical signal to trigger the pulse generator and held the repetition frequency at 10kHz. For different amplitudes of electrical pulse, a set of curves was obtained according to the test data. The available electrical pulse region is 0.4-3.5ns. There are big noises as the PW voltage is lower than 2V.

Similar linear relationships between the PW voltages and optical pulsewidth obtained at EOM's two output channels are shown in Figure 4.14 with the bias of 2.8V at Channel A and 8.5 V for both Channel A and B. We find optical pulsewidth is proportional to PW voltage when bias and amplitude of electrical pulse are fixed. At a fixed PW voltage point the optical pulsewidth is inversely proportional to the amplitude. Again, the power of a pulse stream is proportional to the area under the profile of the optical pulse that approximates to a pulsewidth multiplied by the peak power of the optical pulse when leakage is near zero, while the peak power is proportional to the amplitude of the electrical pulse. So one can get the inverse relation between optical pulsewidth and the amplitude.

Comparing the three sets of curves (a), (b), and (c) in Figure 4.14, one can see an interesting phenomenon. When PW voltage is bigger than certain numbers, the pulse duration no longer rise with the PW voltage. In figure (a), optical pulsewidths keep the same values when PW voltage is bigger than 4V (amplitude 4 V) and 8V (amplitude 8V), respectively. However, in figure (b) those PW voltages are 4.8 V and 9.8 V, while in figure (c) only in amplitude 4V case, that PW voltage is 5.8V. Obviously, it's due to the specified pulse duration of the pulse generator. The biggest output electrical pulsewidths are around 3 ns. Figure 4.15 illustrated the linear relationship between the electrical and optical pulses. Also an inverse relation can be found between the slopes and the amplitudes.

Repetition frequency

It was found that repetition rate has no effect on the power and leakage, as expected. Choosing 1, 10, 100, and 1000 kHz repetition rate frequencies, we did the same experiment in which peak power and leakage of EOM's two output channels were recorded with 5ns optical

pulsewidth. The test results of peak power, leakage and extinction ratio versus bias were compared in Figure 4.16 and Figure 4.17. The differences are negligible.

Using higher repetition frequencies, we can save scan time and minimize the low frequency noise in the DBS system. However, repetition frequency is limited, because we should keep only one optical pulse passing through the sensing fiber at any time.

Stability of electrical pulse

To insure the EOM was driven by a stable trigger signal, the stability of output electrical pulsewidth and peak power from the AVTECH AVMP-2-EW pulse generator were checked in two simple tests. First, pulsewidth and peak power were monitored every 5 minutes in 21 minutes and then they were measured every 30 seconds for a duration of 12 minutes.

Test results were shown in Figure 4.18 and summarized in Table 4.5. Comparing Figure 4.18A and 4.18B, we can see both pulsewidth and peak power drift around a mean for every half minutes tests in 4.18B, while they show a slow raising tendency in both every half minutes and five minutes tests.

Table 4.5 Stability test result of electrical pulse.

Test in every 5 minutes			Test in every 0.5 minutes		
	Pulsewidth	Peak power		Pulsewidth	Peak power
Maximum	1.1852	8.4000	Maximum	1.1828	8.3800
Minimum	1.1664	8.3000	Minimum	1.1636	8.3000
Mean	1.1765	8.3433	Mean	1.1738	8.3296
Difference_{max}	0.0101	0.0567	Difference_{max}	0.0102	0.0504
Fluctuation	0.9%	0.5%	Fluctuation	0.4%	0.3%
Stand. Error	0.0033	0.0174	Stand. Error	0.0010	0.0048
99% Conf	0.0132	0.0704	99% Conf	0.0027	0.0134

Unit: Pulsewidth – ns; Peak power – mW.

Stability of optical pulse

The stability of optical pulses is very important for the distributed Brillouin sensing system, especially for small structure (i.e. the size of several meters) measurements. It is because of the peak power and the leakage hence the extinction ratio that impacts the system performance, while the pulsewidth sets the spatial resolution of the system. If the optical pulses are not stable, poor performance of the system will be found in strain/temperature measurements. For this reason, an optical pulse coming from EOM's output pigtail A was measured one thousand times in twelve hours. The initial peak power, leakage and pulsewidth were 59mW, 31mW, and 2.00ns, respectively. Bias was set on 8.6V, while PW voltage was 8V. Probability distributions of peak power, leakage and pulsewidth show in Figure 4.19 and Figure 4.20 and summarized in Table 4.6.

Table 4.6 Stability of one thousand times test result of an optical pulse.

	Peak Power (mW)	Leakage (mW)	Pulsewidth (ns)
Mean	57.2976	32.5509	2.0275
Maximum	69.2	40.4	2.4
Minimum	45.2	25.6	1.8
Difference_{max}	12.1	7.8	0.37
Fluctuation	6.9%	7.8%	2.6%
Stand. Error	0.1242	0.0808	0.0016
99% Conf	0.3206	0.2085	0.0042

We see that average values are very close to initial numbers. For twelve hours of measurement, the fluctuations are ±6.9 % for peak power, ±7.8% for leakage, and ±2.6% for pulsewidth, respectively. The result of stability measurement reminds us that the random errors cannot be neglected. Setting a suitable average number for DBS system is a good method for improving the test accuracy. For our Brillouin sensing system, an average number of 2000 means that a time domain waveform downloaded at each frequency step is the mean of 2000 real-time waveforms. The bigger the average number, the higher the measurement

accuracy. However, it will take a longer measurement time. We need to have a feedback system for the pulsewidth and power of the optical pulse in order to get high strain measurement accuracy. Following we will examine the impacts of pulsewidth, power, and bias to accuracy of strain and temperature measurements. Since the power supply drifted during the test, bias and PW voltage were adjusted several times during the experiment.

4.3 Repeatability of DBS system

4.3.1 Influence of the bias

In the previous section we have measured the drift of power, pulsewidth, and bias of the modulator vs. time. In this section we will study the impacts of those drifts on Brillouin scattering based distributed sensing system. In order to study the effect, we designed a strain unit as shown in Figure 4.21.

The experimental setup consisted of a 1.6m long steel bracket, 36 small pulleys, and a piece of PVC buffered single mode fiber. Twenty pulleys were fixed on the steel bracket and suspended from the ceiling with the fiber hanging down in 19 loops. Point glued with high strength epoxy on the top of 20 fixed pulleys; the piece of optical sensing fiber was separated into 19 regions. Every region between two neighboring pulleys were named with a letter, such as, the loop "B" is a piece of 200cm long sensing fiber located between pulley 1 and pulley 2. Unnamed three pieces between pulley5&6, pulley10&11, and pulley15&16 were one-meter long loose fibers. The lengths of named fiber loops are shown in Table 4.7.

The fiber would be stretched uniformly in a loop when a weight was hanging on the free pulley (the diameter is 25 mm) that was at the bottom of the same loop. The purpose of this experiment is to see with those drifts the shortest strain length that the distributed sensor system can detect. Hence we put 10 cm, 15 cm, and 20 cm section. The 30 cm section was designed for the purpose of detecting the strain accuracy for the uniform strain.

Table 4.7 Sensing fiber lengths in different regions

Fiber Name	Length (cm)
B, C	200
D, E	100
F, G	50
H, I	40
J, K	30
L, M	20
N, O	15
P, Q	10

Positive and negative bias

When UO's DBS system starts a measurement, the lasers were turned on for 30 minutes to one hour to reach a stable operating temperature, then the initial states of the pulse generation and laser control subsystems were set. The status of the data acquisition system was checked and then the measurement procedure began [DeMerchant 2000].

After the computer control turned on the lasers, NT control software would automatically set pulse duration and EOM bias that could be either a positive or a negative number between ±10V. It was found that the EOM bias would be at different values for Single Acquisition mode. In Continuous Acquisition mode, when setting the bias at one specific value, it is observed that the values would rise up slowly during the measurement. If the feedback control is not on, those phenomena partly come from current configuration in which leakage instead of bias was set for locking on the initial number, however electrical pulse would be rising continuously as shown in Figure 4.18.

Figure 4.22 shows the comparison of the no load test results for different bias values with the experimental setup (Figure 4.21). These are four single acquisition runs with 1.8ns pulse duration and average number of eight thousand. Two tests were done for leakage setting at

0.01V. The other two recorded at 0.04V leakage. The computer software chose biases automatically. As previously presented, the peak power and leakage of the output optical pulses of the EOM changes periodically and the periodicity is around 10 volts. In both figure A and B, the sum of the two absolute values of two biases is close to the bias working period of EOM. So we thought they should have similar effects. However, the difference was seen obviously. The biggest Brillouin shift difference between two curves is 2.3MHz for figure A and 3.7MHz for figure B equivalent to 40.1με and 64.5με strain or 1.9°C and 3.1°C temperature differences. The possible reason is that different biases correspond to different peak power, pulsewidth, and SNR of the probe pulses, which cause different signal resolutions and spatial resolutions harmonizing to different experimental results.

Different leakages

Results with near biases, but different setting leakages are compared in Figure 4.23. Figure A is for negative bias and figure B is for positive bias. The biggest Brillouin shift difference between two curves is 3.2MHz for figure A and 2.1MHz for figure B equivalent to 55.7με and 35.0με strain or 2.6°C and 1.6°C temperature differences.

Comparing part A and part B in Figure 4.23, smaller difference was received with negative bias than that of positive bias. From Figure 4.22, better performances were found with smaller leakage. It is because smaller leakage is equivalent to larger SNR that results in good performance of the system. The results in this section illustrates that using different bias would lead to different test results and therefore the bias fluctuation is one of the most important error source.

4.3.2 Polarization states and averages

For UO's DBS system, in order to increase SNR and reduce polarization effects on the measurement, a number of time domain waveforms are averaged before the pump depletion is measured [DeMerchant 2000]. Large average numbers will increase strain and temperature

measurement accuracy at the expense of longer measurement time. Normally this number is set from 500 to 2000 depending on spatial resolution. Smaller spatial resolutions require a larger number averaging to reach the same accuracy.

During the project we found the system performance was poor with normal 2000 averages in smaller spatial resolution as shown in Figure 4.24(B). LeCroy LSA 1000 Signalyst of UO's DBS system allows up to 2000 waveforms to be averaged with as little as 25 μs dead time between "segments" [Brown 2000]. However, the polarization controller (HP11896A) has a 12 second paddle adjustment time to finish polarization state scrambling. If the frequency scanning range of a measurement run is from 12650MHz to 13100MHz with a 5MHz step, it will normally take about 240s. Each step is going to take about 2.7s including data acquisition, transmission, and system preparation time, that is the polarization controller has scanned only 2.7/12 part of the polarization states on Poincaré Sphere. This cannot reduce the polarization sensitivity of the sensor system. To improve the impact of the polarization state variations on the system performance, we need to use a high-speed polarization scrambler. Alternatively, we can also increase the waveform-averaging time to about twelve seconds to match the current polarization scrambler (HP11896A). 8000 averages instead of 2000 are required. As a result, the test time of a single run has been increased by four times. Figure 4.24(A) shows the result of 8000 averages. A piece of loose fiber was measured ten times for both 8000 averages (A) and 2000 averages (B). Test results summarized in Table 4.8.

Table 4.8 Comparison of ten measurements of a loose fiber for both average 8000 and average 2000.

	Average 8000	Average 2000
$\text{Deviation}_{ave.}$	0.3394 MHz	1.7352 MHz
Deviation_{max}	0.4426 MHz	7.4640 MHz
$\text{Deveation}_{min.}$	0.2839 MHz	0.3594 MHz
Δv_{max}	5.5 MHz	13.62 MHz
Bias drift	0.85V	0.81V
Test time for single run	12'53''	3'46''

Both experiments in Figure 4.24 took distributed measurement every 30 minutes within five hours. In 8000 averages case (A), the bias drifted 0.85 V (from –5.37V to -6.22V) during the five hours of measurements. For 2000 averages, the bias changed 0.81V (from - 4.73 V to -5.54V) in ten runs. Comparing Figure 4.24 A and 4.23, similar curve shape can be found if using same scales in axes with the figures. Although a long measuring time (12'53'') in the 8000 averages case should induce bigger bias drifting and leakage variations in each run than that of 2000 averages, ten measurements are having agreeable results in Figure 4.24 A. It is demonstrated that 8000 averages did improve the performance of the DBS system.

4.3.3 One or two laser frequency lock

In UO's DBS system, one of most important acquisition parameters is Brillouin frequency ν_B that is a frequency difference between probe and pump lasers and from which one can calculate strain and temperature. During the measurement, locking ν_B in stable values at each step within the frequency-scanning region is the foundation of the distributed strain and temperature measurement of DBS system. Fluctuation of the ν_B will cause errors in both strain and temperature measurements.

There are two methods to lock the Brillouin frequency. The first is holding one laser's frequency and adjusting the other one to the desired frequency differences. We named this method as one-laser lock (I). The second method, two-laser lock (II), is adjusting two lasers in both positive and negative directions simultaneously. Compared to the one-laser lock method, the two-laser lock can lock the set frequency differences quickly, since it can approach the ν_B from two directions. In this project we compared the performances of these two methods.

The experimental setup used for the comparison of one and two laser lock methods is shown in Figure 4.21: two 200g weights were hung at the bottom of pulley B and D respectively, while a 500g weight hung at F. Three chosen leakages were 0V, 0.015V, and 0.025V. The measurements are shown in Figure 4.25. Compared to the real strain distribution in Figure 4.25 (R), both (I) and (II) methods got correct strains that were proportional to the weights and right sensing fiber sections. They are 2m, 1m, and 0.5m, which were under

uniform strains. Two-laser lock method (II) was more sensitive to different leakages but failed to distinguish the sensing fiber section F at 0.015V leakage case. Actually, according to statistic results in twenty measurements, the possibility with which the method (I) cannot differentiate the section F is 33%, while that possibility of the method (II) is 14.3%. Method (I) needs more time to lock a projected frequency; sometimes it failed and caused "socket error" for the DBS system. However it can get more repeatable sensing fiber locations for different leakages. Method (II) can lock a frequency more quickly, but it is poor to locate the sensing fiber with different leakages. The experimental results of method (II) also illustrated that choosing correct bias (or leakage) is very important for DBS systems.

To explain the above phenomena, it is important to review how the laser frequency is tuned. There are two methods for tuning the frequency of the Nd: YAG laser used in our DBS system: heating of the laser crystal and inducing strain in the crystal with a piezo element [LIGHTWAVE 1997]. The temperature of the laser crystal can be varied by applying a voltage to a thermoelectric cooler (TEC) under the laser crystal. Heating the crystal will result in the physical expansion of the crystal and increasing the refractive index of the Nd: YAG. Both of these techniques will lead to a physically longer cavity length that slightly decreases the output frequency of the laser with a tuning range over tens of gigahertz in 1 to 10 seconds. For the second method, the single-frequency output of the laser can be quickly tuned over several megahertz by applying a voltage to an optional piezoelectric element bonded onto the crystal that contracts or expands the laser crystal. It strains the crystal sufficiently to vary the frequency by tens of MHz at rates up to 0.1 MHz. The tuning coefficient is specified to be >1 MHz/volt.

Obviously, any variation of the environmental temperature or the fluctuation of the tuning voltages will cause the changing of the tuning frequency. In method (I), since one laser adjusts the frequency difference, longer times to adjust and stabilize the set frequency are needed than for method (II). If the software cannot lock a set frequency in the time predetermined, the failed lock operation is recognized by the computer. Because the frequency of one laser is fixed, method (I) has advantage to locate the sensing section of the fiber. On the other hand, method (II) tunes the frequencies of two lasers to close in on set frequency difference, but independent of the real frequency values for both lasers. It saves

tuning time, but has a drawback on determining the position of the fiber, as the frequencies of two lasers are unsteady.

4.4 Summary

There are about 35 different adjustable settings that can be used to configure the control software for a specific sensing application and would directly impact the performance of DBS system. In this chapter we studied several of them around the pulse generation subsystem, such as, bias, leakage, PW voltage, pulsewidth, and repetition frequency. Bias is found to be the most important. This is why we developed a bias control feedback system. In the future a quantification of this influence will be evaluated after rewriting some parts of the software. We also discussed the relationships among the repeatability of DBS system and some parameters of the equipment; those include bias, polarization controller, averages and frequency lock methods.

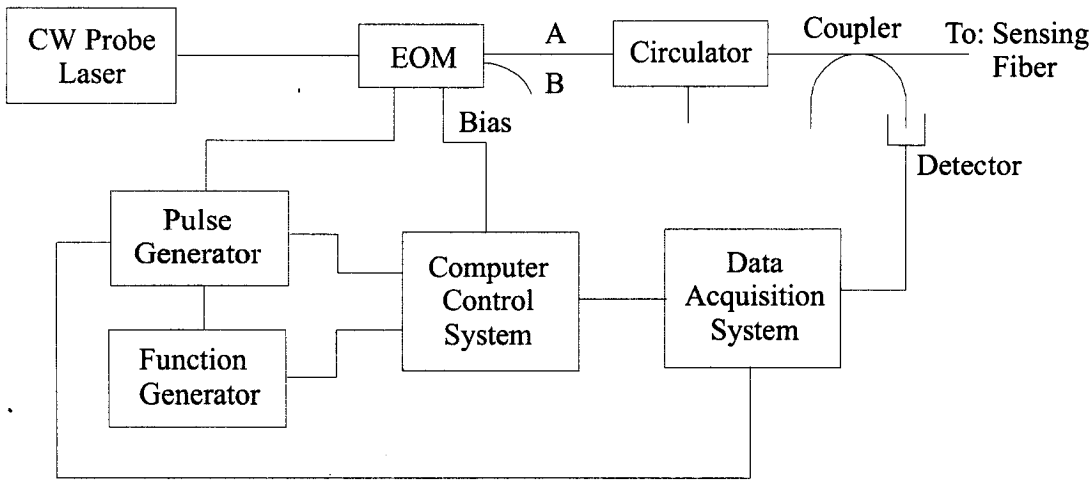

Figure 4.1 Configuration of the pulse generation subsystem

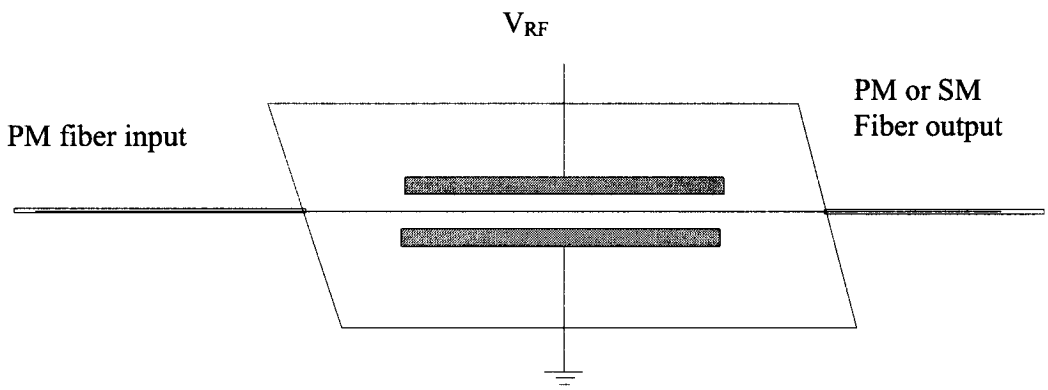

Figure 4.2 Configuration of the integrated phase modulator

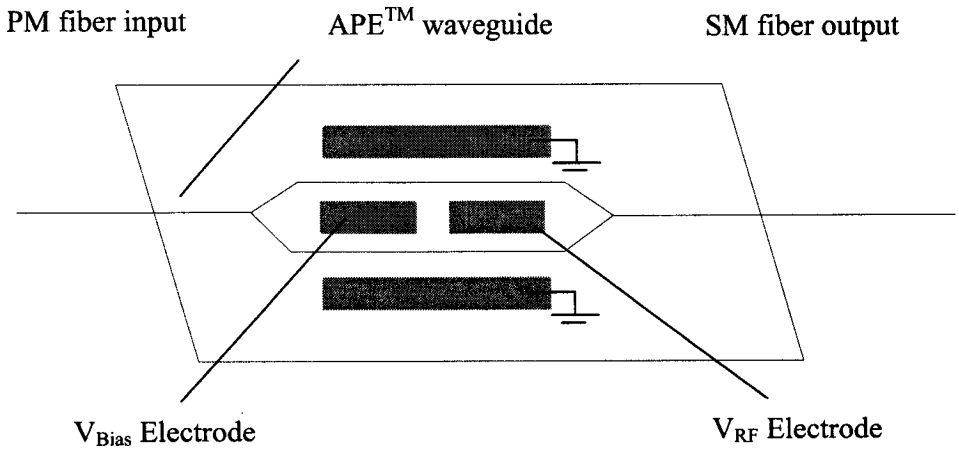

Figure 4.3 Single Output Mach-Zehnder amplitude modulator

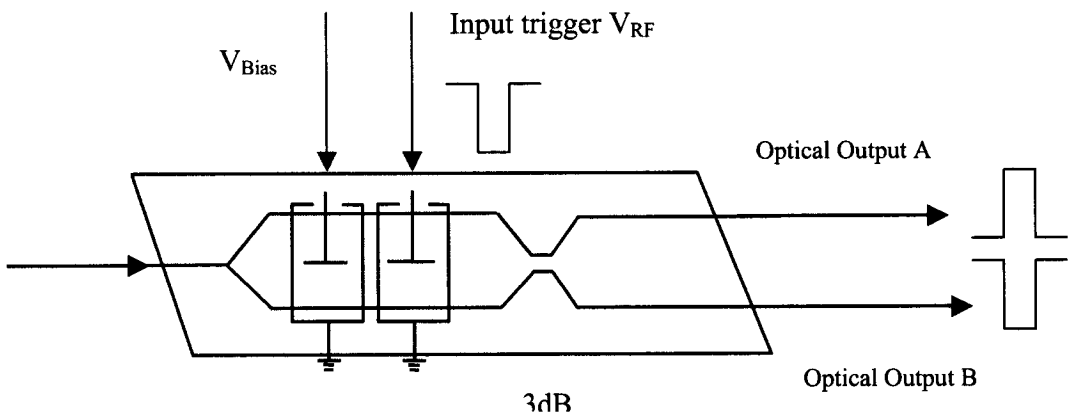

Figure 4.4 Configuration and action of a Y-balanced bridge electro-optic modulator used in UO's DBS system

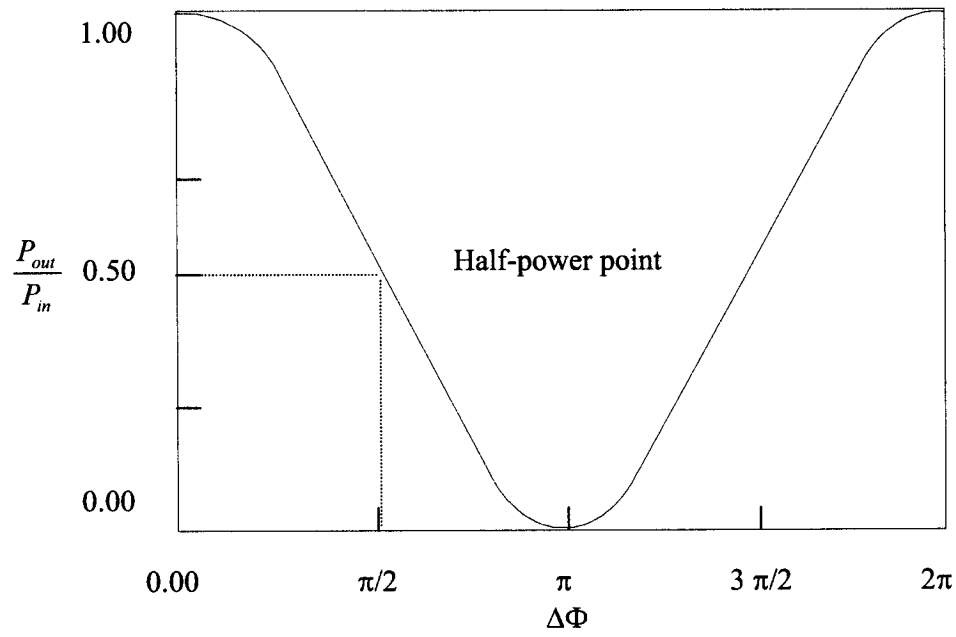

Figure 4.5 Transfer function of the amplitude modulators

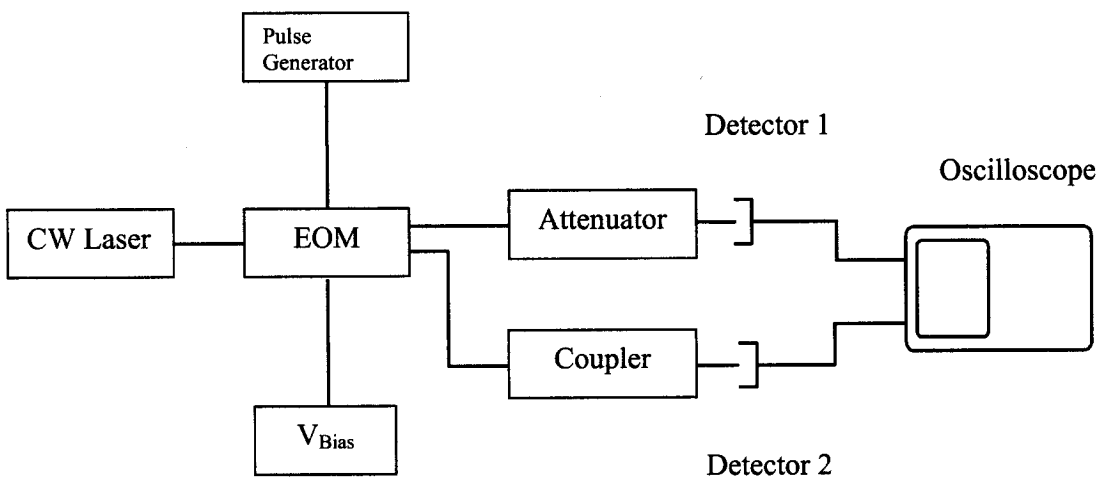

Figure 4.6 Experimental apparatus for study Y Balanced Bridge Modulator

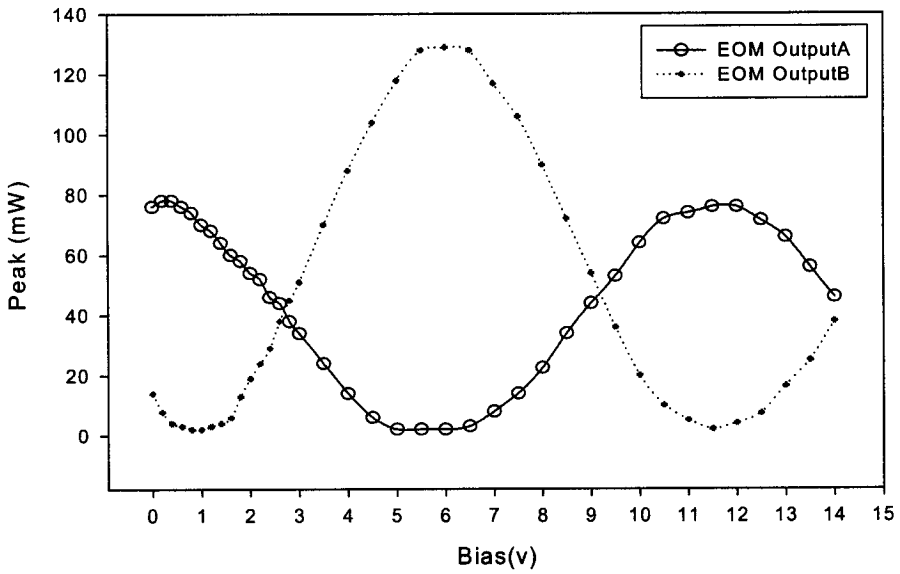

Figure 4.7 The relationship between the peak power of EOM's two outputs and the bias

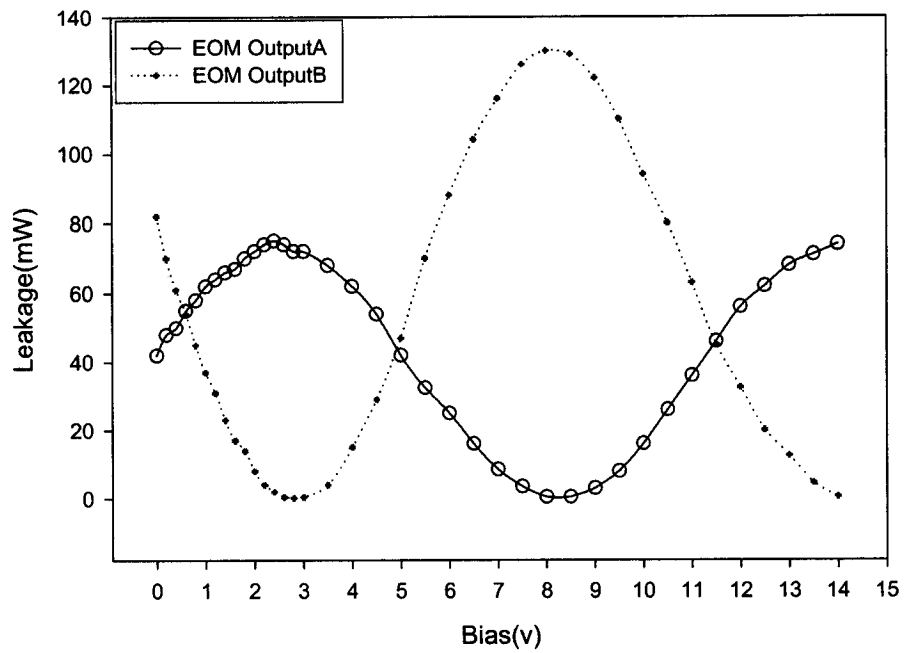

Figure 4.8 The relationship between the leakage of EOM's two outputs and the bias

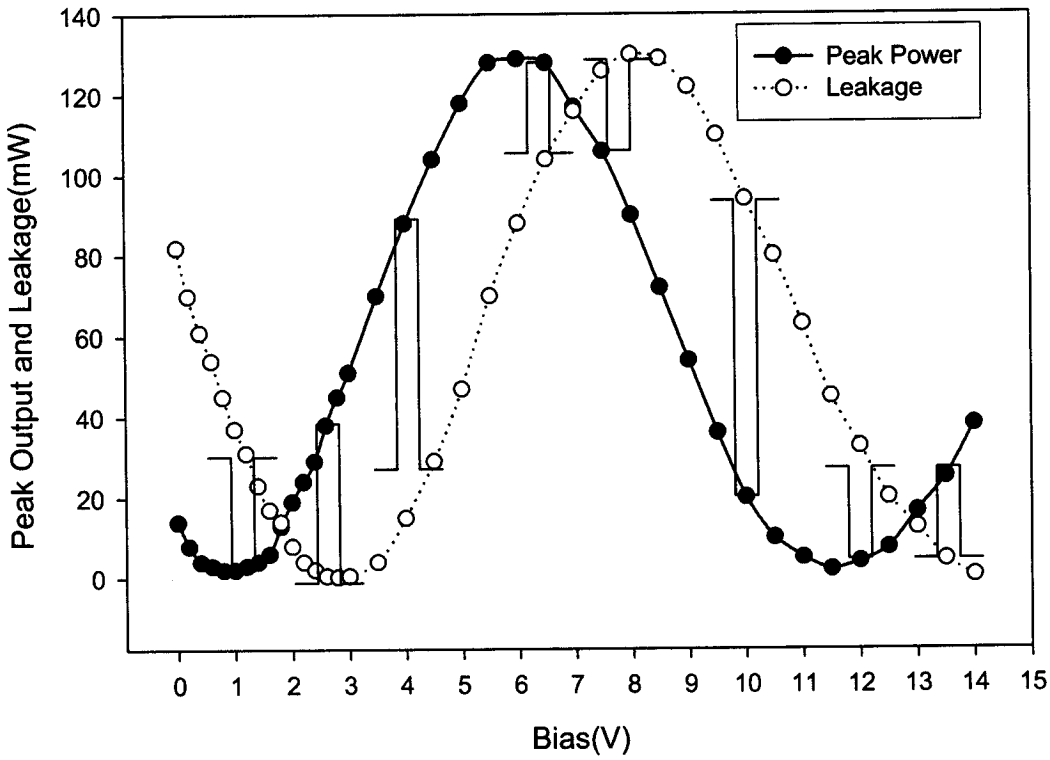

Figure 4.9 Peak output, leakage, and amplitude of optical pulse for EOM's output channel B

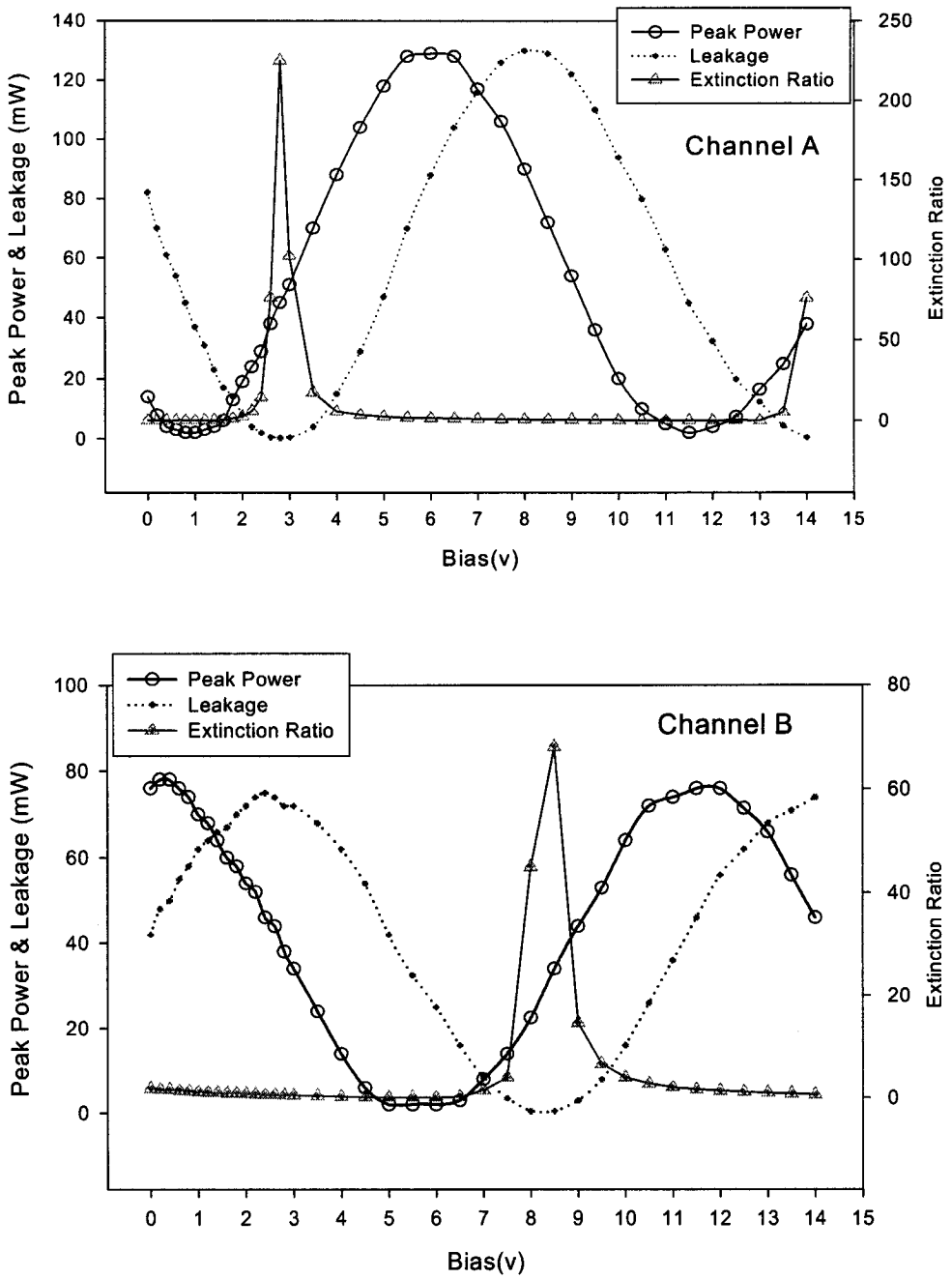

Figure 4.10 Peak power, leakage and extinction ratio for channel A and B in 1ns pulsewidth case

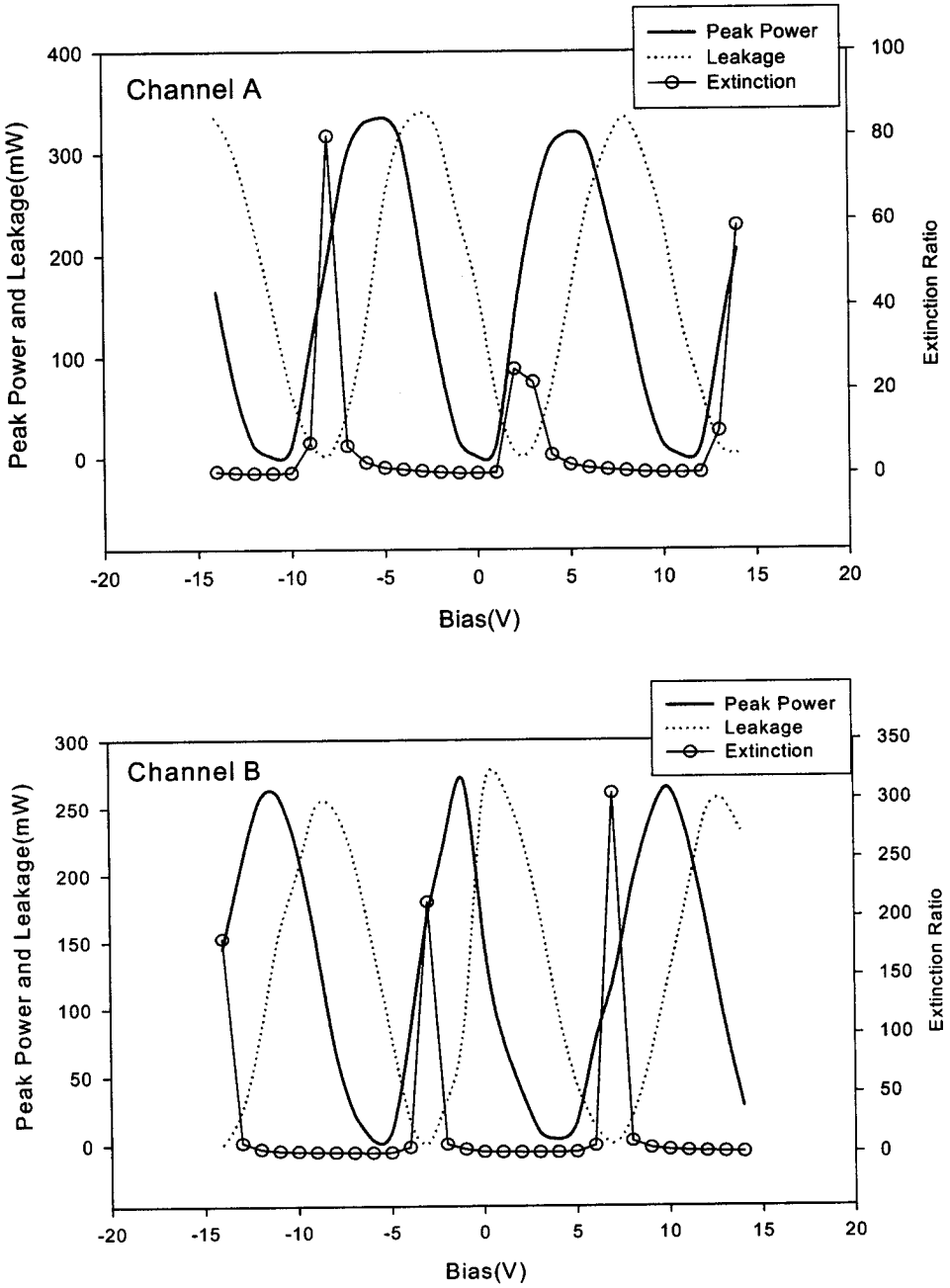

Figure 4.11 Peak power, leakage and extinction ratio for EOM's output channel A and B in 5ns pulsewidth case.

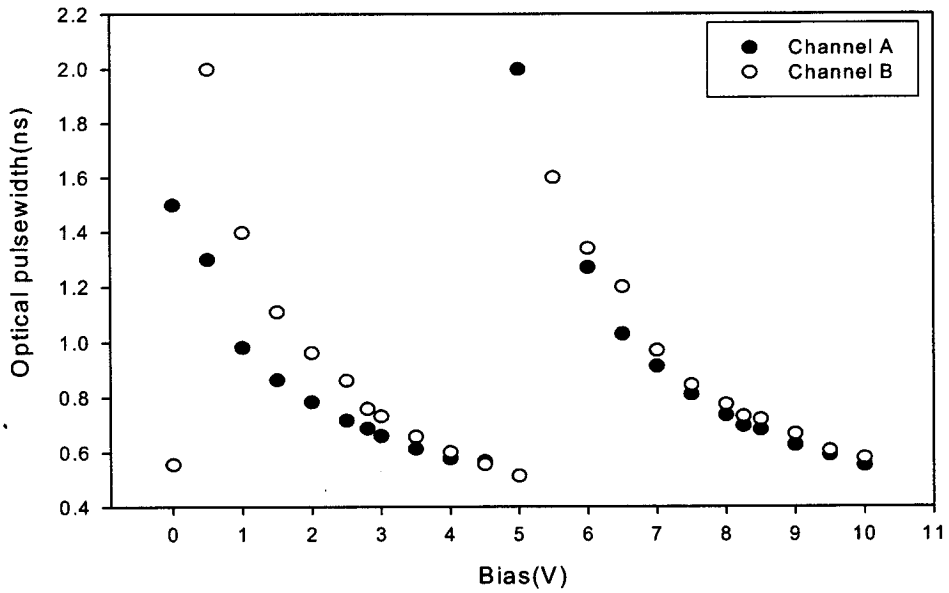

Figure 4.12 Relationship between optical pulsewidth and bias at 1 ns electrical pulsewidth

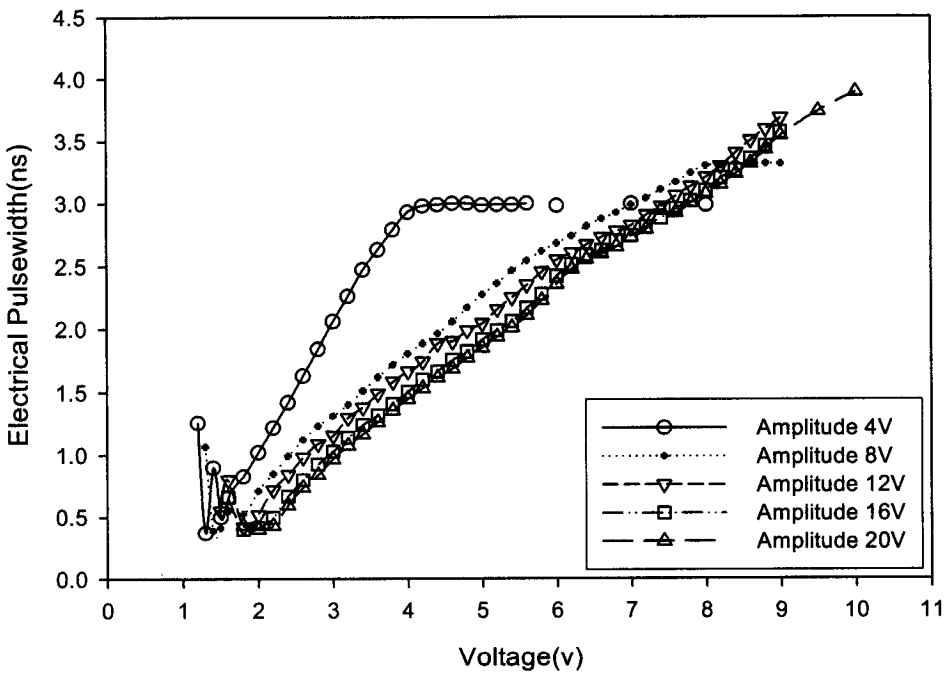

Figure 4.13 The relationship between electric pulsewidth and the PW voltages of the pulse generator.

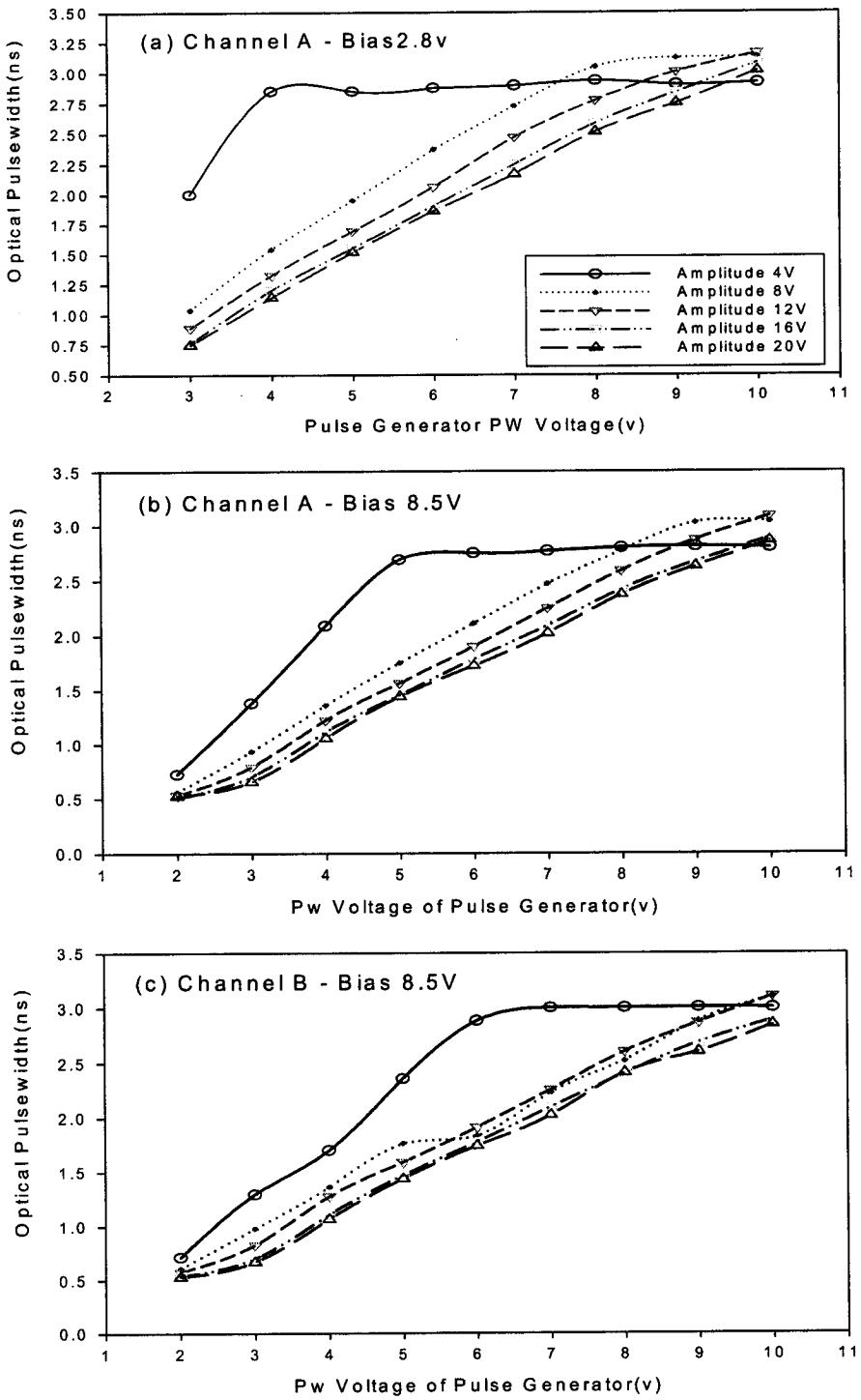

Figure 4.14 Relationship of the optical pulsewidth and the PW voltages of the pulse generator.

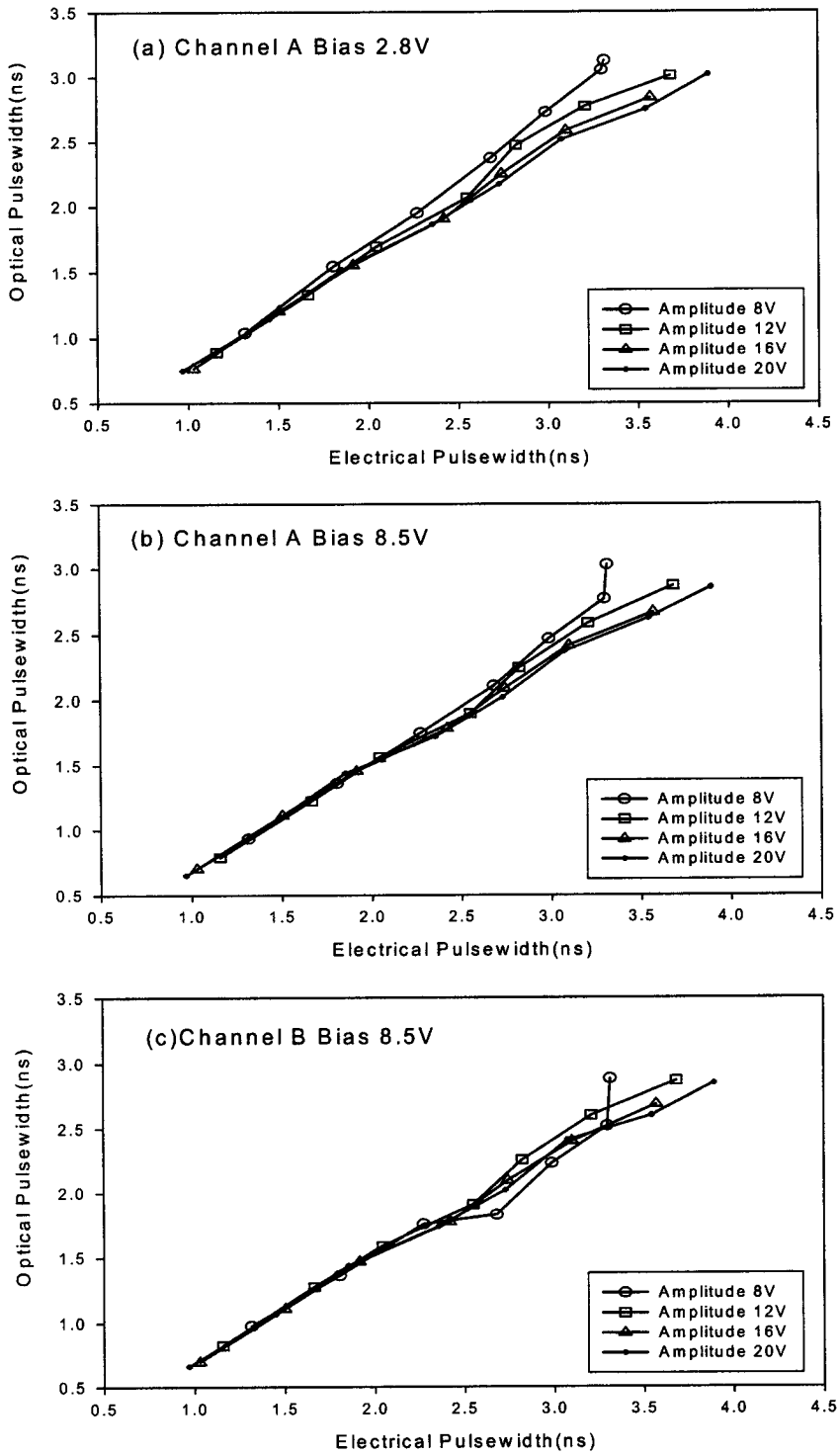

Figure 4.15 Relation of electrical and optical pulses for different Amplitudes

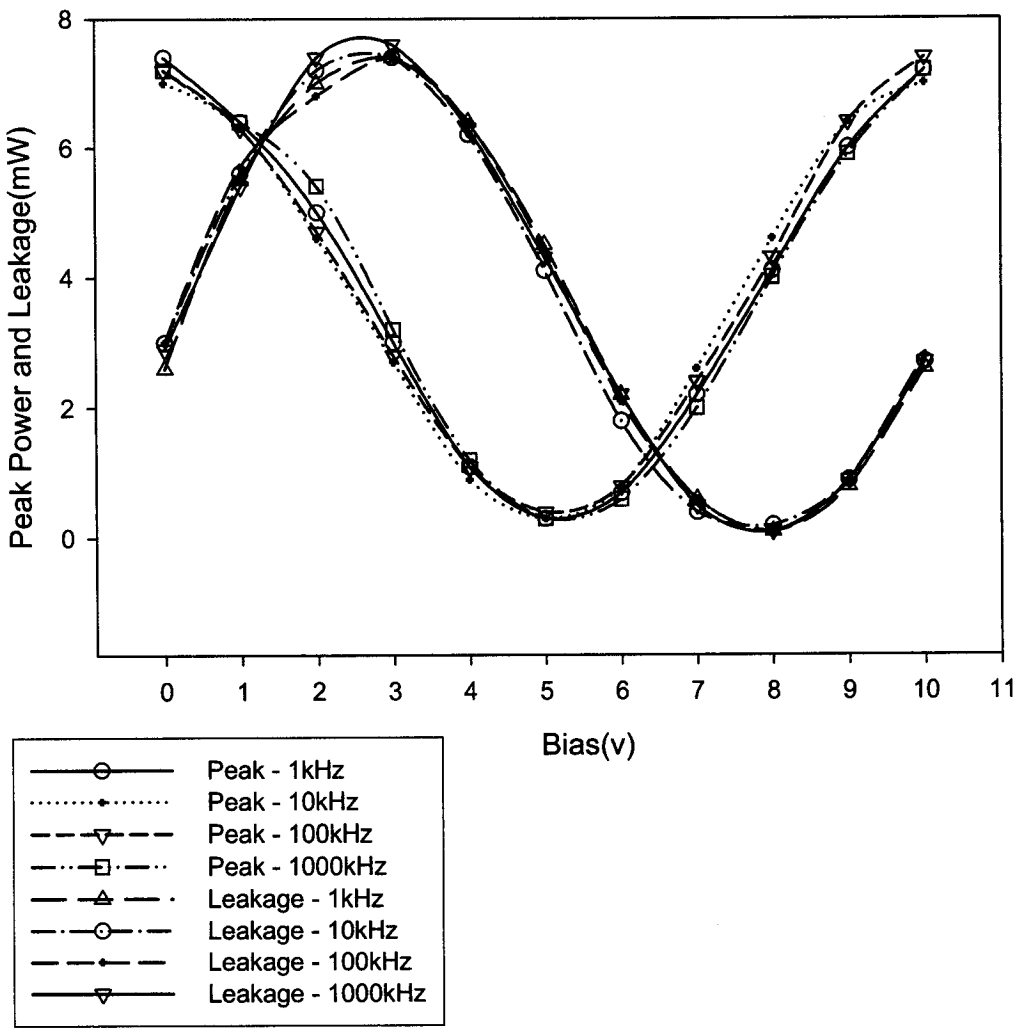

Figure 4.16 Comparison of peak powers and leakages tested in EOM's output pigtail A with different repetition frequencies at 5ns optical pulsewidth.

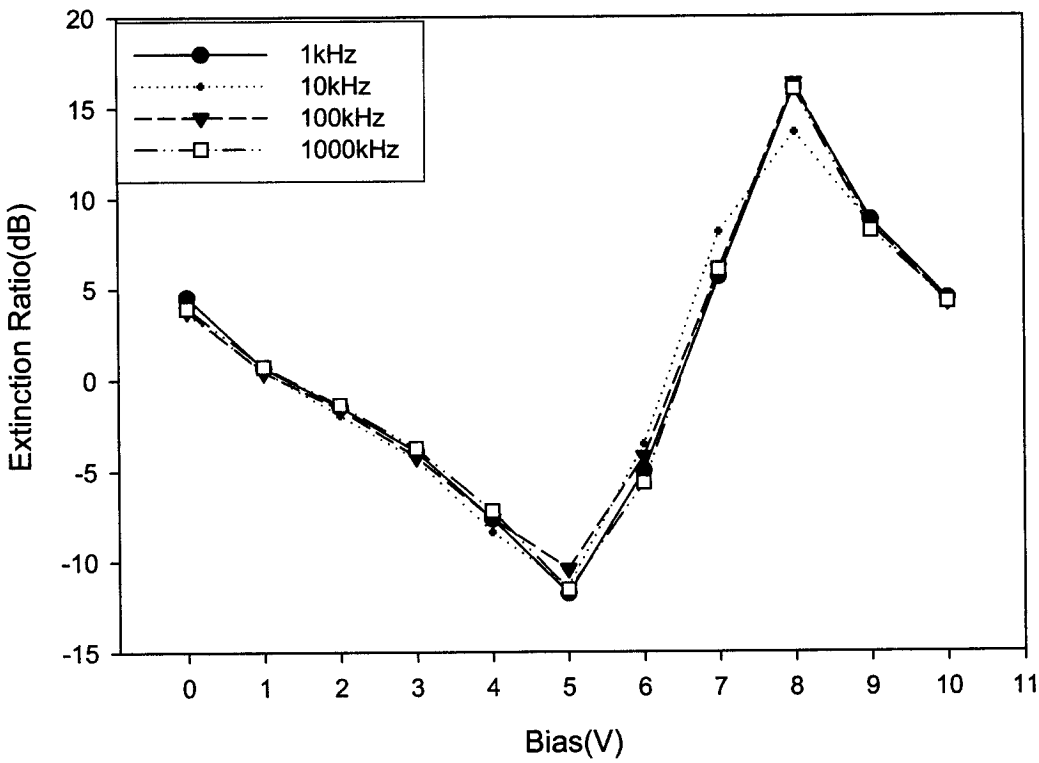

Figure 4.17 Comparison of extinction ratios (dB) tested from EOM's output pigtail A with different repetition frequency at 5ns optical pulsewidth.

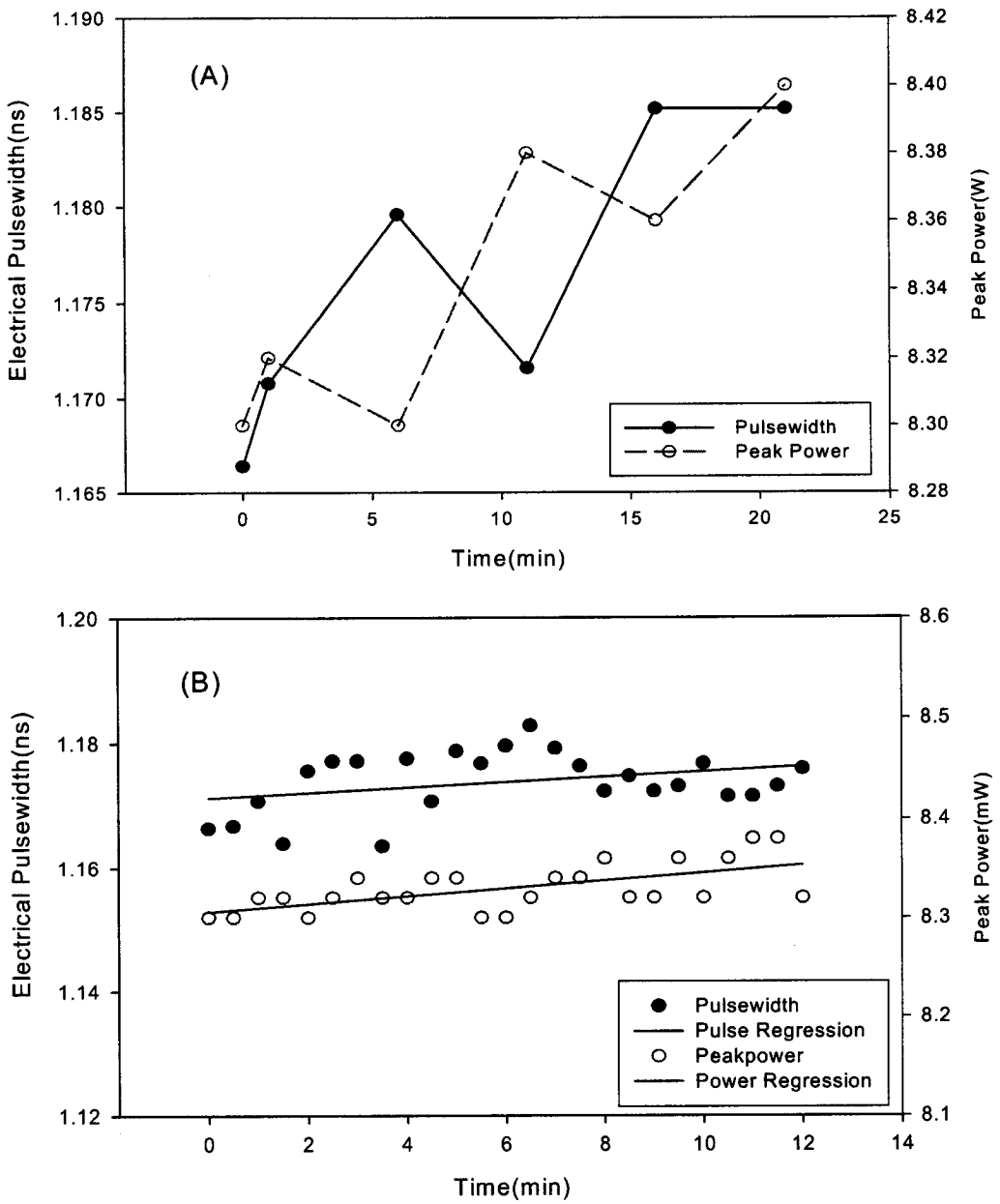

Figure 4.18 Stability of electrical pulsewidth and peak power for AVTECH AVMP-2-EW pulse generator, (A) measured every 5 minutes in 21minutes; (B) measured every 0.5 minutes in 12 minutes.

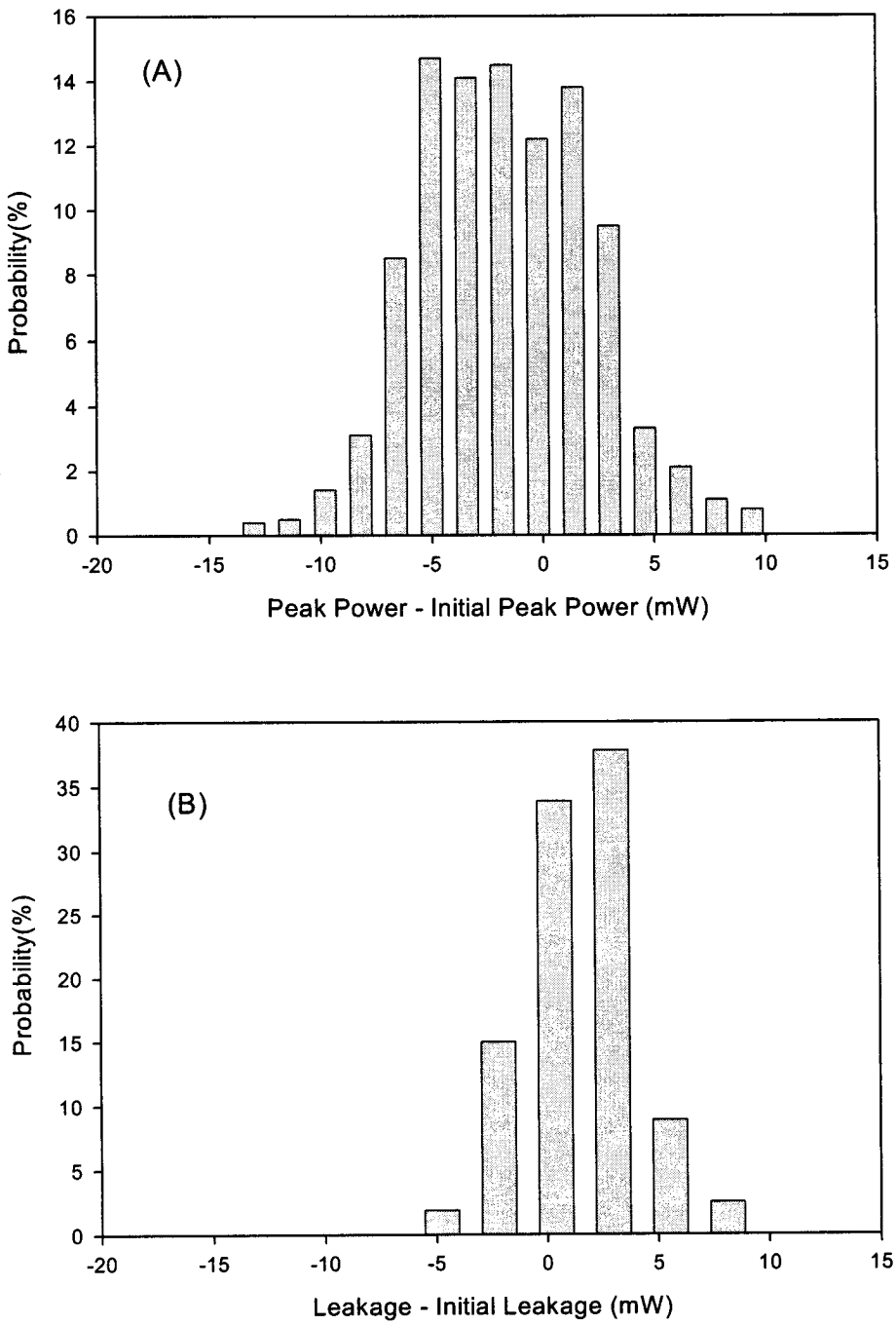

Figure 4.19 Distribution of (A) peak power and (B) leakage of an optical pulse measured one thousand times in twelve hours. The initial values of peak power and leakage are 59 mW and 31 mW, respectively.

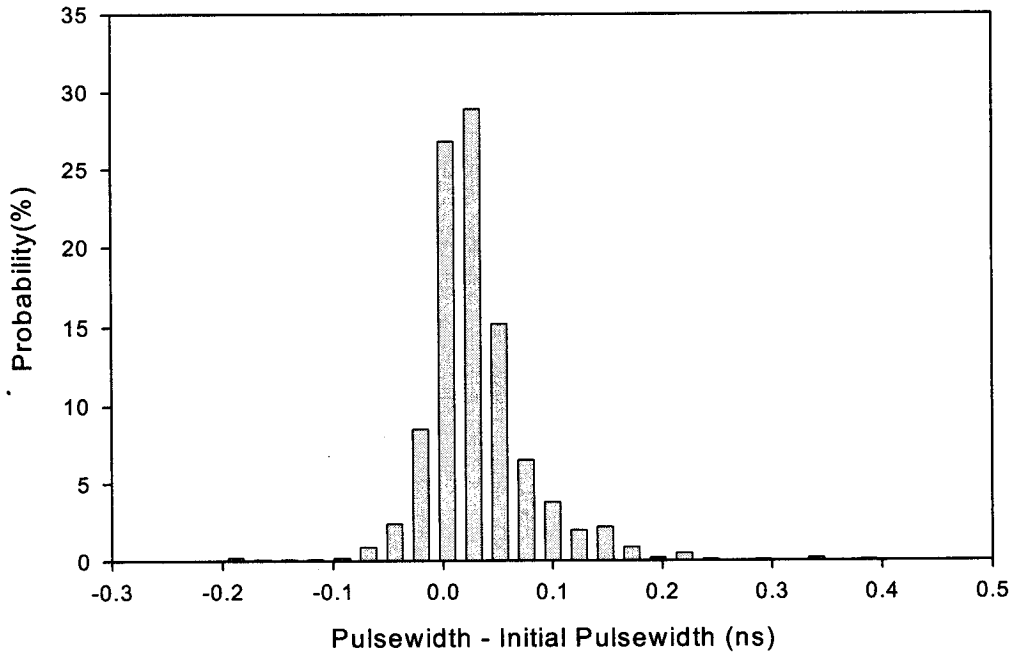

Figure 4.20 Pulsewidth distribution of an optical pulse measured one thousand times in twelve hours. The initial pulsewidth is 2 ns.

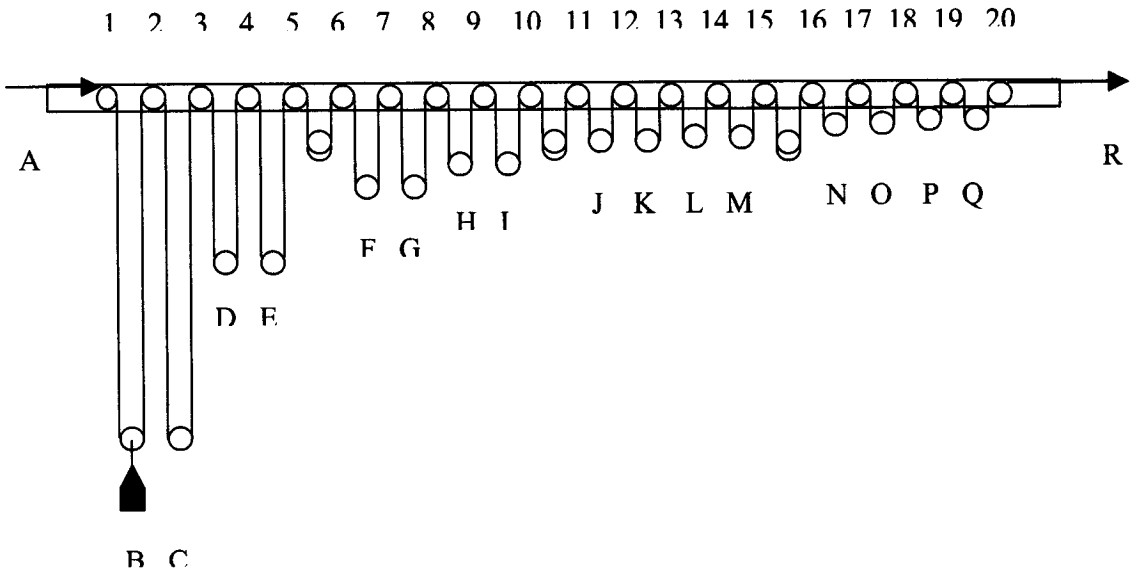

Figure 4.21 Experimental setup for testing the repeatability of DBS system.

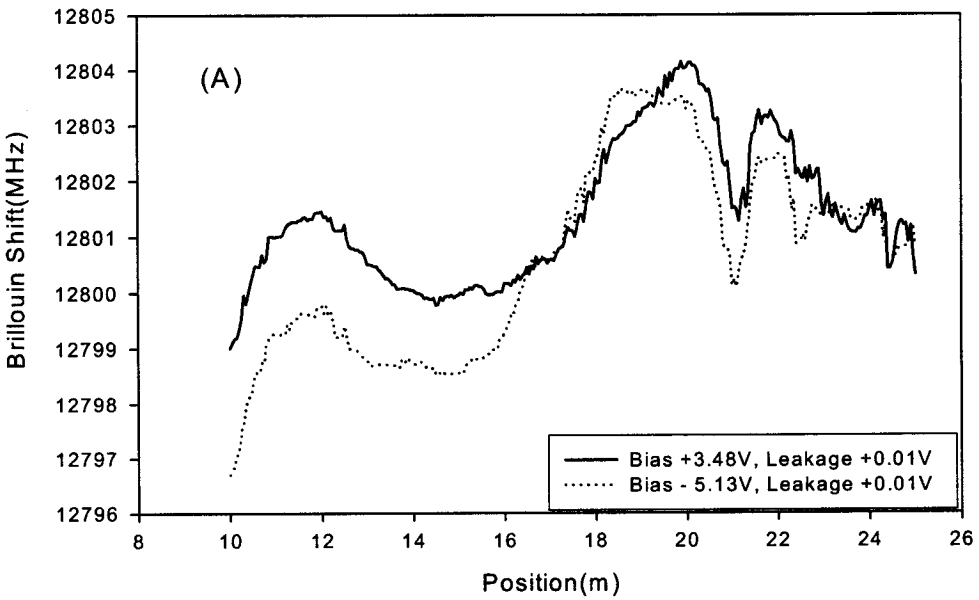

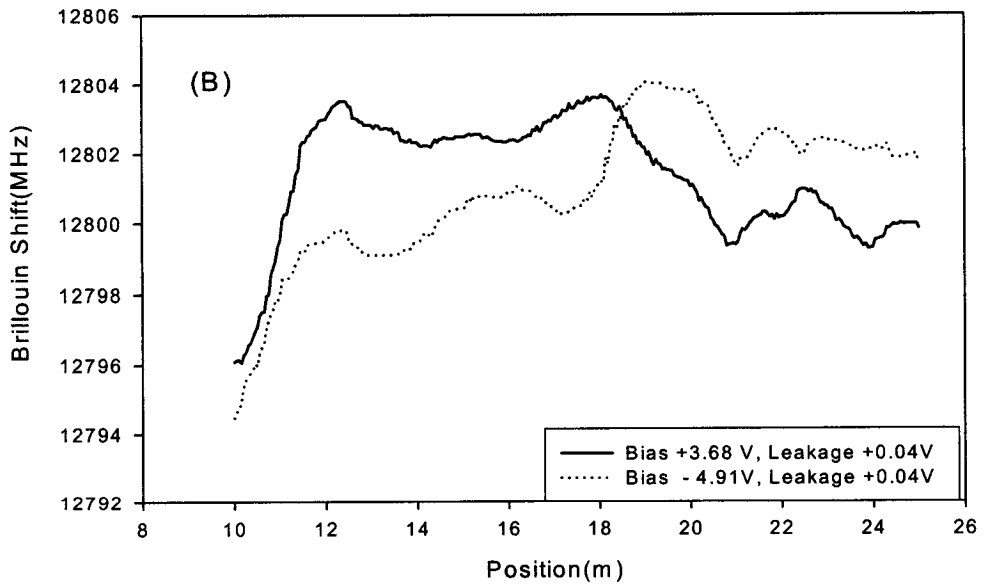

Figure 4.22 Comparison of test results with positive and negative bias in a loose fiber measurement. (A) Set leakage at 0.01V; (B) set leakage at 0.04V

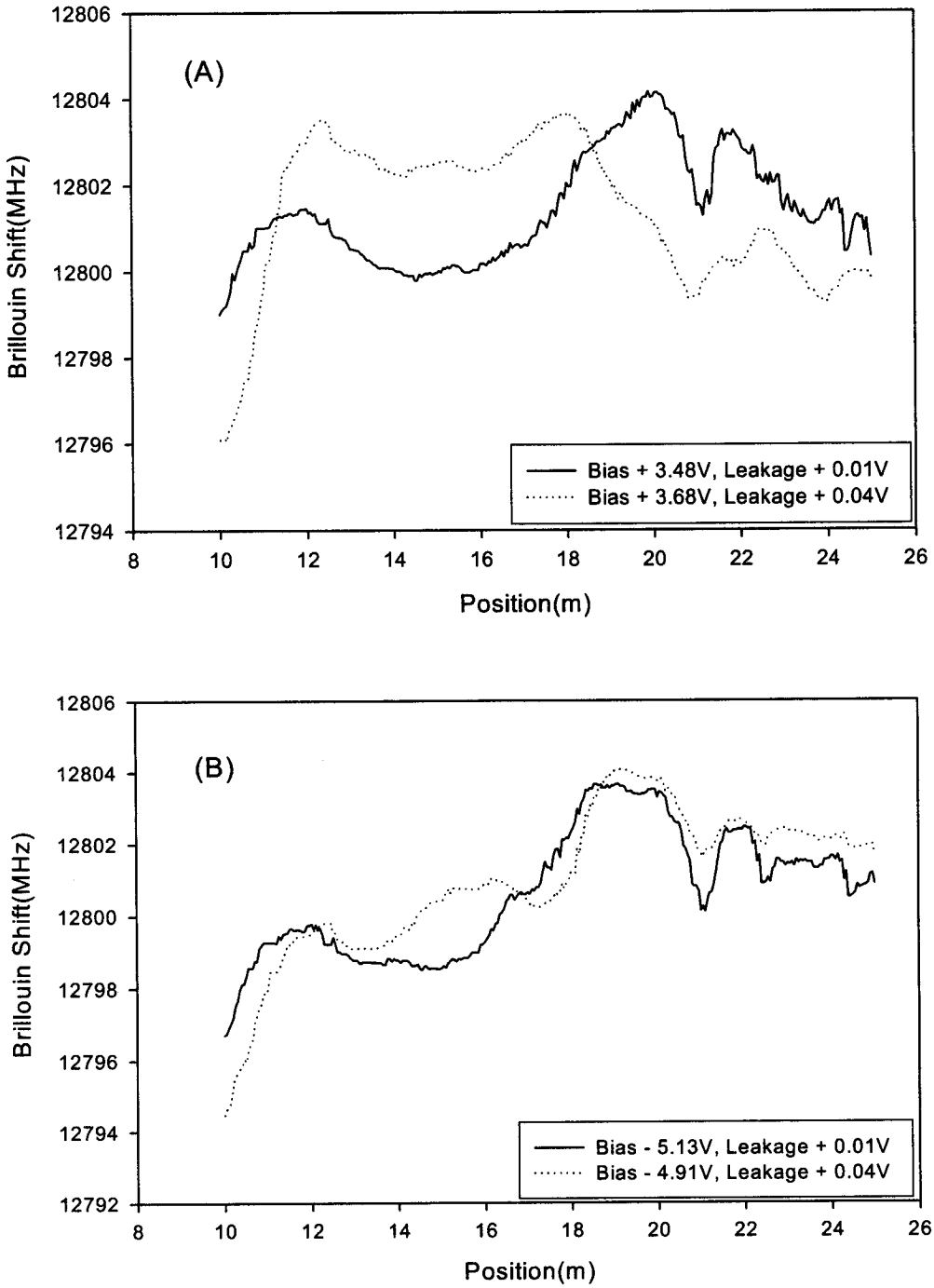

Figure 4.23 Comparison of test results with near bias, but different leakages in no load case.

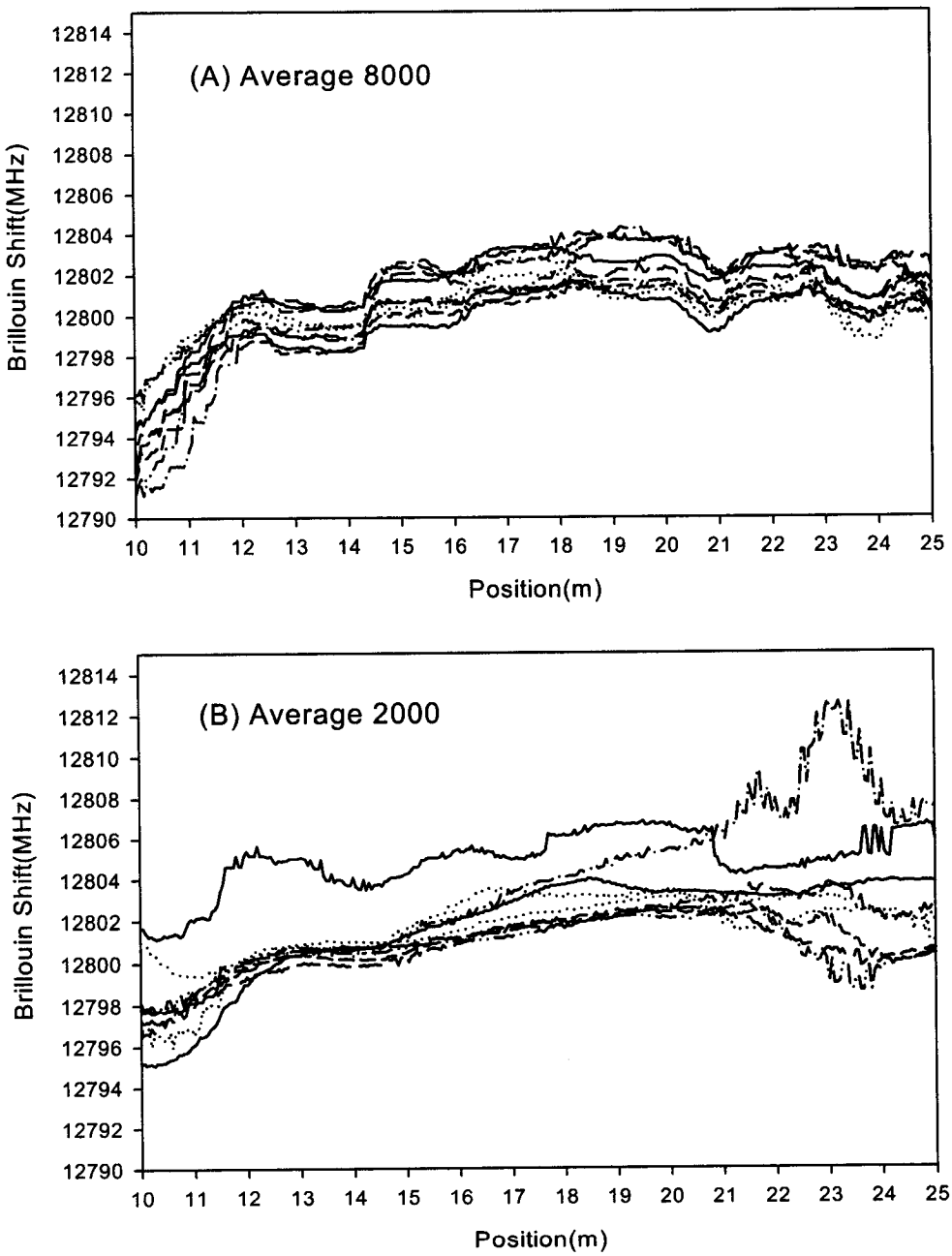

Figure 4.24 Comparison of 10 measurements no load tests with the experimental setup shown in Figure 4.21, (A) average 8000 and (B) average 2000.

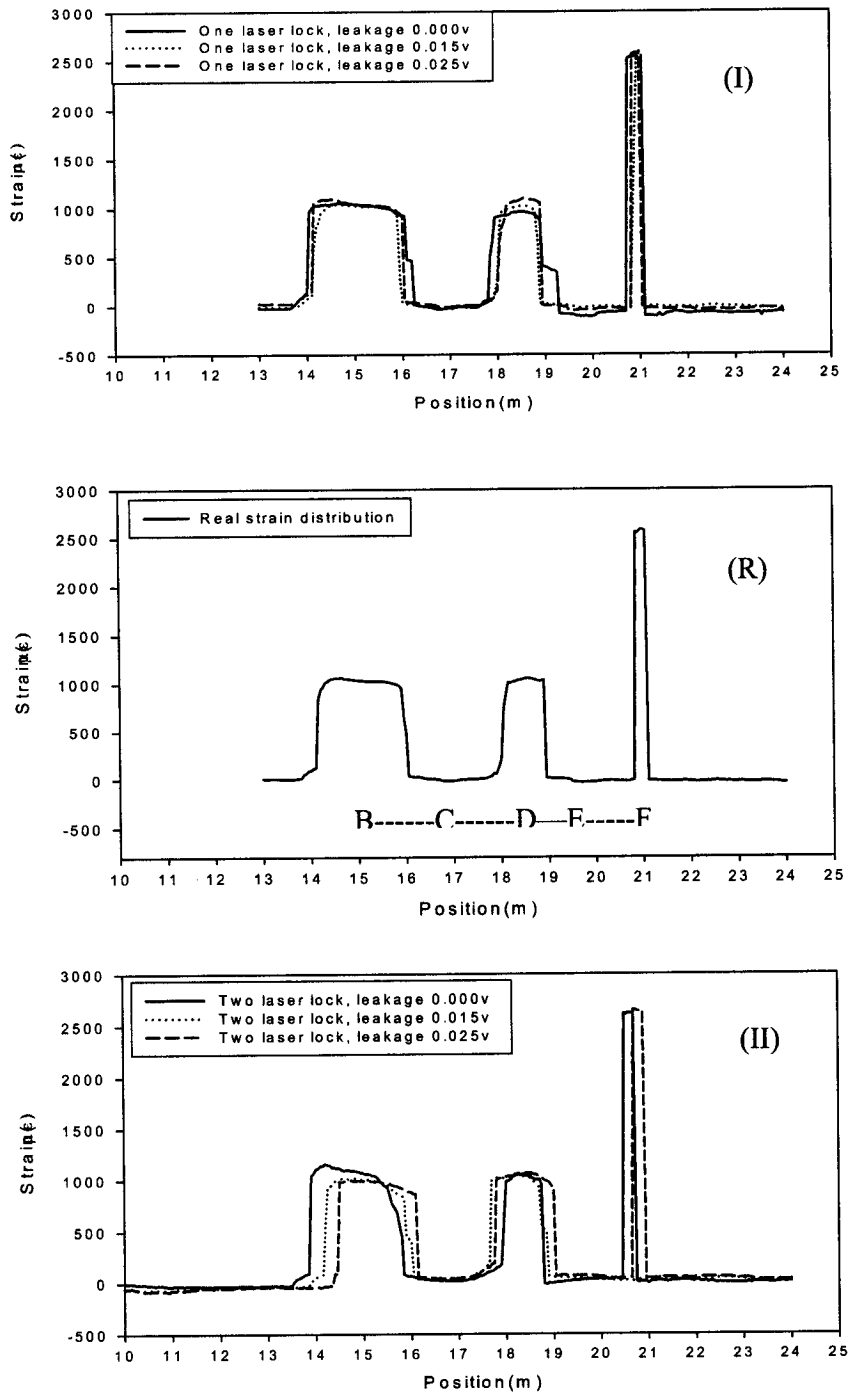

Figure 4.25 Load test with the experimental setup as shown in Figure 4.22. Hung 200g weights at B and D, 500g weights at F. (I) one laser lock, (R) real strain distribution, and (II) two-laser lock.

Chapter 5

Strain Measurement in a Concrete Beam

Application of the distributed Brillouin sensing in scientific research and industries is our ultimate goal for developing this technique. This section presents the strain measurement of a 1.65 m reinforced concrete beam using a Brillouin scattering based distributed fiber strain sensor with a 50 cm spatial resolution [Zeng et al.2002]. The strain distribution was measured for one-point and two-point loading patterns for optical fibers embedded in pultruded glass fiber reinforced polymer (GFRP) rods and those bonded to steel reinforcing bars.

5.1 Introduction

The distributed fiber optic sensing system based on Brillouin scattering (as shown in Figure 3.1) developed by our Fiber Optics Group has been used to monitor the strain in plastic pipes [DeMerchant et al. 1998a] and steel beams [Bao et al. 2001].

In this study, the optical fiber was embedded in a concrete beam to measure its internal strain and to allow measurement of both structural and material strains. The difficulties associated with strain measurement in concrete are: First, the concrete could generate cracks under heavy loads (~4.445kN or 1000 lbs that weight is spread out on 10cm ×10 cm area); second, crack formation complicates the signal processing used for measuring strain accuracy. Consequently, the strain distribution along the concrete beam cannot be predicted accurately by analytic structural theory.

The purposes of designing this concrete beam test are:

1) Although optical fibers are generally well protected within the GFRP rod, no previous experiments have been done to verify whether the distributed sensing fiber has good agreement with the conventional strain gauges in determining strain information from

a GFRP rod. Any discrepancies would need to be compensated by calibration techniques.

2) The GFRP rod performs well under tension, and poorly under compression. Thus, it is important to verify whether the fiber embedded in the rod reflects this behaviour as well. More importantly, when the fiber was made as one strand of fiberglass rod, it was impossible to pre-tension the fiber for compressive strain measurement. Clearly this compression mode test can verify the capability of the distributed Brillouin scattering sensor for compression measurement.
3) With fiber both embedded in the GFRP rod and bonded to the steel reinforcing bar in the same concrete beam at the same height, we can make a direct comparison of the protecting performance between the epoxy-glue and the GFRP rod.
4) Recently, the lightwave technology of our distributed sensor system has been modified [DeMerchant 2000] to check whether the new improvements bring in better performance in terms of strain measurement accuracy. The new improvements include: i) the introduction of a power check and correction at the signal processing end for laser power fluctuation, and feedback control on the electro-optic modulator to get the best extinction ratio and fixed pulse width for the optical pulses, which provides the spatial resolution, and ii) the introduction of the digitizer/signal averager and Y-balanced bridge modulator.

It is believed that with this investigation we can collect valuable data for both application of distributed Brillouin sensing system and fiber installation in the realistic civil engineering structures, as well the sensibility of a Brillouin sensor.

5.2 Experimental Set-up and preparation

Reinforced concrete beam

The reinforced concrete beam was 1.65 m long with dimensions 100 mm x 200 mm, and was fabricated using 50 MPa concrete to allow it to gain sufficient strength prior to the fourteen days of flexural testing. The concrete had a modulus of elasticity of 29 GPa at the

time of testing. The beam was reinforced with grade 400 hot worked deformed steel bars where two 10M (10mm diameter) bars were used at the top and two 15M bars at the bottom. The concrete cover was 15 mm. Both ends of the bottom bars were bent into 90° hooks to provide anchorage. The beam was designed based on CSA Standard 23.3-94, and was made to incorporate two methods of optical fiber protection. The first method involved the embedding of fibers within pultruded GFRP rods to increase their rigidity and resistance to mechanical and chemical damage. The second method is to bond the fibers to steel reinforcing bars with epoxy adhesives to prevent the fibers from reacting with concrete materials of high alkalinity. By bonding the fibers to the reinforcement, they can be kept straight to protect them from damages. To properly align the fiber in this fashion, the surface of the side bar was ground smooth prior to bonding.

Fiber installation

Figure 5.1 shows the layout of the rebars and rods inside the formwork of the concrete beam. (1) is the top GFRP rod, the testing result of the optical fiber within this rod named CR, (2) is the bottom GFRP rod, the testing result of the optical fiber in this rod so called TR. In the same way, (3) is top the steel reinforcing bar and (4) is the bottom steel reinforcing bar, the testing result obtained from the optical fiber bonded on these rebars are named CS and TS, respectively. Here C means compression, T means tension, R means sensing fiber embedded in GFRP rod, and S means sensing fiber bonded to the surface of the steel reinforcing bars.

It is important to note that the terms "fiber steel" and "fiber rod", refer to measurement of the reinforced steel bars and GFRP rods using the distributed optical fiber sensor.

The sensing fiber was divided into three passes that connected to the Brillouin scattering based distributed sensing system respectively. The first pass was the compression rod (CR) fiber spliced to the compression steel (CS) fiber, the second was tension rod (TR) fiber, and the third was tension steel (TS) fiber. The fibers in the CR and TR were embedded with polyimide-coated optical fibers inside 9.4 mm pultruded GFRP rods. Each embedded fiber in

the rod had an overall diameter of 155 μm with a core diameter of 10 μm and a cladding of 125 μm.

Acrylate-coated optical fibers were bonded to the steel reinforcements (CS and TS) using a high-strength, structural, epoxy paste adhesive. These Corning PVC buffered SMF-28 single mode fibers were pre-tensioned, and then bonded to the steel reinforcing bars to prevent buckling of the fibers when tested under compressive forces.

Light weight, high strength, high stiffness, and resistance to corrosion are among the compelling reasons that make GFRP rods attractive for use in smart structures. The GFRP rods were fabricated at Dalhousie University using the pultrusion system [Kalamkarov et al. 1998] with continuous E-glass filaments in a urethane modified bisphenol-A based vinyl ester resin system with a single strand of polyimide-coated optical fiber located at the centre of the composite. The polyimide coating of the optical fiber helps to protect the fibers from high temperature induced by the curing process.

The top surface of the rods were coated with a 2 mm layer of epoxy and sand to improve the interfacial bonding between the rod and concrete to prevent slippage. Also, the ends of the beam were extended 150 mm beyond the supports to provide an anchor for the pultruded GFRP rods. In addition, the loading level of the beam was kept low to minimize the bonding stress between the GFRP rods and the cement. In spite of these precautions, it appears that the significant slippage of the GFRP rods occurred in the concrete as the fiber within the rod was subjected to a much lower strain than the fiber bonded to the reinforced steel bars.

Conventional strain gauges layout and loading method

In order to compare the distributed fiber sensor results with conventional sensors, two types of conventional point sensors were placed at the mid-span of the concrete beam: 1) Electrical Resistance Strain (ERS) gauges, attached to steel reinforcing bars; 2) Mechanical Strain (MS) gauges, glued to the sides of the concrete beam.

The ERS gauges were attached at the top and bottom surfaces of the reinforcement at mid-span. The ERS gauge system operated within a 3-6 mm gauge length, while the MS gauge

system, which consisted of eight pairs of demec points glued to each side of the reinforced concrete beam, operated within a 50 cm gauge length.

Figure 5.2 shows the design of the reinforced concrete beam with the layout of the fibers, ERS gauges, and MS gauges, as well one and two-point loading methods. The ERS gauges bonded to the top of the steel reinforcing bars were located at the same elevation for comparing strain results and to monitor the performance of the gauges during each test.

Both one and two-point loading tests were applied to the concrete beam at its mid-span as shown in Figure 5.3 and 5.4. In the loading test, the beam was loaded by the crosshead of the testing machine causing a downward deflection placing the top of the concrete beam in compression and the bottom in tension with a 1.35 m clear span. Before each load was applied, the unstrained state readings were recorded as reference measurements by the distributed sensing system and ERS gauges. As the load capacity of the concrete beam was 51 kN (11473.1 lb) for both types of tests due to governed shearing, the maximum load of 24.5 kN (5500 lb) was applied in twelve equal increments.

5.3 Experimental Results and Discussion

In an effort to address some of the shortcomings of the various curve-fitting methods of analyzing complex Brillouin spectra, the spectrum centroid method of analysis was used in this study as presented in the section 3.4.1. This method represents the average strain of a fiber section subjected to nonuniform strain distribution between two neighbouring points (5 cm in this study). Strain distributions were calculated from the Brillouin shifts with the equation 2.28. The strain coefficients, C_ε, were measured as 17.42 με/MHz for the CS and TS, 16.2 με/MHz for CR, and 15.7 με/MHz for TR fibers, respectively. Because the fiber was glued to steel bars with epoxy for CS and TS, the strain coefficients are the same as for both CS and TS. For CR and TR, fiber was used on one strand in GFRP during formation process; strain coefficients are different for both glass rods.

Test results of fiber optic sensing

The relationships between strain, load and position are shown in Figures 5.5 ~ 5.8 for both one-point and two-point loadings on the GFRP rods and reinforced steel bars, respectively. The applied load ranged from 0 to 24.45kN (5500 lbs) and was added progressively by 2.22kN (500 lbs) weight increments. The positions along the sensing fiber were identified by meter. In Figures 5.5 ~ 5.8, the position "0m" corresponds to the mid-span of the concrete beam. The strain was directly proportional to load for both one and two-point loading and the maximum strain occurred at the mid-span of the concrete beam for different loads.

The length of the concrete beam is 1.65m; between two supporting points (under the beam) is a 1.35m clear span. One-point loading was applied to the concrete beam at its mid-span. There is a 0.61m interval between two parts of the crosshead of the testing machine in two-point loading case. The beam was loaded by the crosshead giving a downward deflection, equivalent to the top of the concrete beam in compression and the bottom in tension.

Both fiber steels and fiber rods can measure strain distribution of the same concrete beam at different positions. We believe the fiber on steel tends to measure the localized strain, as it was glued to the steel bar by epoxy; while the fiber rod tends to measure the strain response of the GFRP rod, as the fiber is in the middle of the rod, which is similar to the structured strain.

Figure 5.5 shows the tensile strain measurements for the fiber steel (TS (1p), Figure 5.5(a)) and fiber rod (TR (1p), Figure 5.5(b)) with one-point loads at different positions along the concrete beam. Figure 5.5 (b) corresponds to fiber rod strain; central loading point has highest strain, as expected. Inside the region between two support points (1.35m), TS (1p) and TR (1p) show almost same strain distribution with different loadings. The strain values of TS (1p) are bigger than that of TR (1p), caused by the average effect of the GFRP rod. The two ends of TS (1p) go to up, due to the 90° hooks of the bottom rebars.

Figure 5.6 shows the tensile strain measurement for two-point loadings on the concrete beam. The obvious unsymmetrical feature was revealed in a plot of tensile strain versus position for the fiber rod (TR (2p)). TS (2p) and TR (2p) show nearly same high strain values around the mid-span. Two sub-peaks around –0.5m and 0.7m in Figure 5.6(b) and two lower strain sections among three peaks correspond to two supporting points, two loading points and

the force balance between loading points and supporting points. Fiber on steel did not have these low strain sections, as the rod detects the structural strain with average strain effect responding from the load to the rod, while fiber on steel measures localized strain. The central maximum values in both Figure 5.5(b) and Figure 5.6(b) represent the highest tension.

This asymmetry may arise from a non-uniform property of the concrete beam. As the two-point loading experiment was conducted after several one-point loading experiments, the concrete beam showed signs of fatigue while being lead into the inelastic regime, resulting in its asymmetrical response. Two weakly strained sections of TR (2p) around the – 0.2 m and 0.4m are induced by the fact that the loading and supporting points are measured in the same spatial resolution section. The resulting strain values are diminished as the centroid signal processing provides an average strain over a region where the opposing forces of the load and supports interact destructively with one another. In general, when two opposite strains are measured together in one measurement zone, the total strain will be minimal.

The optical fiber used for distributed sensing was embedded in the middle of the GFRP rod. As a result, the fiber was indirectly measuring the strain response of the rod due to an applied load on the concrete. On the other hand, the fiber bonded to the surface of the steel bar measures the concrete response to the load directly, providing a localized strain measurement. This has been confirmed by the results of two-point compressive loading. For one-point loading (TS (1p) case), the low strain at –0.7 m and 0.6 m correspond to the supporting points, while the high strain at two ends correspond to the bending of the 90° hooks located at both ends of the 15M rebars, although both positions are not at the concrete edges. The tension was transferred through the shear force.

Figure 5.7 and Figure 5.8 show the compressive strain measurements for the upper fiber steel (CS) and fiber rod (CR) with one-point (Figure 5.7) and two-point (Figure 5.8) loading at different positions along the concrete beam. As expected, the maximum compression is observed at mid-span for both one-point and two-point loadings. The strain in one-point loading is very symmetric to the central point of the concrete beam, while the strain in two-point loading is not symmetric on both sides of the beam. As explained previously, the two-point loading experiments were conducted after a series of one-point loading tests. Although the loads were kept low to maintain the elastic response of the beam, the concrete may

continue to generate cracks after a few one-point loading tests, resulting in an inelastic response from the beam afterward. Therefore, the cracked beam indicates an asymmetric strain response for both tension and compression modes. Crack formation in the concrete is also a result of the limited support provided by only two steel bars embedded within the cross section of the beam. The loading condition simply overwhelms the concrete structure without further support, resulting in crack formation.

Comparison of the test results with conventional gauges

To compare the distributed fiber sensor results with those of conventional strain gauges, Figure 5.9 ~ 5.12 reveal the mid-span strain values of the concrete beam as measured by these sensors for the one point loading compression mode (Figure 5.9), tension mode (Figure 5.10), two point loading compression mode (Figure 5.11), and tension mode (Figure 5.12). The abscissa is the load applied in kilo-Newton and the ordinate is the strain value measured in microstrain ($\mu\varepsilon$). Four measurements are based on (1) fiber embedded in pultruded GFRP rods; (2) fiber bonded to the steel reinforcing bars; (3) ERS gauges located in the middle of the steel reinforcing bar, and (4) the MS gauges on the surface of the beam. The strain gauge readings are the strains adjusted to the position where the fibers are located using the structural analysis. When the distributed sensors were attached to the steel reinforcing bars, the measured strains vs. load curves are consistent for one and tow-point loading in both compressive and tensile modes.

Actually, ERS is the most acceptable strain gauge in industry and research labs. It measured localized strain over a 3 mm gauge length. MS strain gauges measure the strain over 500mm; therefore, a factor of 81% was incorporated to the strain readings at the midspan in order to compare with ERS readings. Normally, the performance of strain gauges is good in tension, but bad in compression case. That is why a large difference between the readings of ERS and MSG has been observed in compressive strain case.

The fibers embedded in GFRP rods give lower strain readings as the concrete strain is found indirectly by measuring the strain response of the GFRP rod, which causes a spreading of the strain distribution. Briefly, when the GFRP rod encounters the impact of the load, its

flexibility allows it to slightly buckle to support the load. This buckling causes a non-uniform strain distribution along the fiber length under measurement. Consequently, the average strain over such a fiber length will be diminished in contrast with direct loading for the steel beam, as illustrated in Figure 5.13. Without its flexibility, the GFRP rod, along with the optical fiber, would simply fracture under large loads.

For two-point loading cases under tension mode (Figure 5.12), the distributed sensor results for the steel reinforcing bars and GFRP rods agree favourably with the ERS gauges. As explained previously, the GFRP rod tends to yield diminished average strains. However, under ideal two-point loading conditions, the strain between two loading points is constant for certain loads. As a result, this strain averaging effect would not be revealed, unlike the one-point loading case. During one-point loading, the strain changes rapidly near the mid-span point. Therefore, the spreading of the strain distribution caused by the GFRP rod is the main reason why its strain measurement differs from those of distributed measurements of the reinforced steel. For the two-point loading compression case (Figure 5.11), the distributed fiber sensors and electrical strain gauges yield equivalent strain readings for both the GFRP rod and reinforced steel materials.

The strain measurement accuracy is ±15 με (μm/m) according to the system calibration in the laboratory environment with non-uniform-distributed strain and ±5 με with uniform strain distribution. This was obtained with many repeated experiments to determine the accuracy. The straight lines in Figures 5.9~5.12 are linear regression lines. For distributed measurements of one-point loads, the standard deviations were estimated as 7.3 με and 15.0 με for fiber embedded in GFRP rod and bonded to the steel reinforcing bars, while increasing to 20.0 με for both fiber rod and fiber steel in the two-point load test respectively. The larger fluctuation in two point loading case may be due to the concrete beam's inelastic response, so called fatigue of the concrete beam, as the one point loading experiment was conducted first.

The distributed fiber sensors used in this experiment provided accurate strain measurements, particularly with fiber bonded to reinforced steel. Based on the results given above, we can draw the conclusion that the epoxy coating effectively protected the fibers, and transmitted the concrete strain to the fiber efficiently. The fibers embedded in the GFRP rod work well under uniform strains, i.e. at the mid-span of two-point loading. However, in

situations where high strain gradients occur, the strain information is averaged within the spatial resolution, resulting in lower strain readings. Such cases were found predominantly during the one-point loading cases.

According to Ansari and Yuan, the mechanical properties of the fiber protective coating, the glass core (core and cladding), and the length of fiber in contact with the structural material (gauge length) will affect the strain transduction capabilities of the optical fiber sensor [Ansari and Yuan 1998]. This is another mechanism that might contribute to the lower strain measured by the GFRP rods. The primary function of the fiber coating is to protect it from brittle fracture when partial mechanical energy is directed at what is absorbed by the cushion-like coating or lost through the interface shear transfer between the coating and the core. Consequently, the fiber core senses only part of the strain. In addition, the thick coating of the rods, which include the E-glass fibers and the vinyl ester resin, likely absorbed a portion of the strain.

5.4 Summary

This experiment has successfully demonstrated the ability of the distributed fiber optic sensing system to measure strain at different locations along a concrete beam. Both methods, fiber embedded in GFRP rod and fiber bonded to steel reinforcing bars, were found to effectively protect the optical fiber strand. The distributed fiber sensor strain resolution varied between ±7--20 με depending on the fiber installation method and the strain gradient. The spatial resolution of the system is 50cm in this experiment with a 5cm read-out resolution. The strain values measured from the optical fiber matched well with conventional strain gauge readings for the reinforced steel, while fibers embedded in GFRP rods worked well under uniform strain, but not very well under non-uniform strain.

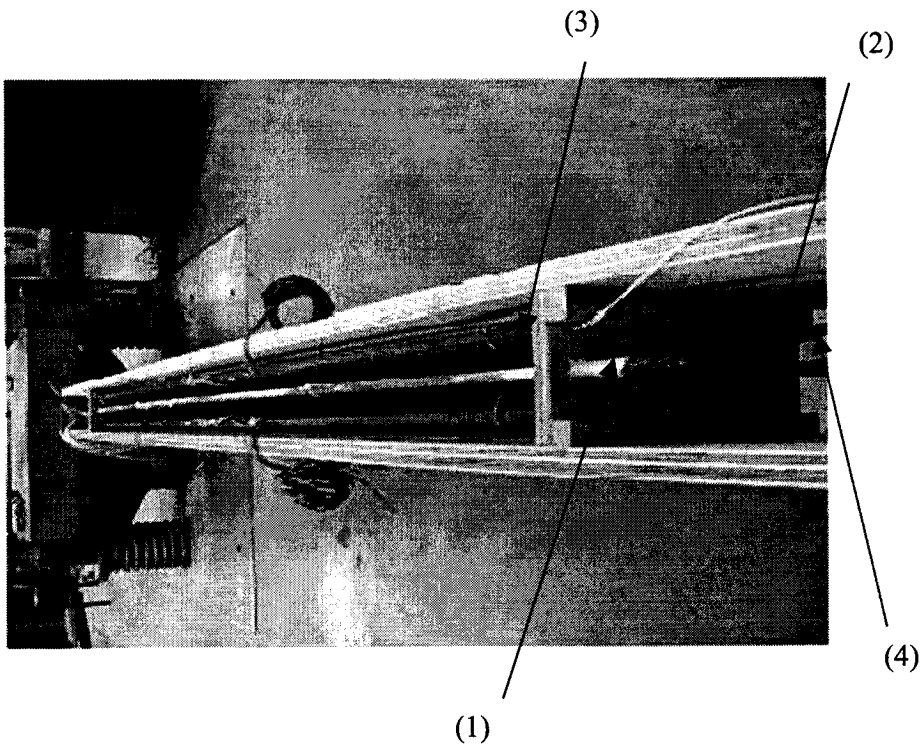

Figure 5.1 Layout of the rebars and rods inside the formwork of the concrete beam.

(1) Top GFRP rod, the testing result of the optical fiber in this rod named CR

(2) Bottom GFRP rod, the testing result of the optical fiber in this rod named TR

(3) Top steel rebar, the testing result of the optical fiber on this rebar named CS

(4) Bottom steel rebar, the testing result of the optical fiber on this rebar named TS

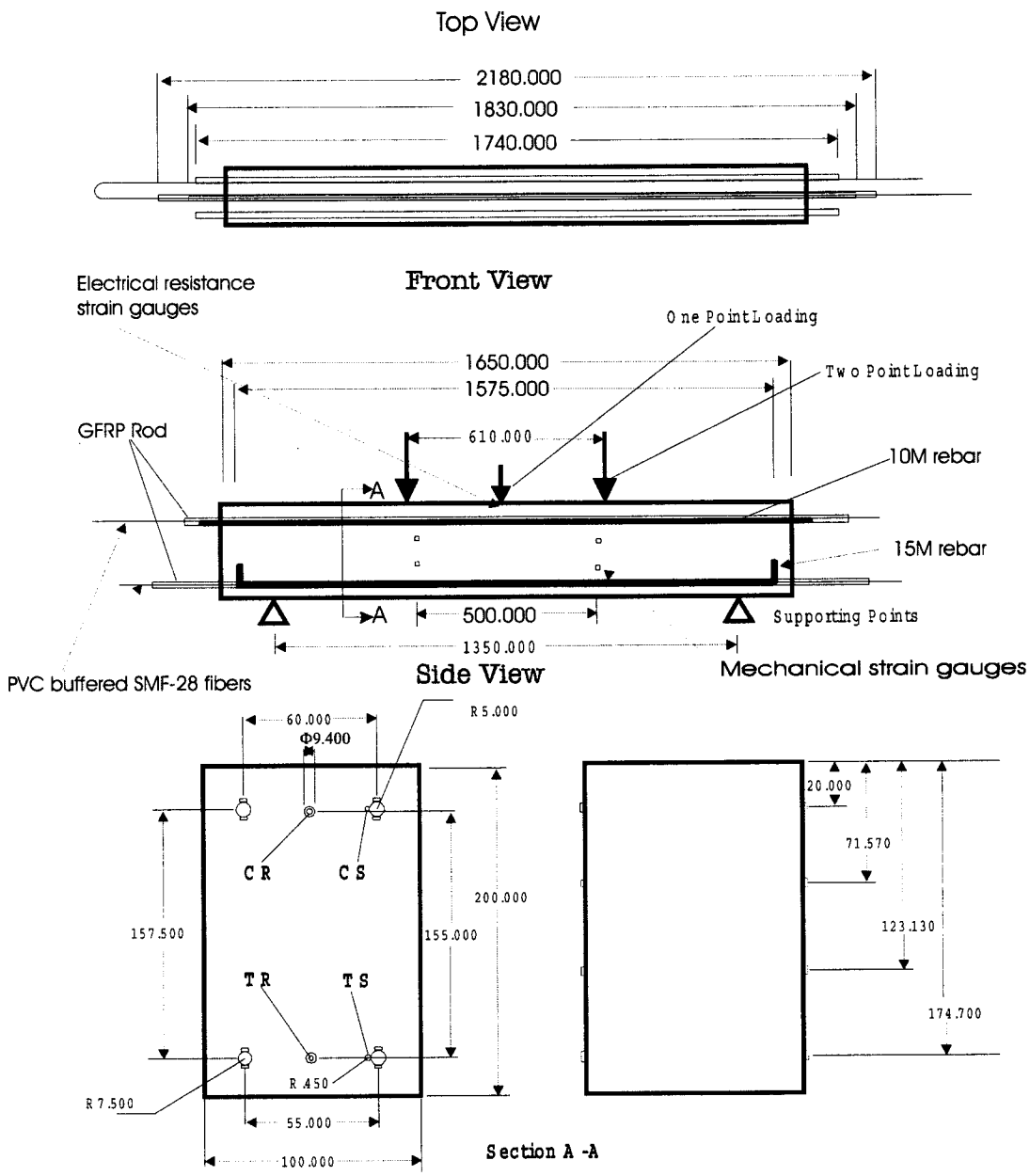

Figure 5.2 Reinforced concrete beam design with sensor and gauges layouts.
CR---Compressive Strain of Fiber in GFRP Rod
CS---Compressive Strain of Fiber on Steel Reinforcing Bar
TR---Tensile Strain of Fiber in GFRP Rod
TS---Tensile Strain of Fiber on Steel Reinforcing Bar
All measurements are in mm.

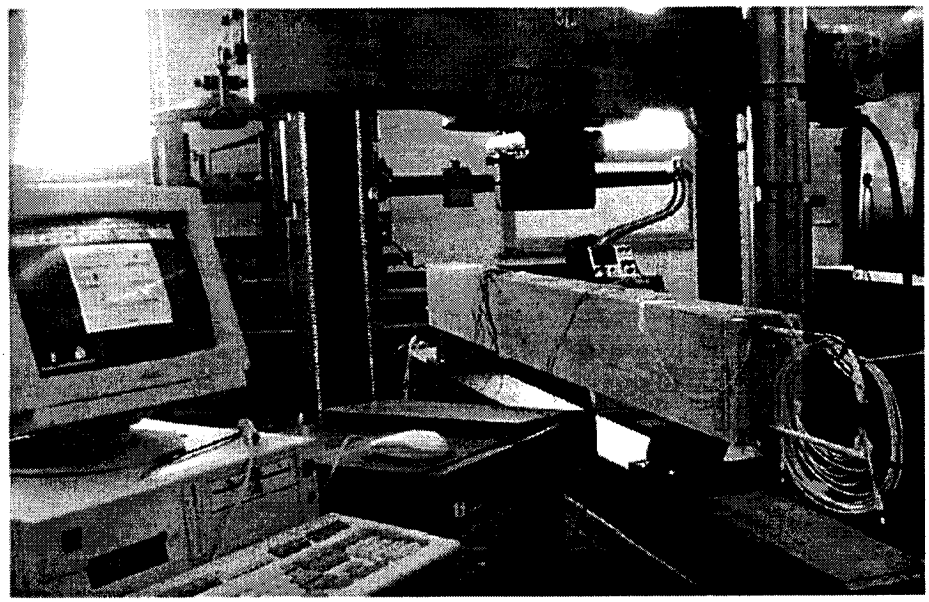

Figure 5.3 One-point load tests. A Baldwin Universal Testing Machine was used to applied loads to the reinforced concrete beam at mid-span.

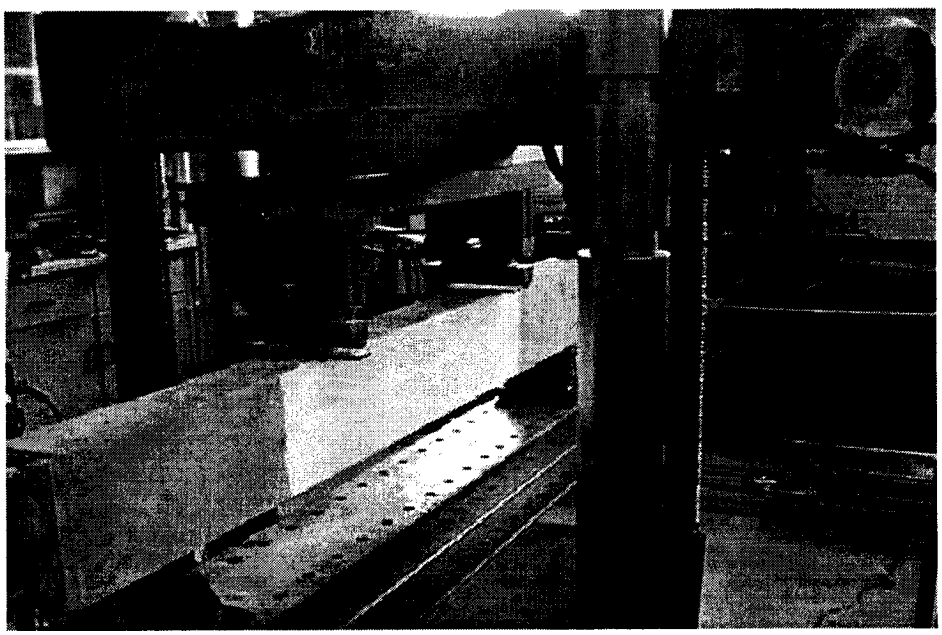

Figure 5.4 Two-point load tests

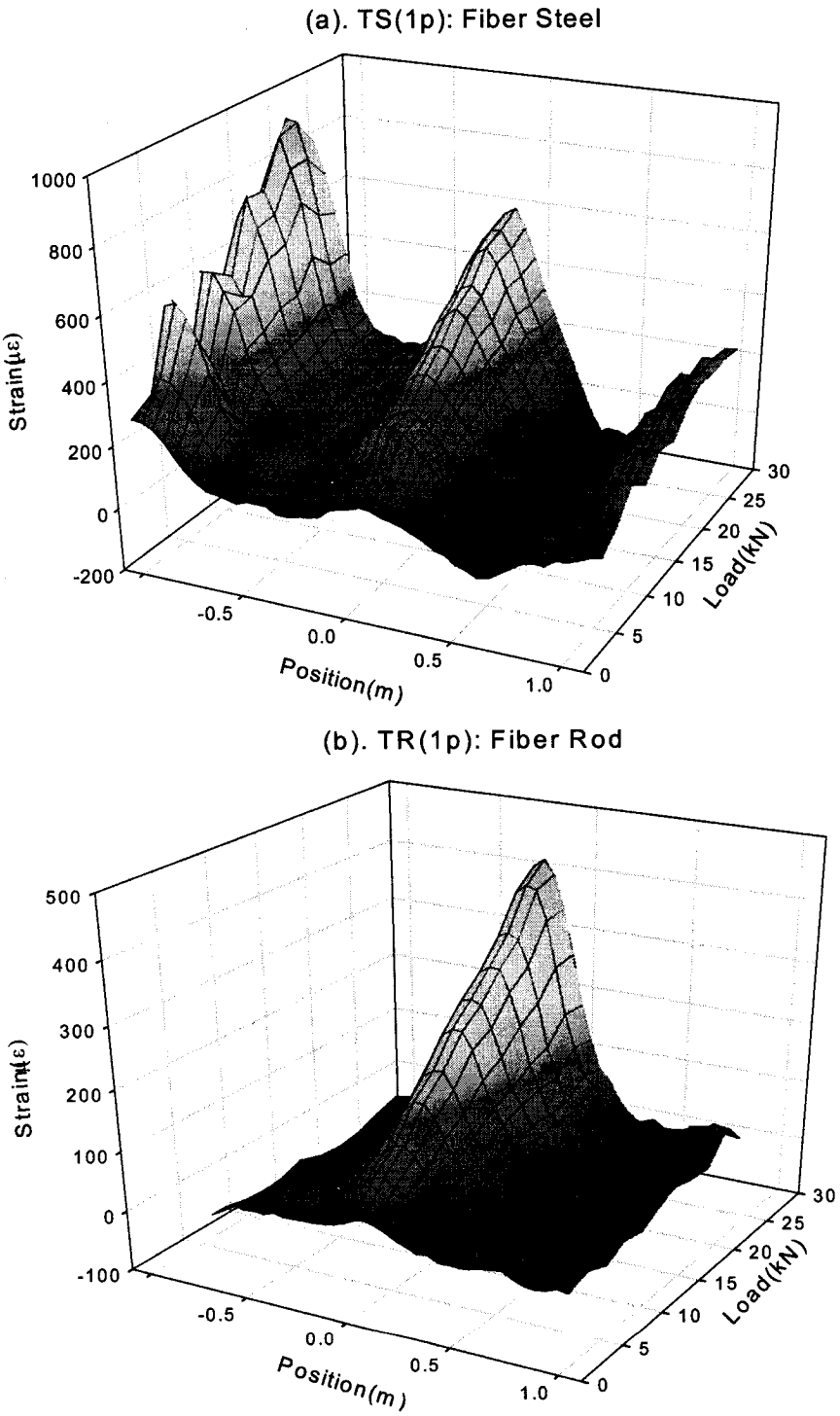

Figure 5.5 One-point load tensile strains measured by the sensing fiber (a) bonded to the steel reinforcing bar and (b) embedded in the GFRP rod.

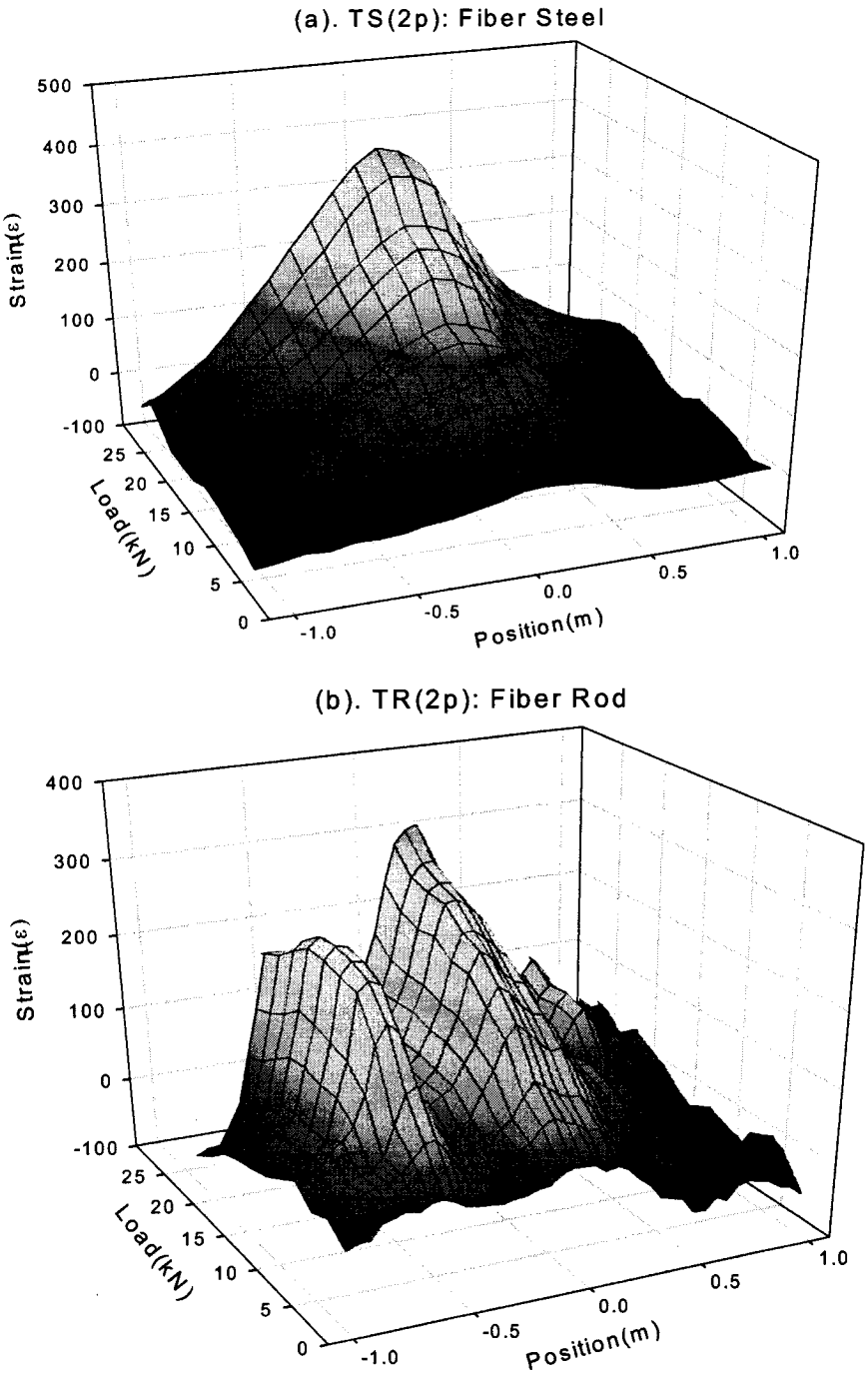

Figure 5.6 Two-point load tensile strains measured by the sensing fiber (a) bonded to the steel reinforcing bar and (b) embedded in the GFRP rod.

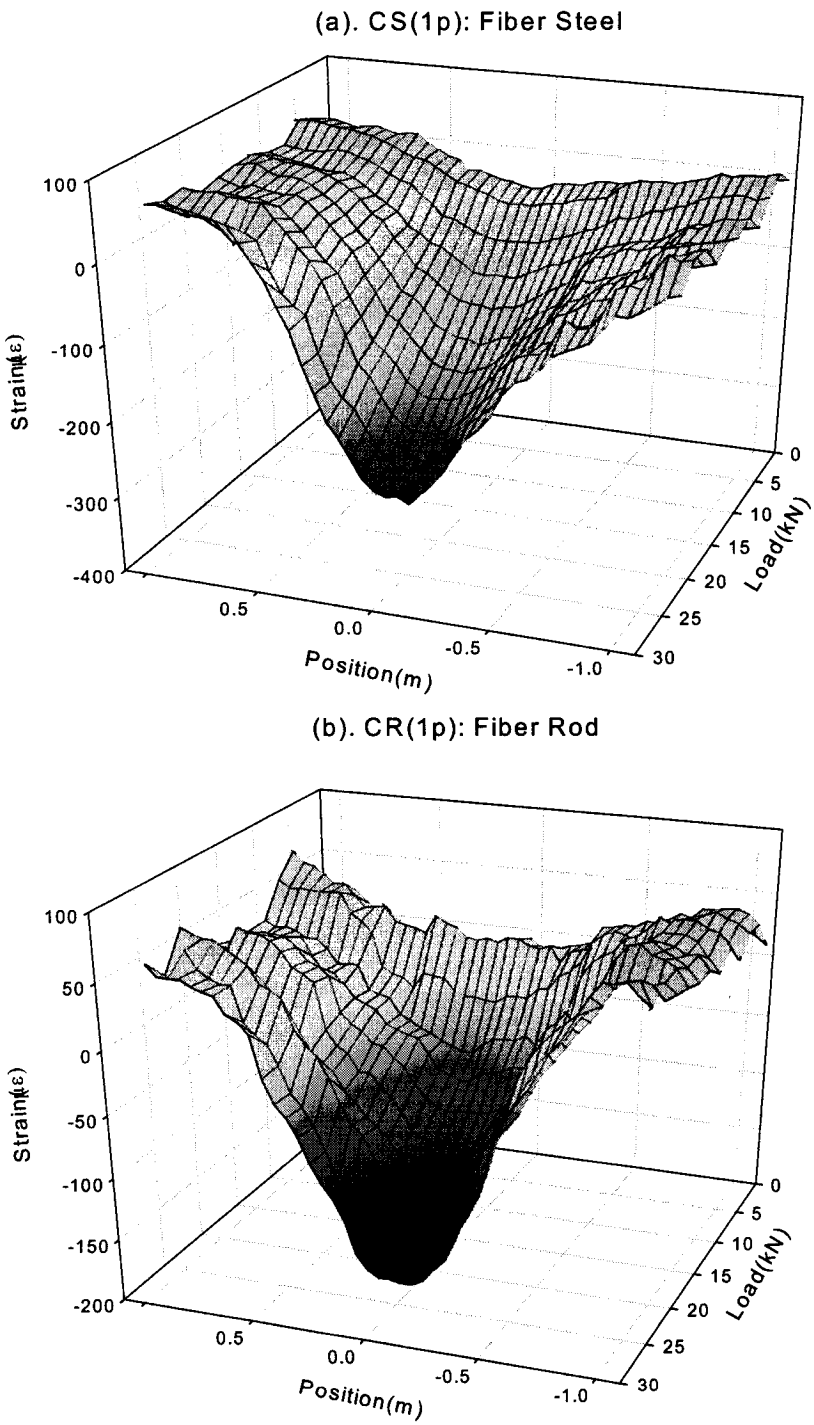

Figure 5.7 One-point load compressive strains measured by the sensing fiber (a) bonded to the steel reinforcing bar and (b) embedded in the GFRP rod.

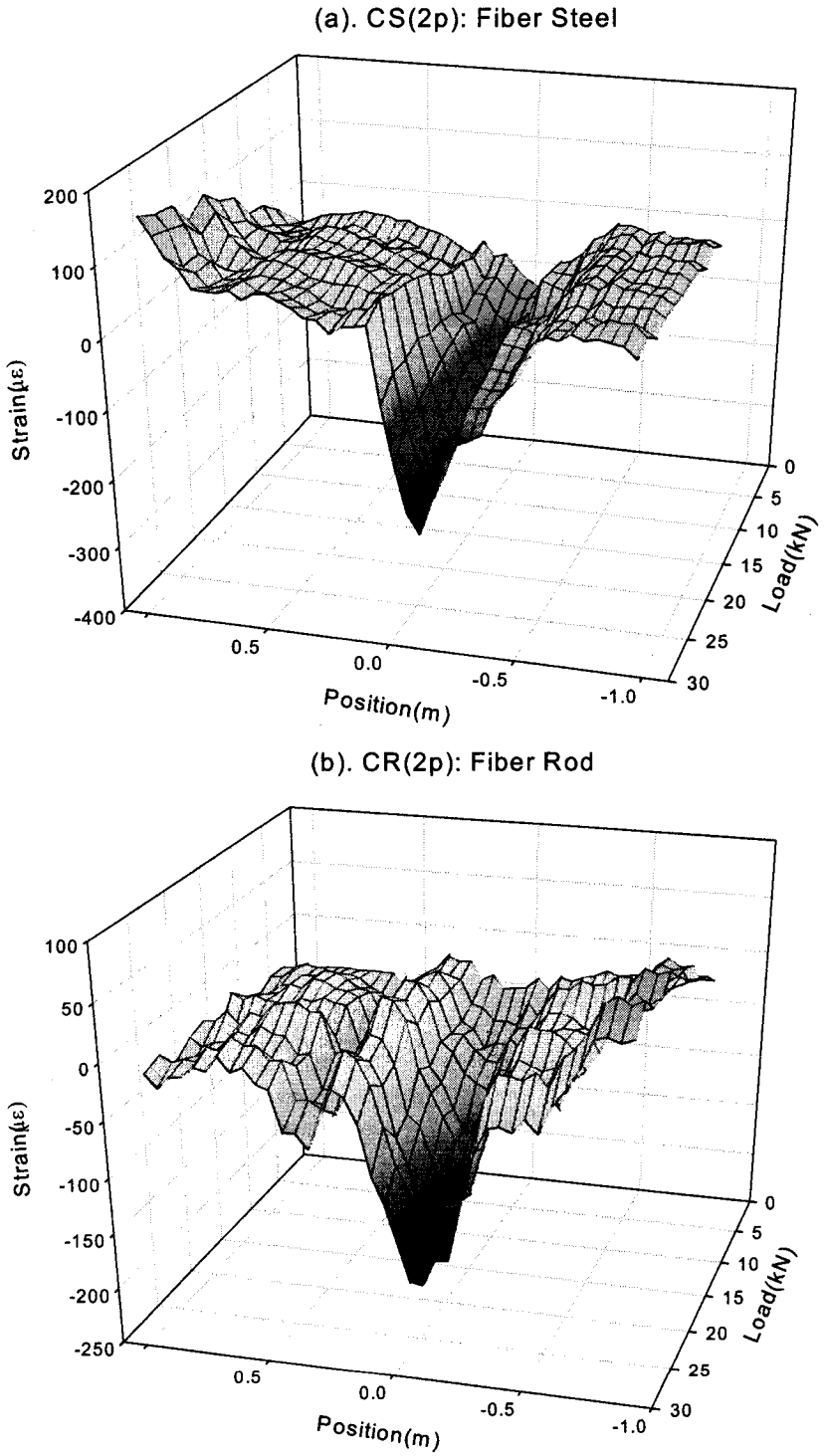

Figure 5.8 Two-point load compressive strains measured by the sensing fiber (a) bonded to the steel reinforcing bar and (b) embedded in the GFRP rod.

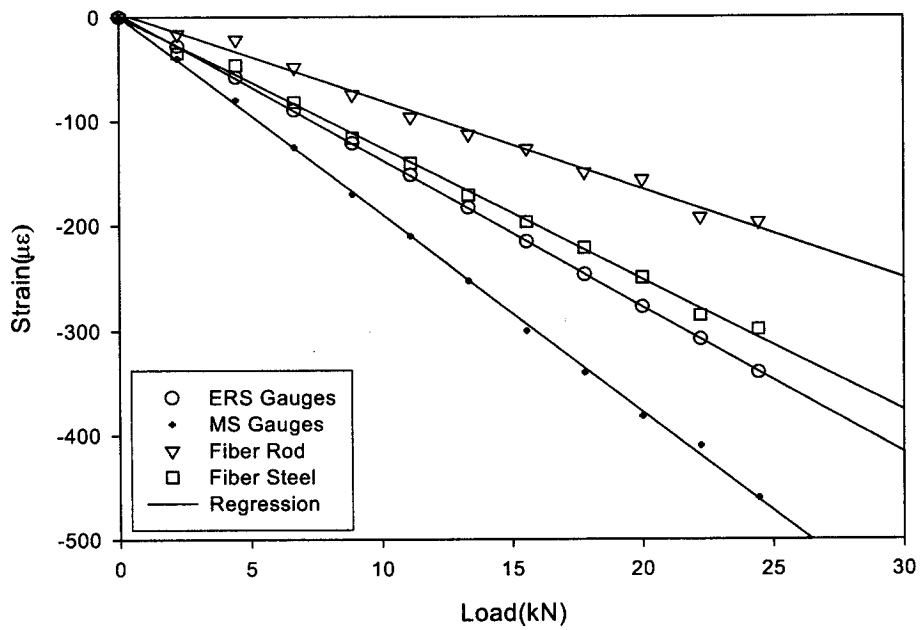

Figure 5.9 Comparison of one-point load compressive strains acquired from different strain gauges.

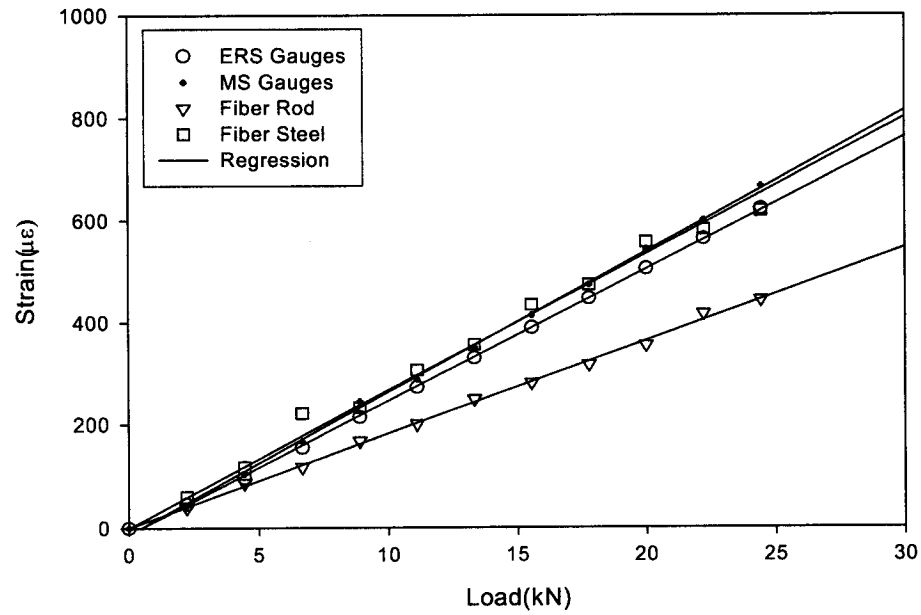

Figure 5.10 Comparison of one-point load tensile strains acquired from different strain gauges.

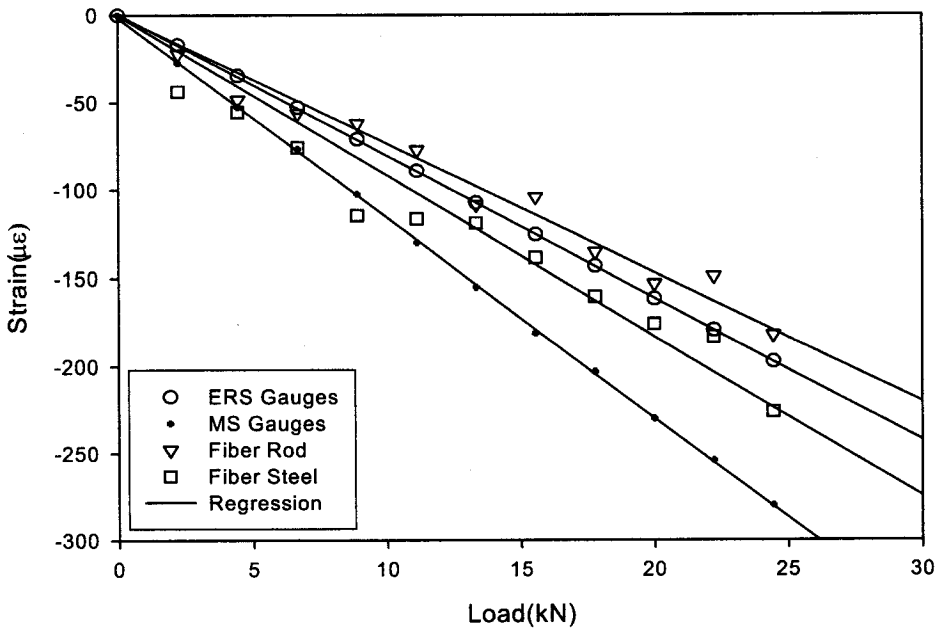

Figure 5.11 Comparison of two-point load compressive strains acquired from different strain gauges.

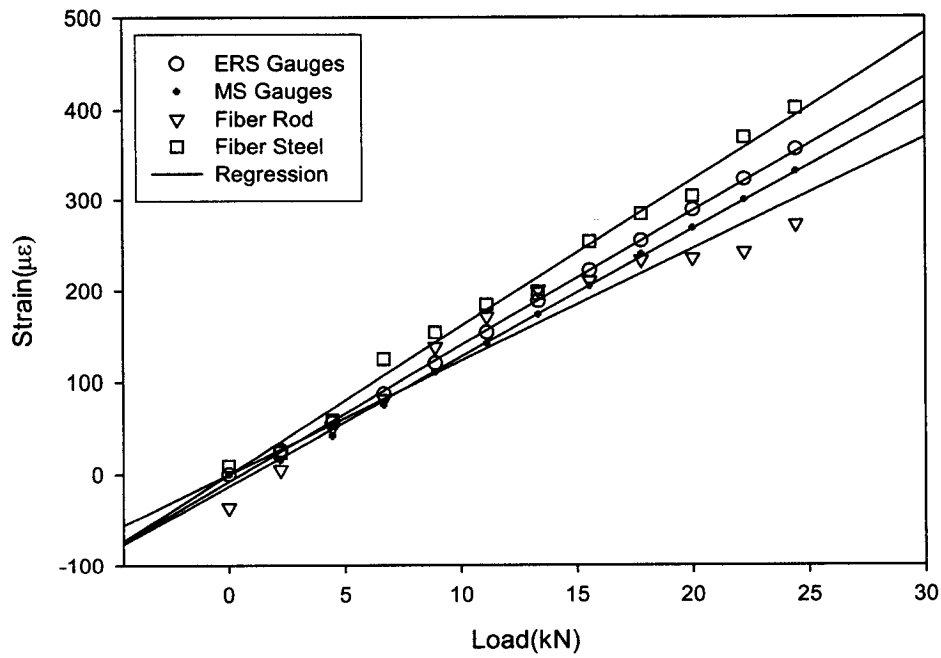

Figure 5.12 Comparison of two-point load tensile strains acquired from different strain gauges.

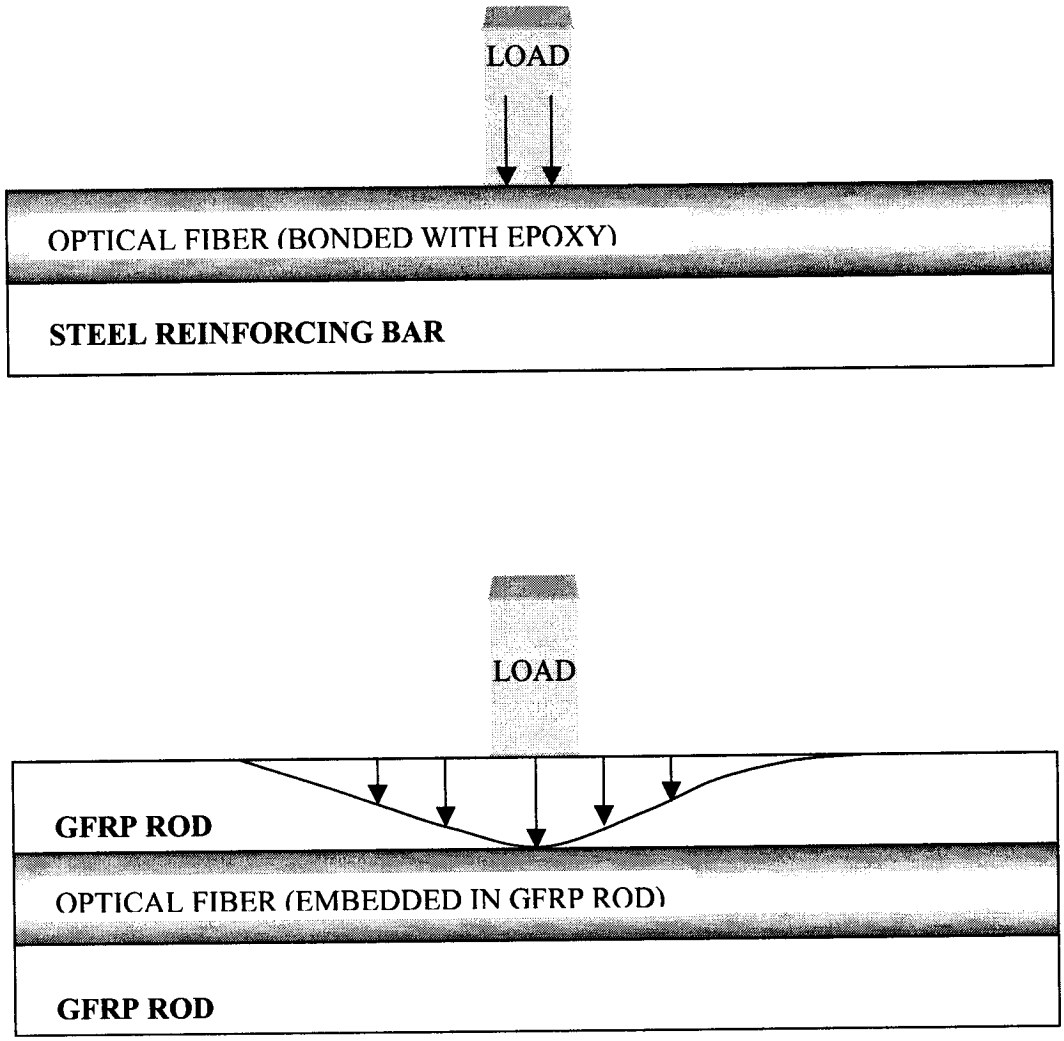

Figure 5.13 The impact of loading for two different methods of fiber installation. The optical fiber measures the full load directly when bonded with epoxy (top), while the GFRP rod creates a spreading of the strain distribution, allowing the fiber to measure only a partial strain (bottom).

Chapter 6

Temperature and Strain Monitoring of Composite Curing Process

The use of embedded fiber optic sensors for cure monitoring of thermoset-based composite materials has been recognized as a very useful technology for reducing the autoclave processing costs of composite aerospace parts. The technique is flexible and virtually non-intrusive since the diameter of the optical fiber is as small as 170 μm. The properties of the composite materials are found to strongly depend on the processing stage. The key points to improve the quality and reliability of these materials have been identified in the cure monitoring and the optimization of the manufacturing process. In particular, the curing process of the polymeric matrix is the most critical and costly stage in the manufacturing of composite structures [Mijovic et al. 1993; Cusano et al. 2001]. During a cure cycle, the *in-situ* temperature, viscosity, pressure and cure state of the thermoset resin are continuously evolving. It is difficult to accurately predict how these critical parameters change during cure, although they directly affect the quality of the final part, e.g. defects and process-induced warpage. They are usually unknown since they depend on part and tooling geometry, materials, and the autoclave loading. Thus, significant variation can occur across a single composite part. To compensate for the lack of information, very conservative and lengthy process cycles are used in commercial manufacturing.

As presented in previous chapters, the most useful application of distributed Brillouin sensing is strain and temperature monitoring. This led to an interest in determining if the Brillouin shifts are proportional to either strain or temperature. During the strain measurement

of a civil structure, the temperature changes slowly due to the huge volume of the civil structure and its effects can generally be neglected. However, in the composite material curing process, the temperature is increased by 177°C within 60 minutes. This means we should deduct the temperature contribution from the Brillouin frequency measurement to get the strain information. We can measure strain and temperature simultaneously using the combined Brillouin power and frequency with temperature measurement accuracy of 3.9°C and strain accuracy of 178 με at a spatial resolution of 3.5 m [Smith et al.1999b]. However, this spatial resolution is not adequate for curing monitoring of the composite material that has a total length less than one meter.

In this investigation we used two optical fibers placed adjacent to each other. One fiber was isolated from any strain effects to monitor the temperature, while the other measured the effect of both strain and temperature. In this way we can measure both strain and temperature at centimeter spatial resolution. We used a peak detection method for combined strain and temperature measurements at different heating and cooling stages for this curing monitoring experiment, so that we measured both temperature and strain simultaneously. The experiments were conducted with 15 cm spatial resolution and 5 cm readout resolution that is the distance between two neighboring points in the strain/temperature measurements in the time-space domain.

The objective of this investigation is to combine the real-time cure monitoring capability of a single mode fiber with intelligent software to develop a closed loop intelligent production control. Strain is used here to indirectly measure the changes in the curing state since the epoxy and composite matrix resin will shrink upon gelation and vitrification. In cure monitoring of composite parts with large and complex shapes, distributed sensing offers significant advantages over point measurements, since it can sense a greater surface area and points of interest that do not have to be identified beforehand.

6.1 Experiment

Material

Composite panels used in this study were made by laying up to 16 layers $[0_{16}]$ of AS4/3501 unidirectional carbon fiber/epoxy pre-preg tapes. AS4/3501 is a high performance composite widely used in aerospace applications. The 3501 resin is an amine-cured epoxy system that is usually cured at 177°C. Due to the high temperature processing, a single mode optical fiber with Pyrocoat polyimide coating supplied by Lucent Technologies was chosen as the sensing fiber that has a temperature range from –65 to +350°C and an external diameter of 155 μm.

Composite panels

In order to measure shrinkage, the optical fiber was pre-strained by hanging a load of 3.47N on one end. An arrangement of a 485×100×6.35 mm aluminum tool plate with a small pulley, a fixed-block, and a slide-block was used to keep the pre-strained optical fiber taut after embedded in the 16-ply panel, as illustrated in Figure 6.1. This pulley experiment was designed with the intent to measure the shrinkage and expansion of the composite material.

The optical fiber was defined with A to G to represent temperature and strain at different sections. A layer of release nylon film was laid on top of the plate before laying up the panel. The panel was prepared manually by laying and debulking (30 minutes) two layers of pre-preg at a time. The pre-tensioned fiber was embedded longitudinally in the center at the eighth ply. To hold the optical fiber in place, the fiber was glued onto metal blocks at the point A and G as shown in Figure 6.1.

As both temperature and strain are a function of the Brillouin frequency, in order to separate the contribution, the fiber was deployed with two paths to measure. The first path is for temperature sensing that is labeled as C in Figure 6.1 and was isolated from strain by inserting the fiber into a 1-mm inner diameter polymer tube before embedment. The second is for both strain and temperature in section E due to the resin shrinkage/expansion induced in the curing process. During the analysis of Brillouin frequencies, the temperature contribution

in E would be deducted from the reference side to obtain the strain information. Before curing, the Brillouin frequency at initial state was measured to get the reference frequency. Any variation in strain in the curing process was then recorded with respect to this reference frequency.

6.2 Test

Curing process

The composite material is made of carbon fiber and partially cured epoxy resin. There are different epoxies with different curing rates etc. At room temperature the separate constituents are liquid and when combined chemically react to form a solid. The curing process results from cross-linking of the polymer molecules. The epoxy in the composite material is half-cured, i.e. the chemical reaction is half complete, and therefore it is a semi-solid. When heated to 177 degree Celcius in the autoclave (oven), the chemical reaction starts again. The degree of cure (DOC) is hence the level of cross-linking. The highest theoretical degree of cure is 100% but under normal curing we achieve about 90%, which is acceptable. The longer we heat it at the cure temperature, the higher the number...even to as much as 98%. In terms of mechanical and thermal properties, the strength, modulus and service temperature is maximum at the highest degree of cure. So we try to achieve that.

When curing, i.e. cross-linking and polymerization, occurs, there is a lot of heat produced during the chemical reaction. Usually, the DOC is found using differential scanning calorimetry, which is a measurement of heat flow as the epoxy cures. At the same time, the epoxy is also getting harder but it is difficult to measure hardness of a hot epoxy.

According to the curing schedule recommend by the manufacturer, the curing was performed in an air-circulating oven. The cure cycle consisted of heating up at 2.5°C/min and then holding for two hours at 177°C before cooling down at the same rate. Controlled cooling was achieved using carbon dioxide. A thermocouple was inserted into the center of the composite to allow comparison with temperature readings of the optical sensor. Throughout the entire process cycle, an 18-psi vacuum was applied. The variation of degree of cure

(DOC) as a function of time for this pre-preg using the present cure cycle has been obtained previously and is given in Figure 6.2 [Johnston 2001].

As shown in Figure 6.2, there are two curves representing the temperature in the oven and in the composite material. The oven temperature is higher than the material temperature during the heating and equilibrium stage, but lower when the oven cools off. The reason is that the material has the heat capacity to hold the temperature. The temperature difference between oven and material is in the range of 20°C to 30°C to hit the maximum curing temperature (solid-liquid) about 5°C for constant temperature (liquid phase), and 20~30°C again for liquid-solid transition. After the completion of the curing process, all the power switches and valves are turned off. During this process, the optical fiber will be integrated completely with the particular piles.

Measurements

The distributed Brillouin sensor was used to measure both strain and temperature distribution along the entire fiber length with a spatial resolution of 15cm. The system measured the Brillouin frequency shifts of sensing fiber to determine the strain and temperature at different locations using the Brillouin loss technique [Bao et al. 1995]. The time domain waveforms were taken with 500 averages. The scan range of the beat frequency was from 12.8 GHz to 13.4 GHz depending on the temperature and thermal strain of curing process. The frequency step of 5MHz was a good compromise between the speed of curing and the accuracy of the temperature measurement. The time gap between two consecutive measurements was 5 minutes.

For the dimension of the test panel shown in Figure 6.1 and the system parameters mentioned above, 4 to 5 data points can be obtained from each section of sensing fiber embedded in the composite. Only 1 to 2 of these data points can be considered as a direct monitoring of the internal strain and temperature, since the other points would include contribution from the free fiber length outside the composite laminate. For the temperature sensing section C, there is one peak in the Brillouin spectrum corresponding to the temperature as a function of time. On the other hand, for both temperature and strain sensing

section E there are at least two peaks, one comes from the temperature variation, while the other (maybe two or more depending on the strain distribution) corresponds to the strain variation. The normal average strain/temperature measurement method developed in our group uses the intensity integration to get the average strain/temperature. However, it cannot be used here, as strain and temperature peaks cannot be mixed. Hence, we used a peak detection method to get the temperature and strain.

Whenever a section of the optical sensing fiber is subjected to different strain and temperature, multiple Brillouin peaks will appear in the Brillouin spectrum. To illustrate this, the Brillouin gain spectra for the composite panel at adjacent data points of 118.5 ns (referred to as section A since contribution of A>B) and 119 ns (referred to as section B since contribution of B>A) at 177°C are shown in Figure 6.3. The values 118.5 and 119 ns represent the times after the launch of the pulse. The difference between these two points corresponds to a 5 cm distance along the fiber. Even though the data points every 5 cm can be measured, the strain contributions from two other neighboring points (±5 cm) within the 15 cm gauge length still appear in the Brillouin spectrum. It is due to the interaction of two counter-propagating pump and probe beams within one pulse width. In each curve of Figure 6.3 there are two Brillouin peaks corresponding to loose fiber in section A and pretension fiber in section B. It is clear that the signal strength of the left peak at 118.5 ns is stronger than the right peak, which means within the spatial resolution of 15 cm; the section A fiber length is longer than the section B fiber. Comparing at 119 ns, a reverse is seen in which the second peak shows a higher signal level, i.e., the section B fiber length is longer than A within the spatial resolution of 15 cm. Here, the net effects of temperature and strain in section B appear as a larger peak. Similar peaks were observed at points 128 ns (section F) and 128.5 ns (section G).

Since the data in Figure 6.3 is taken at 136 min into the process, the composite would have fully hardened/solidified as seen in Figure 6.2. The lower frequency (left) peak, ν_A, in section A gives the oven temperature's Brillouin frequency, while the right higher peak, ν_B, in section B has the combined effects of temperature, pretension, the thermal expansion of the fiber, and cure shrinkage at 177°C. Therefore, the difference between the peaks $(\nu_B - \nu_A)$ corresponds to the net fiber strain due to the combined effects except temperature.

To monitor the strain and temperature variation within the composite material during the cure process, we analyzed an additional length of 20 cm past section B, which is equivalent to the data point at 121 ns (section C, temperature in the composite). Similarly, a 20 cm length was deducted from section G to obtain the data at 126 ns (section E, temperature and strain in the composite). The Brillouin gain spectra for 121 ns and 126 ns are shown in Figure 6.4. It can be found that the highest frequency peaks for section C and E are different. The fiber length in section C has been inserted inside a tube to isolate the section from cure-induced contraction as the composite resin hardens with curing. Any strain change in section E is transferred to the fiber in section C (in the tube) via the section D pulley. Accordingly, the frequency difference $(\nu_E - \nu_C)$ would represent the net strain in section E due to curing. The deduction would remove the effects of the initial prestrain, pulley friction, and any rise in composite temperature, assuming that the chemical cross-linking exotherm is uniform throughout the entire composite panel.

When different sections of sensing fiber under varying conditions are simultaneously covered by one pulse, the different strains and temperature will be measured to give multiple Brillouin peaks in Brillouin spectrum. Even though we can measure the data points at every 5cm, the strain contributions from the neighbor points within 15cm gauge length will still appear in the Brillouin spectrum. This is due to the two counter-propagating beam interaction from both pump and probe beams within one pulse-width.

The Brillouin frequency shifts at each location/section were monitored throughout the curing process and then converted to its strain equivalent using the factor 1 MHz = 17 με. This was measured with our distributed Brillouin sensing system for the fiber we used in the composite curing experiment.

6.3 Test results

Temperature profile

Figure 6.5 shows the profiles of the Brillouin frequency at points of 116.5 ns, 121 ns, and 126 ns that representative of the sections A, C, and E, respectively. The 116.5 ns corresponds

to the loose fiber within section A. The process of the heat-up, isotherm hold, and cool down of the oven can be monitored with the section B. The slope of curve A during heat-up is 2.8 MHz/min, equivalent to 0.89°C/MHz using a 2.5°C/min heating rate. This agrees very well with the temperature/Brillouin frequency coefficient (C_T) of 0.80°C/MHz.

The nominal thickness of the panel after curing is 3.2 mm. Due to the relatively lower thermal conductivity of the AS4-3501 carbon fiber/epoxy composite; there is a thermal lag between the center ply of the composite panel and the oven. Figure 6.6 shows the thermal lag measured by the K-type thermocouple inserted at one end of the panel. The thermal lag of about 10 min is also seen in the Brillouin frequency shift during the heat-up stage for section C and E (as compared to section A) in Figure 6.5. The composite temperature is found to be slightly lower (about 5°C) than the oven setting temperature of 177°C at the isotherm hold as shown in Figure 6.6. During the cooling stage, the composite lags behind the oven cooling. It is also evident that it is difficult to achieve a constant cooling rate in an oven using carbon dioxide.

Net strain profile

To extract the net strain profile during cure, we subtracted the data at 126 ns (E) from that at 121 ns (C) to get the net change due to cure shrinkage in section E. Again, this assumes that the optical sensor inside tube section C is not insulated from the thermal changes within the composite. Hence, there is no difference between the temperatures in section C and E. This is a reasonable assumption as seen in the profiles in Figure 6.5. The net strain between E and C is obtained by multiplying the difference in Brillouin frequency shifts $(\nu_C - \nu_E)$ and strain conversion factor 17 με/MHz. Figure 6.7 shows the net strain profile during the cure process and the corresponding thermal profile (including lag) for the composite. There are four obvious phases of strain change due to the heat-up, isotherm, and cooling of the composite pre-preg. In the heat-up stage (S1), there is a net strain of about 680 με after 25 min of heat-up. The net strain is due to the thermal expansion of the optical fiber and aluminum pulley. The coefficient of thermal expansion for aluminum and the optical fiber is 28.7 and 4.55 με/°C [Chen et al. 1999; Faupel and Fisher 1997], respectively. Relative to section E, the

embedded fiber length in C would tend to be constrained by the presence of the surrounding carbon fibers even if the viscosity of the matrix resin has decreased considerably. The liquid matrix resin in C would start to gel or solidify after approximately 50 min (120°C) as in Figure 6.2. The degree of chemical cross-linking and viscosity of the resin would increase very rapidly from this point on, as shown in Figure 6.2.

At the start of the S2 stage, which is well before reaching the 177°C isotherm, the resin is about 60% cured and adheres to the optical fiber sensor. The sensor signal clearly begins to follow the resin shrinkage as cross-linking/vitrification progresses quickly. The coefficient of thermal expansion (CTE) of the carbon fiber is near zero. Cure shrinkage appears to be completed in 22 min with no further change in net strain in the isothermal hold stage (S3). Again, this agrees well with the DOC data in Figure 6.2, where the resin is 90% cured at this stage. The net strain due to cure shrinkage is about 255 με. It has been previously reported [Johnston 2001] that the observed strain change is about 40 με. However, the direct measurements of specific volume changes in AS4-3501 pre-preg have shown shrinkage as high as 1.5% [Russell 1993].

In the last stage (S4), further shrinkage can be seen due to thermal contraction when the composite panel, aluminum pulley, and optical fiber are cooled. It is not clear why the strain response lags behind the thermal profile. According to thermocouple readings in Figure 6.6, the cooling occurs at two rates – the second one is faster (3.2°C/min) than the first (0.95°C/min). Therefore, the rate of contraction due to cooling from 177°C to room temperature at the average of 2.1°C/min is 69.8 με/min or 33.2 με/min. If we consider the CTEs of the aluminum pulley and optical fiber, the net strain due to thermal contraction of the composite panel would be about – 0.05 με/°C, which is very close to the longitudinal CTE of cured AS4-3501 composite [Crasto and Kim 1993].

From the results so far, there is evidence that the 15 cm spatial resolution distributed Brillouin sensing system is able to detect the relatively small contraction in the matrix resin between the onset of gelation and vitrification stages.

6.4 Summary

The distributed Brillouin scattering technique has been successfully applied to monitor the strain and temperature variation during the curing process of carbon fiber and epoxy composite materials. The optical fiber was embedded within the mid-ply of the16-ply panels to measure in-situ temperature and in-plane strain simultaneously. A signal processing and data analysis method was developed to generate the net strain profiles at different stages of the cure process. The work has demonstrated that a 15-cm spatial resolution is capable to detect in-situ the relatively small strains associated with resin curing shrinkage during gelation and vitrification.

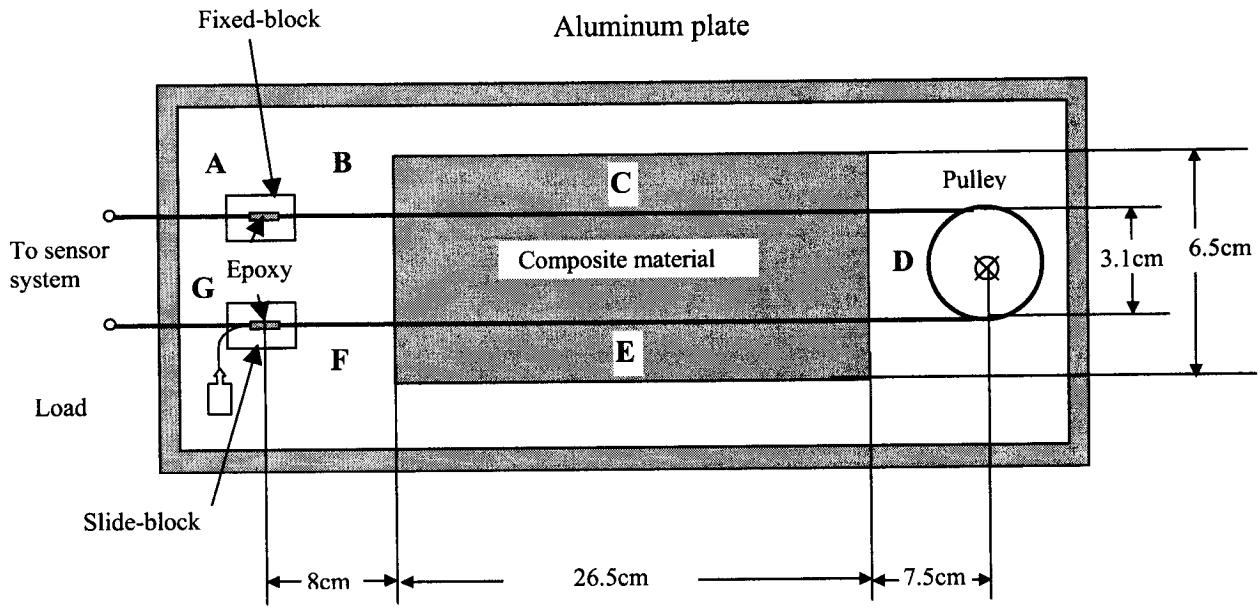

Figure 6.1 Layout of the optical fiber embedded in the composite material

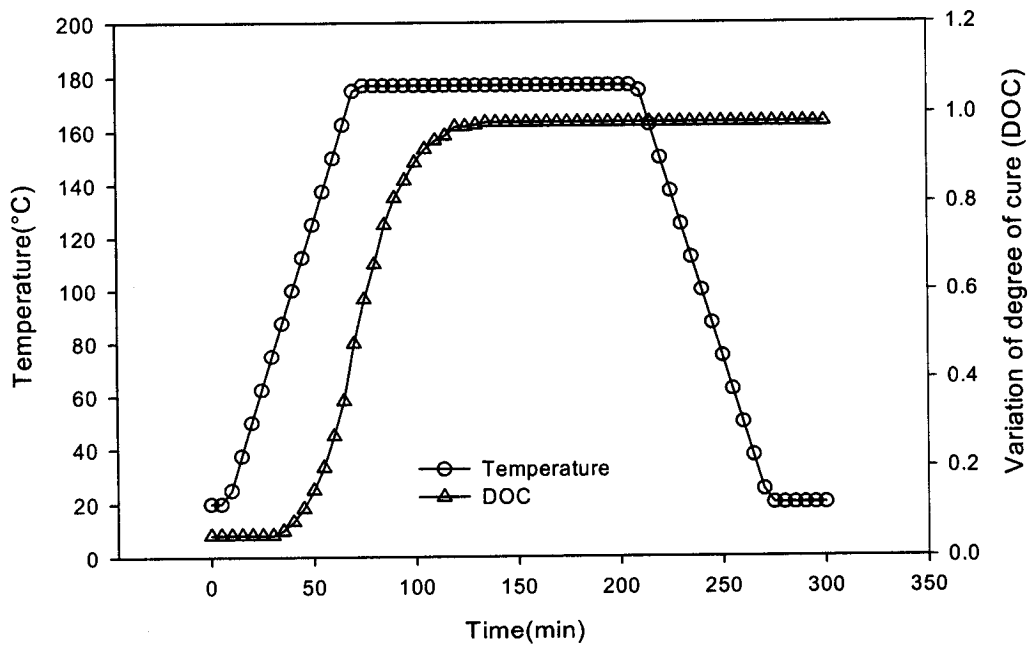

Figure 6.2 The degree of cure (DOC) as a function of time

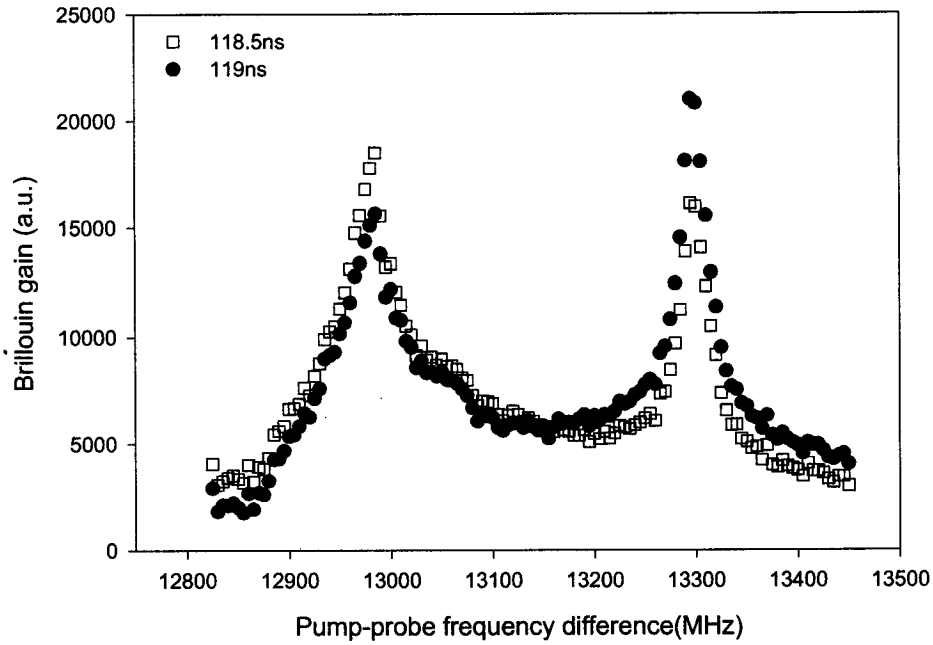

Figure 6.3 Comparison of Brillouin gain spectra at 118.5 ns (section A) and 119 ns (section B)

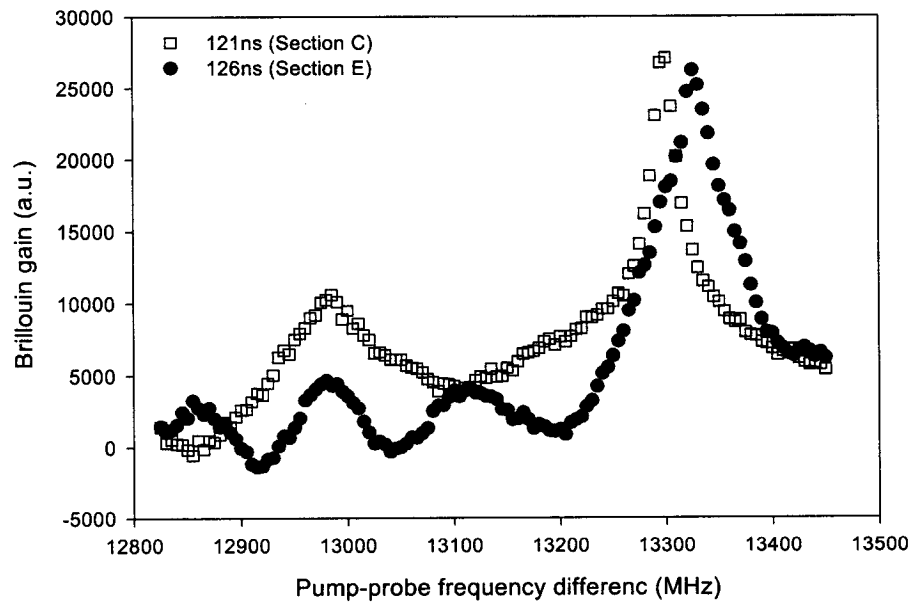

Figure 6.4 Comparison of Brillouin gain spectra for 121 ns (section C) and 126 ns (section E) of the optical fiber.

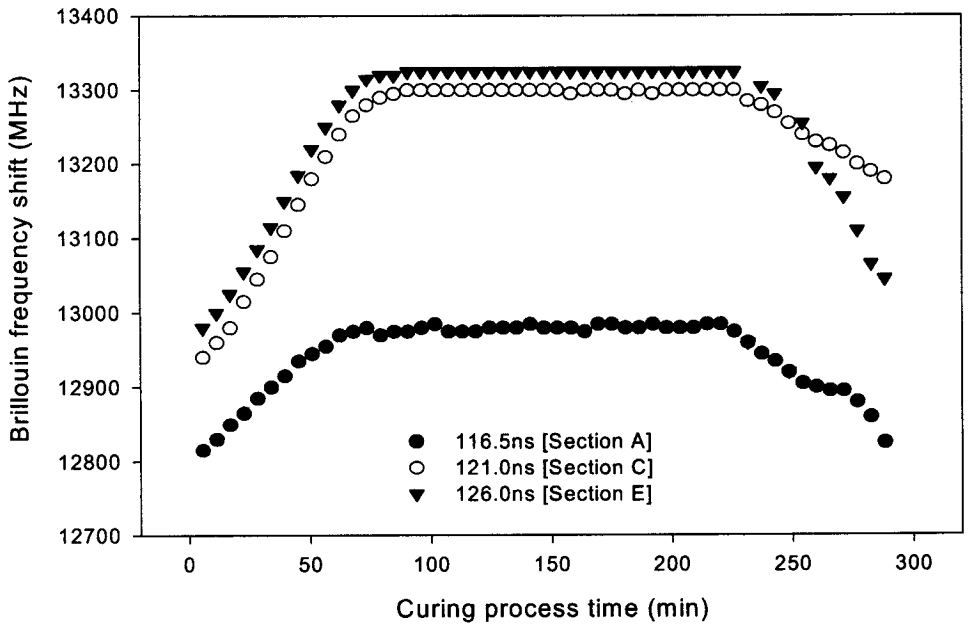

Figure 6.5 The apparent Brillouin frequency profiles for sections A, C, and E of the optical fiber during the cure process.

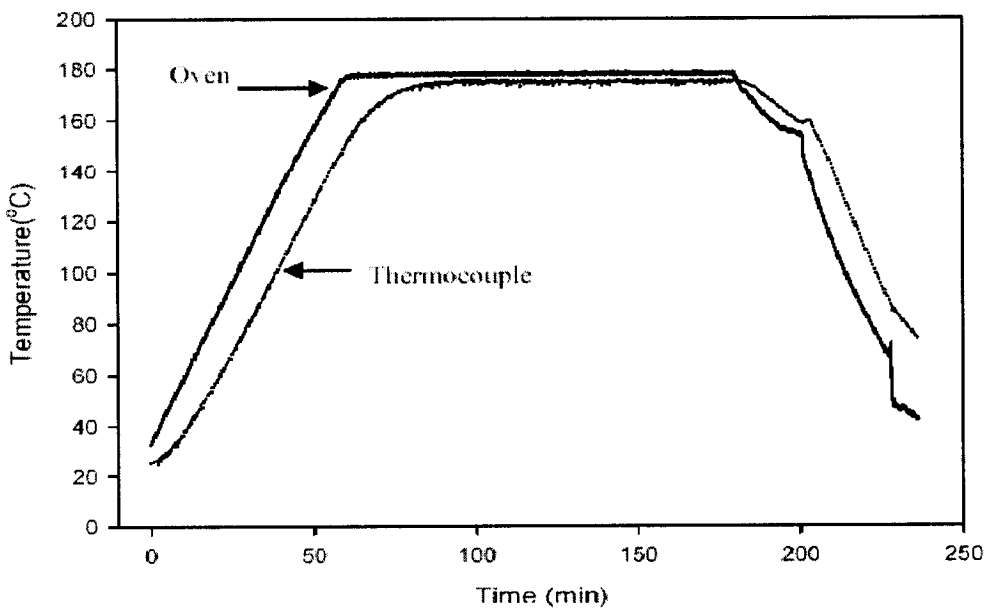

Figure 6.6 The lag between the composite (thermocouple) and oven temperature.

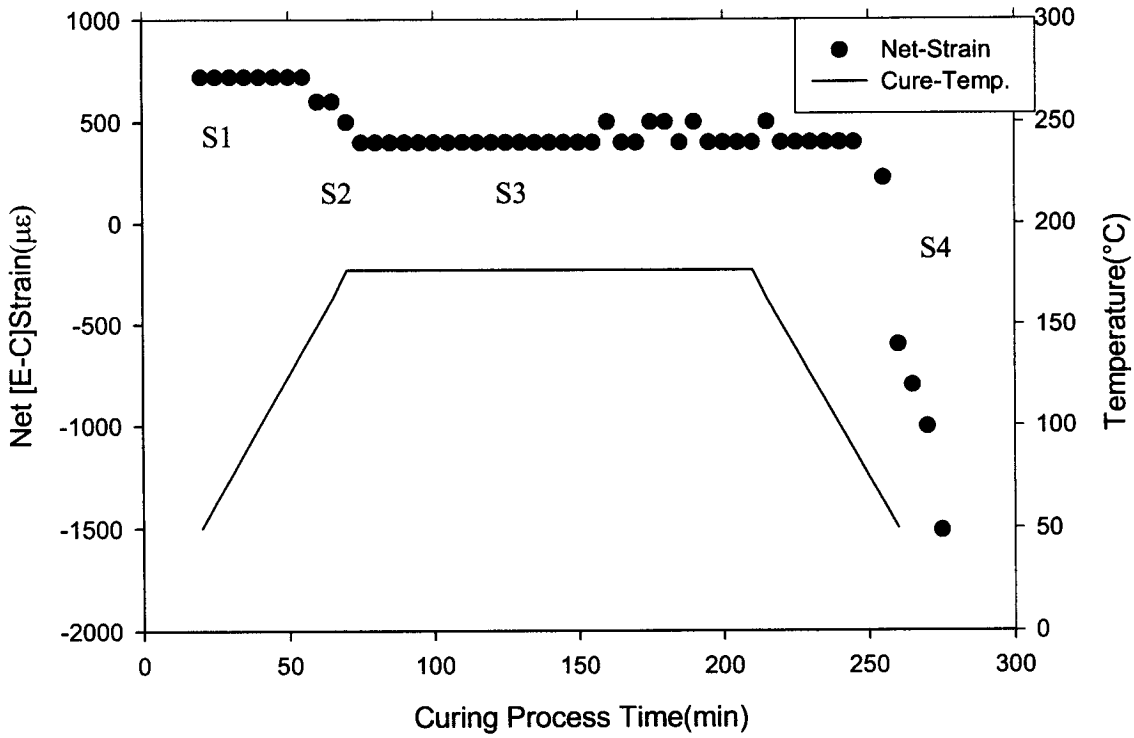

Figure 6.7 The net in-plane strain profile (E through C) due to the curing of the AS4-3501 composite panel.

Chapter 7

Field Application of Distributed Brillouin Sensor

This chapter introduces two field tests with our distributed Brillouin sensing system. One is strain and temperature monitoring of a nuclear containment structure [Zeng et al. 2002a]. The other is temperature compensated strain measurement of the load test on the Rollinsford Bridge [Zeng et al. 2002b].

7.1 Strain and Temperature Monitoring of a Concrete Structure

The purpose of this field test was to monitor strains (compression and tension) in the concrete and fiber reinforced polymer (FRP) layer due to the environmental impacts, such as temperature, wind and sun radiation. The limitation with both temperature and strain sensing fibers was that the strain induced by sun radiation was different due to the different jackets for protecting fibers. This could introduce the strain measurement uncertainty.

The choice of the epoxy to adhere the sensing and temperature fibers to concrete and /or FRP, were essential to ensure the accurate strain reading from the structures rather than the strain induced by the epoxy or polymers. Since the repairing of the concrete structure was for the upper part of the nuclear reactor wall, a thin FRP sheet was applied to the concrete surface, we attached our sensing and temperature fibers on the surface of the FRP with PL Premium® Polyurethane Construction Adhesive.

The temperature and strain were measured for two days, the first day was from 8am to 2pm; the second day was from 3pm to 8pm. The temperature of every hour within 10km was obtained from Environmental Canada. Two peaks were found during 1st day with 4°C temperature variation. Our temperature sensing fiber had confirmed this at a few locations of

the concrete structure. The average strain measurement accuracy was ±50με, which was measured by standard deviation from measurement data and best Brillouin frequency fit.

7.1.1 Test preparation

Since a sensing fiber would respond to changes in both strain and temperature, two kinds of sensing fibers were used to detect temperature and strain. One fiber (cable fiber) was attached to the structure isolated from strain, and it only senses the temperature. The cable protection applied to this fiber would not respond to the strain (or with minimized change). The other (bare fiber) was attached to the structure to sense the strain with small pretension applied to the fiber. The Brillouin frequency obtained from bare fiber is subtracted from that of cable fiber (corresponding to the temperature effect) to get the strain in the bare fiber at every position.

Both the strain and temperature fibers were SMF-28 single mode fiber. The temperature sensor is a 3mm jacketed fiber. In the jacket, there were 12 bare fibers that made this cable very strong. This communication cable was designed to resist the strain induced by the environmental effect. Here we used it to isolate the strain impact to this fiber for temperature monitoring. SMF-28 fiber is widely used in the telecommunications industry; it is inexpensive and readily available.

Figure 7.1 shows the concrete structure of the nuclear reactor wall. It is a cylinder shape approximately 60 meters in height and 40.7 meters in outer-diameter. The perimeter is 128m. The sensing fibers were installed near the top of the cylinder. On the surface of the concrete, a FRP protective layer was pre-attached. Our sensing fibers were glued on the surface of the protective layer. In order to show the impact of the sun radiation to the temperature and strain reading we divided the sensing region into 8 sections, every 16 meters as a section as showed in Figure 7.2. Both bare fibers for stain sensing and temperature sensing were fully covered by epoxy. The temperature sensing fiber remains loose in the cable as shown in Figure 7.3.

The start points of the sensing fibers are in the west marked with "8 m" in Figure 7.2. The three sensing fibers are cascaded and connected with 700m lead fibers. The lead fiber passed through the special hose into the building and down to the ground level. At the ground level,

lead fiber was connected to a nearby building where the Brillouin sensing system is located. The total length of the optical fiber is about 1100 meters.

Before the on-site test, the strain and thermal coefficients of the sensing fibers were calibrated in the laboratory. The results are shown in Figure 7.4 and Figure 7.5. The average values the coefficients are listed in Table 7.1

Table 7.1. Calibration of SMF-28 sensing fiber

	Single mode fiber	3mm Cable fiber
Strain coefficient (με/MHz)	17.09	N/A
Thermal coefficient (MHz/°C)	1.221	1.264

7.1.2 Experimental results and Discussion

The strain and temperature measurement had been carried out continuously from 8AM to 2PM in the field. It was a cloudy/raining day on September 21, 2001. During that period of time, the temperature variation was 4.4 °C. One complete measurement took about 5 minutes. The measurement was taken every 20 minutes.

Figure 7.6 shows Brillouin shifts in the strain fiber-1 and the temperature fiber along the whole hoop. The Brillouin frequency differences between two testing results at 12:00AM and 2:00PM corresponded with air temperature difference of 1.4 °C. The Brillouin shifts of the strain fiber represent the strain levels of the concrete structure, while that of the temperature reference fiber are proportional to the temperature variation. However, Figure 7.6 shows a maximum variation with position of ~ 15 MHz that would correspond to a temperature variation of ~ 13°C. There is an order of magnitude difference. The possible reasons are: 1) The air temperature value obtained from the local meteorological observatory of a nearby city was 10km away, it is 1m above the ground, while the concrete structure we measured the temperature is 50m above the ground, also what we measured is the concrete temperature; 2) The temperature calibration was done with the loose fibers, strictly speaking, they are not loose in the cable (there were some pre-tension and stress with them). 3)

Different materials have different thermal expansion coefficients, for examples the expansion coefficient of epoxy used in this test is 7.5 times larger than that of optical fibers.

Figure 7.7 shows the comparison of the air temperature and the temperature changes of the eight sections on the nuclear reactor wall in six hours. The temperature distributions were measured with the temperature reference fiber. The weather and air temperature records of the nearby city (10 km apart) were obtained from the local meteorological observatory. Both curves showed similar tendency.

The differences between the air temperature and temperature distribution of the concrete structure are mainly due to the weather and geographic environment that impacted the temperature distribution in different regions of the concrete structure. For different regions of the concrete building, the temperature variation was different. Some regions have more rain than the other due to the direction and strength of the wind. In addition, the St. Lawrence River is to the north, a huge plain is to the west, and factory buildings to the east of the tower. Approximately 50-meters above the ground where the sensing fiber was installed, the directions and strength of the wind changed frequently. The directions and velocities of the wind in the measurement region are shown in Table 7.2. It's obvious that the temperatures around the tower should be different in such a complex environment.

Table 7.2. The directions and velocities of wind

Time (o'clock)	8:00	9:00	10:00	11:00	12:00	13:00	14:00
Direction	S	S	SSE	SSE	ENE	ENE	ENE
Velocity (km/h)	4	11	19	6	2	11	5

The continuous six hours strain variations are shown in Figure 7.8. Comparing Figure 7.7 and Figure 7.8, the temperature and the absolute value of strain tends to give the same changing trend in most case. Some unusual segments, such as at the Section7, came from the complex local conditions. The possible reasons were: 1). Because of the concrete, Polyurethane Construction Adhesive, FRP, and silica fiber have their own thermal expansion coefficients, which are 10μm/°C, 30μm/°C, 45μm/°C, and 4μm/°C (Figure 7.9), the multi-material structure made the analysis more complicated. 2). In order to measure strain, the

fiber must be tightly attached to the concrete surface. A certain amount of pre-strain was introduced during the installation that was not uniformly distributed along the fiber. 3). As the temperature of the environment altered, the temperature fiber may have not responded immediately. The 3mm jacket of the cable fiber and the layer of epoxy adhesives caused a reasonable delay.

Negative strain values are showed in Figure 7.8. The underlying physical process is a competition between participating members. As the temperature changes, materials tend to expand or contract depending on the specific material properties. When the optical fiber is used for physical sensing, the results tend to reflect the most dominant process, i.e. the response of the material with the highest temperature coefficient of expansion. Furthermore, expansion of materials can occur in all directions so we must distinguish between forces in an axial direction and those in non-axial directions. When the net force stretches the fiber along the axial direction (as temperature rises), we say the fiber is under "tension". The fiber is under "compression" when the fiber is shortened (temperature goes down) due to the axial forces. However, transverse forces can also occur as shown in Figure 7.9, whereby the expansion of materials "squeezes" the fiber's cross-section without expanding the fiber along its axial length. This can especially occur when the fiber is mounted continuously with rigid glue. There are four forces acting on the surface of the optical fiber: a upward expansion force of the fiber and downward compressive force of the epoxy that acted on the top surface of the fiber; while an upward compressive force of FRP and a downward stretch force of the fiber that acted on the bottom surface of the fiber. In this case, the fiber has no room to expand in any direction, therefore an induced stress occurs along the fiber's cross-section. Thus, the silicon oxide molecules are being compressed together so the Brillouin frequency is downshifted in a similar fashion as axial compression. Hence when temperature increases around 10 – 11 o'clock, the measured value has been increased in the form of stress.

The standard errors [Appendix] of the strain measurement are 44.5 με for strain fiber1 and 51.5 με for stain fiber-2 while that of Brillouin shift measurement are 2.6 MHz for strain fiber1 and 3.0 MHz for strain fiber-2. For a large structure monitoring with very small spatial resolution (18cm), it is considered a good test result comparing to Kurashima and coworkers'

study that reported a ±60με strain accuracy and 1m spatial resolution [Kurashima et al. 1997].

We are planning to go back the site to make another strain test, study the long-term changes and make the comparison of the current strain measurement with the future test results.

7.1.3 Summary

When the distributed Brillouin scattering sensor is used for long-term strain monitoring in the field, the temperature variation as a function of time and position must be measured as a reference, so that the temperature contribution to Brillouin frequency can be subtracted from the strain distribution measurement.

The choice of the glue for the bond agent between the sensing fiber and the concrete structure is crucial for accurate strain reading of FRP/concrete. The thermal expansion coefficient of the glue should be smaller than the FRP/concrete, so that the concrete structure rather than the glue contributes the major strain variations.

7.2 Temperature Compensated Strain Measurement of the Load Test on the Rollinsford Bridge

This section reports the temperature compensated strain measurement during the load testing of the Rollinsford Bridge, Rollinsford NH with the distributed Brillouin sensing system [Zeng et al. 2002b].

The old bridge in Rollinsford, New Hampshire (shown in Figure 7.10), built in the 1930's, carried two lanes of traffic a distance of 52.4 m over four spans. As time passed, the supporting steel bars and girders experienced significant amounts of corrosion, thus degrading the structural integrity of the bridge to dangerous levels while the traffic loads continued to increase over the design loads of the 1930's. Consequently, in Dec. 2000, the New Hampshire Department of Transportation (NHDOT) replaced the structure with a new 33.5 m single span

concrete bridge (Figure 7.10). To minimize salt-spray corrosion, New England Bulb Tee (NEBT) concrete girders were chosen instead of steel girders in the new bridge, and pieces of corrosion resistant carbon fiber reinforced polymeric (CFRP) grid were placed vertically on top of girders to act as a shear connection to the concrete deck and to ultimately ensure truly "steel-free" deck.

The new Rollinsford Bridge is the first bridge in the US using CFRP composite grids in the bridge deck and the first bridge in the world being reinforced entirely with this material in the bridge deck. Since this is the first CFRP grids bridge deck, it is very important to monitor the strain distribution in the bridge deck under loadings. This study demonstrates the strain measurement of the CFRP bridge deck during load testing using distributed fiber optic sensing based on Brillouin scattering.

CFRP is a new material for the civil engineering industry, the strain monitoring of long and short-term data on the materials of FRP and high performance concrete (HPC) will provide the guide for future bridge instrumentation. Until now, no comprehensive long-term monitoring system and rational analytical predictive methods exist for structures. Hence the development of monitoring methods and analytical tools is essential to answer those questions related to the long and short-term performance of civil structures.

In this experiment three SMF-28 single mode optical fibers with 900 μm buffer jacket were used to measure the strain variations on the deck with and without loading. Two of them were bonded with high strength epoxy paste adhesive on the bottom surface of the CFRP composite grids embedded in the high performance concrete (HPC). The bottom surface was chosen to glue the fiber to protect the fiber from the damage during the concrete pouring process. The third fiber was attached to the bottom surfaces of the deck and girders using two methods of fiber installation: 1) the fiber was continuously glued along the surface in sensing regions proving nonuniform strain within spatial resolution; 2) fibers glued at 15cm providing uniform strain measurement along gauge length.

The glue choice is important in this work. There are three requirements: 1) it can durably connect both optical fiber and concrete; 2) no chemical reaction takes place between the glue, optical fiber, and concrete; 3) it has about 30 minutes consolidating time. The connection may be destroyed for a long consolidating time due to the spread of the glue. Through testing in the

lab, we chose a construction epoxy with a thermal expansion coefficient of 30μm/°C. However, different thermal expansion coefficient of concrete (10μm/°C), epoxy (30μm/°C), and optical fiber (4μm/°C) may induce a strain reading error that is not really subjected by concrete or FRP grid.

The strain was monitored continuously along different bridge deck positions. Temperature compensation was obtained with loose fibers between glued fiber sections and lead fibers. Compression (negative strain) and tension (positive strain) were observed on upper and lower CFRP grids where truck wheels were located.

Brillouin scattering based distributed sensor can be used for measuring temperature and strain related to the behavior of the bridge, and as a health monitoring system through real-time, remote monitoring of the performance of the bridge during installation are providing useful information about the steel-free deck design and gathering information on fibers installation into a concrete deck for future field tests.

7.2.1 Pre-test slab experiments

Before the field test, a test specimen of the bridge deck (constructed at University of New Hampshire) was investigated under different loads in the lab to compare the capability of strain measurements between distributed Brillouin sensor and conventional strain gauges [Brown et al 2000]. The distributed sensor measurements from the single point-loading pattern on the test slab show a good agreement with the test results from the conventional strain gauges installed in the deck slab. Table 7.3 summarised the comparison of strain values from the distributed Brillouin sensor and conventional gauges for both positive and negative moment regions. Those differences between the test results of the distributed Brillouin sensor and conventional gauges fall within typical experimental error ranges and confirm the readings obtained from the distributed sensor.

Table 7.3 Comparison of the strain readings of Brillouin sensor and conventional gauges for one-point loading case

	Positive Moment Region			Negative Moment Region		
Loading	Gauge	Brillouin	Variance	Gauge	Brillouin	Variance
71.1kN	-210με	-201με	5%	56με	50με	11%
88.9kN	-362με	-313με	14%	70με	75με	7%

7.2.2 Fiber installation in field

In the field test, we need to consider temperature compensation. In the past, we used two fibers in parallel on the structure, one as the temperature reference in which fiber is protected with a large plastic tube and the strain sensing fiber is glued to the structure, or using the temperature fiber attached to the surface without glue. The problems associated to these methods are: 1) when the structure is in the field it is hard to make large diameter tubing (2-3 mm) of 10 m long to cover the sensing region in parallel, as they weaken the strength of the concrete and the bonding between the structure (FRP) and material (concrete); 2) both temperature and strain fiber must be well protected and glued on the CFRP grids before the concrete is poured. After the concrete is poured, both temperature and strain fibers are subjected to the different residual strains, which gives strain measurement error; 3) the glue usually has thermal expansion coefficients 3 ~ 8 time larger than the concrete and optical fibers. Hence the measured strain is the combination of glue and structure/material variation.

To solve these problems in this project we introduced (1) lead fiber sections as the temperature reference. Lead fibers were kept free of strain by the PVC pipe from damages in concrete deck and being fixed by the tapes outside bridge deck. Since lead and sensing fibers are in the same environment conditions, we can subtract the impact of temperatures from the strain sensing fiber to get the net strain. The structural strain measurements with Brillouin scattering based distributed sensor have shown the compression (negative value) for the upper CFRP grid, and tension for the bottom CFRP grid as expected for a concrete beam subjected one point load in the area that fiber sensor covered; (2) the fiber was glued at every spatial resolution point (15 cm) to increase the strain accuracy.

For the material strain measurement, the fiber was glued to the bottom surface of the bridge between girders and bays. We have tried to use as little glue as possible to eliminate the glue impact on the strain measurement. Temperature reference was provided by a piece of lead fiber that was not glued, but point fixed by tapes.

For monitoring the performance of the bridge deck, three sensing fiber loops were installed at different locations along the bridge using SMF-28 single mode optical fibers with 900 μm buffer jacket. Two loops (Loop A and Loop B) were embedded within the bridge deck, and the third loop (Loop C) was attached to the bottom surface of the bridge deck and girders. The embedded fiber loops, Loop A and Loop B, were bonded with high strength epoxy paste adhesive to the bottom surface of the CFRP composite grids located at mid-span of the bridge. Loop A was placed under the bottom grid "B" (Figure 7.11) while Loop B was located at the bottom surface of the top grid "G" (Figure 7.12), e.g. near the road surface.

Four SMF-28 E207090 single mode fibers were introduced as lead fibers transmitting optical signal from the bridge deck to the distributed Brillouin sensing system. They were loose fibers spliced with sensing fibers and then went through a PVC conduit lead to the outlet holding box under the bridge. These fibers were used as temperature reference. Figure 7.13 shows the bottom grid and PVC conduit.

Fiber Loop C was attached to bottom surfaces of the bridge deck and girders after the reconstruction was completed (Figure 7.14), and was divided into nine fiber sections as shown in Figure 7.15 and Table 7.4, A, B, C, D, E and F parts, all of them were glued on the concrete surfaces with different sensing lengths. Except A~F sections, all other parts were kept loose as lead fiber and temperature sensing reference. Here A, C, and E were bonded along Girder 3, 4, and 5 respectively. Regions B and D were attached on bottom surface of the Bays 3 and 4 in the cross direction of bridge deck. Sections A and C were glued every 15 cm, while sections B, D, E, and F were glued continuously to the concrete. The strain was monitored at different positions along bridge deck at various times.

Table 7.4. Size and locations of LoopC installed on the bottom surface of the bridge.

Section	Length (m)	Location (m)	Glued method
A	3.568	Girder3 (37.50--41.16)	Every 15 cm
B	0.940	Bay3 (43.73--44.80)	Continuous
C	3.568	Girder4 (51.05--54.71)	Every 15 cm
D	0.990	Bay4 (57.27--58.34)	Continuous
E	1.829	Girder5 (60.90--62.74)	Continuous
F	0.254 (each)	---	Continuous

7.2.3 Load test and sensing result analysis

The load test was conducted during August 2001 in Rollinsford NH. A 333.4 KN three-axle truck with 102kN on the front axle, and 116 KN per each back axle, was placed at predetermined locations near the mid-span of the bridge shown in Figure 7.16 to test the deck response. The strain distribution of the bridge deck as a function of loading position and time were monitored continuously with a 15 cm spatial resolution.

Brillouin frequency shifts on temperature were measured along a piece of lead fiber. The Brillouin frequency spectrum was scanned at 10MHz steps. For all strained fiber sections (three loops and attached fiber section), Brillouin frequencies were measured and temperature induced Brillouin frequency shifts were deducted from the neighboring unstrained fiber sections.

Figure 7.15 (Loop C - attached), Figure 7.17 (Loop A - embedded), and Figure 7.18 (Loop B - embedded) show the layouts of three optical sensing fiber loops on the bridge and locations of the dump truck when the load tests were applied. The dump truck was parked in positions that the driver's side front tire was placed 0.381m from the bridge centerline on the top of bay4 for Loop A and 0.559m from the bridge centerline on the top of girder4 for Loop B. There were two parking positions for Loop C: one on the top of bay4 and the other on girder5. The distance from the parking positions to the bridge centerline was 0.432m for both positions.

Figure 7.19 (Loop A - bottom CFRP grid) and Figure 7.20 (Loop B – top CFRP grid) show the relative strain changes versus positions along the optical fiber length. It is clear for the top

grid when the loading (truck) was applied; the negative strains (compression) have been measured in Figure 7.20 compared to no truck case at 22m and 31m position. As shown in Figure 7.18 that the front wheel crosses the left line of the sensing fiber Loop B, this results in the large negative compression at 22m in Figure 7.20. This is a narrow and sharp peak compared to the tension in Figure 7.19, as the driver's front wheel is located on the girder 4, the force is limited by the strong support from the girder 4. The back left wheel of the truck induces the compression at around 31m; 7m distance corresponds to the position around PVC pipe for the lead fiber. The PVC tubing provides some support for the fiber, which released the compression on the fiber at this position; hence the compression is much smaller than the strain at 22m. The right wheels are outside of the sensing Loop B.

On the Figure 7.19 we have seen positive strain (tension), as the fiber Loop A is glued at the bottom CFRP grid, as expected with loading the bottom grid was subjected to the tension. The two big tension sections are located at 22-23m and 25-26m. When we look at Figure 7.17 we see the left front wheel (driver side) crosses the left and right lines of Loop A. The distance is around 3m, which matches Figure 7.19. The tension has been spread over a large area, the broader peaks are observed vs. narrow peaks in the girder support case (Figure 7.20), as the front wheel is sitting on the Bay4, which cannot provide as strong support as the girders. Although the maximum strain (~140με) is seen in the compression peaks, the rest of the area in Figure 7.20 has very little strain (< ±20με), while in the tension case, the overall strain (< 80με along 6 m of the sensing length for Loop A from 21-27m) is large across the whole sensing loop due to the weaker support on the bay area.

In Figure 7.21 we converted Brillouin frequency shift to the strain difference along the optical sensing fiber Loop C when the driver's side front wheel of the dump truck was sitting on the girder and bay areas. The strain changes have been corrected for temperature induced frequency shifts. We took the average Brillouin shift of the lead fiber sections and then subtracted them from the Brillouin frequency shift in strain fiber sections A-E, to arrive at the net strain variation.

As explained in the fiber installation section, sections A and C were glued at every 15cm (equivalent to the spatial resolution); sections B, D and E were glued continuously. The section lengths are given in Table 7.4. In Figure 7.21 the solid lines are the results for the

driver's side front wheel of the dump truck on the Bay4 and the dot lines are that on the Girder5. Sections C, D and E correspond to area of the girder 5 and bay 4. It is found that the tension for the load located on the top of the girder is smaller than the loading truck located on the top of the bay. Apparently the girder5 provides stronger support for the truck wheel than the bay4. The force is more spread for the bay area than the girder area. The strain is more localized for the wheel at the girder position. Therefore the strain value is smaller for the girder load case. The detailed analysis is as follow:

1. For region A (girder3): as expected no difference was observed for two truck positions due to large distance between girder3 and loading point.
2. For region B (bay 3): small strain difference was observed as both truck positions did not have tires on the top of bay 3. This region corresponds the lower strain sections for two-point loading (two front wheels are equivalent to two-point loading) [Zeng et al. 2002] for both truck positions.
3. Region C (girder4): huge spikes appeared. Normally when the strain changes rapidly the signal processing will give larger error. The solid line (front wheel on Bay4) shows higher tension at the bottom bridge. This agrees with two points loading on the concrete beam that top part of the concrete beam gives the compression and the bottom part gives tension (as presented in Chapter 5). The dotted line is equivalent to the low-tension strain of the loading point with high strain gradient. As we know high strain gradient results in bigger error, this is a problem for both point and distributed strain-sensing system. Hence the spikes appeared.
4. Region D (bay4): some strain difference was observed, at the position equivalent to one of the two loading points for the same weight in both truck positions. However, the truck positions for two cases were not exactly symmetric relative to girder 4 and girder 5. Hence the strain is different.
5. Region E (girder5): small strain difference was observed. For dotted line it is at one of two loading points, for solid line it is close to one of two loading points. The tension trend is seen and the difference is small. The sensing section in region E is half of the length in region C.

The large "strain" differences between the strained and unstrained fibers may be due to temperature differences among different lead fiber sections or strain sensing sections. The measurement was taken in August when the temperature was varying between 35-40°C over the four hours between measurements. When we took average Brillouin shift of the lead fiber regions to compensate the temperature influence for Brillouin shifts at each strain sections, it induced errors.

The standard errors of the strain measurement are 22με (equivalent to1.3MHz Brillouin frequency shift) for the sensing fiber Loop A, 28με (equivalent to1.6MHz Brillouin frequency shift) for Loop B, and 29με (equivalent to 1.9MHz Brillouin frequency shift) for Loop C. Those values came from the calculations of the standard deviations between the fitting experiment points to the theoretical profile.

7.2.4 summary

The distributed Brillouin sensing system provides temperature compensated strain measurement during load testing of the Rollinsford Bridge. It can distinguish the complicated strain distribution in details on a real bridge. For all three optical fiber loops, the maximum strain values observed during load test were 80-200 με, which is mush lower (< 2%) than the ultimate strain of FRP material (NEFMAC Technical Leaflet 2000). Through signal processing the strain measurement has been compensated for the temperature errors. The strain resolution of ±25με (μm/m) and the spatial resolution of 15cm were achieved.

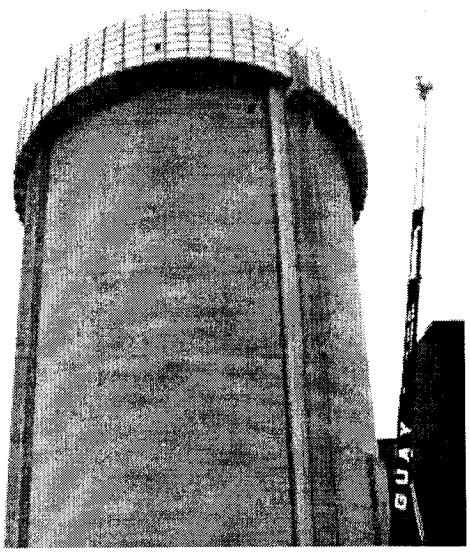

Figure 7.1 The nuclear containment structure

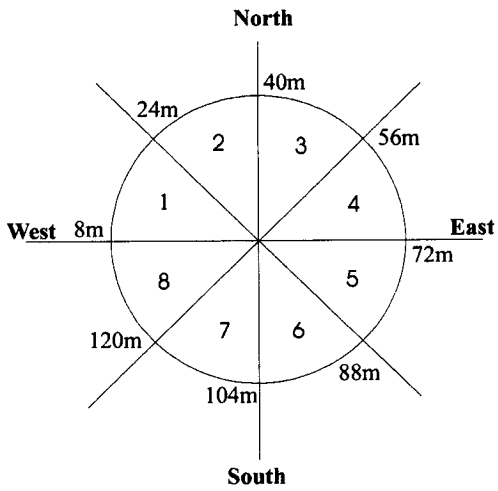

Figure 7.2: Section of the sensing region

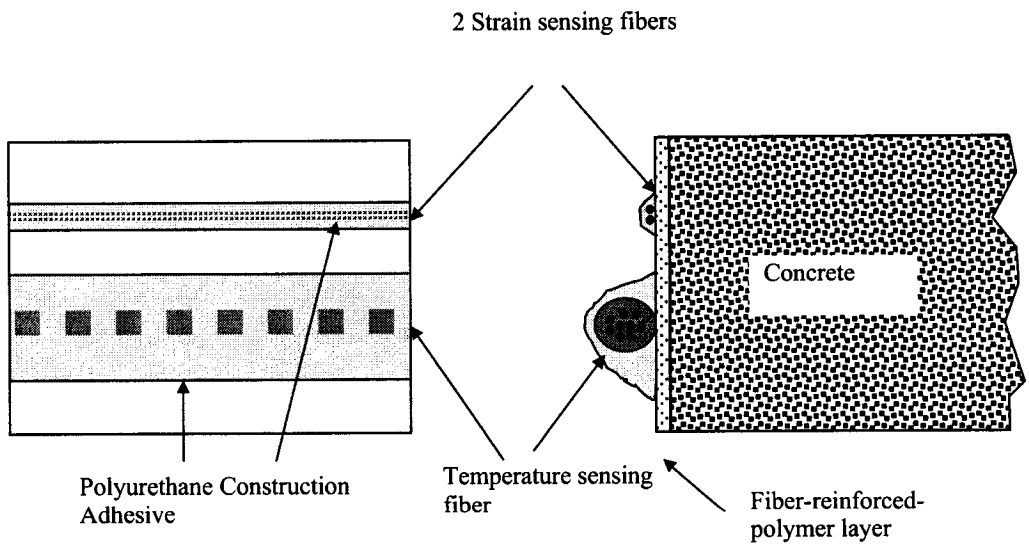

Figure 7.3 A close look of sensing fiber installation on the structure of concrete

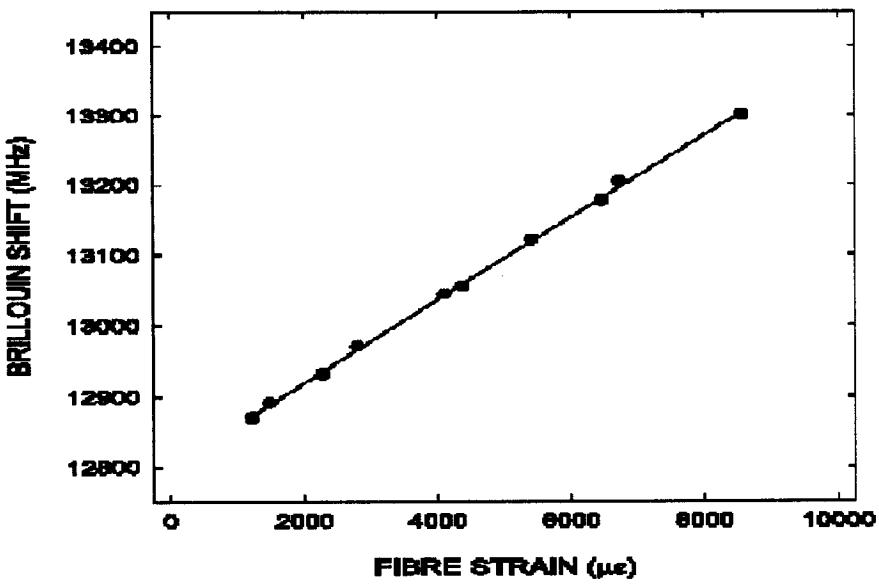

Figure 7.4 Strain-Brillouin frequency calibration for SMF-28 single mode fiber illustrates linear relation between two parameters.

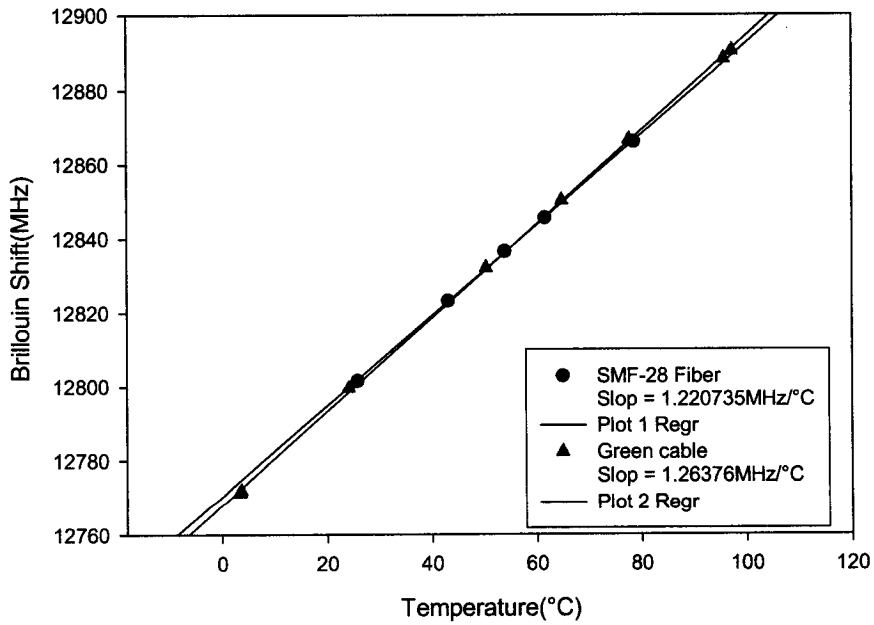

Figure 7.5 Temperature-Brillouin frequency calibrations for SMF-28 single mode fiber and cable fiber show linear relationship between the two variables.

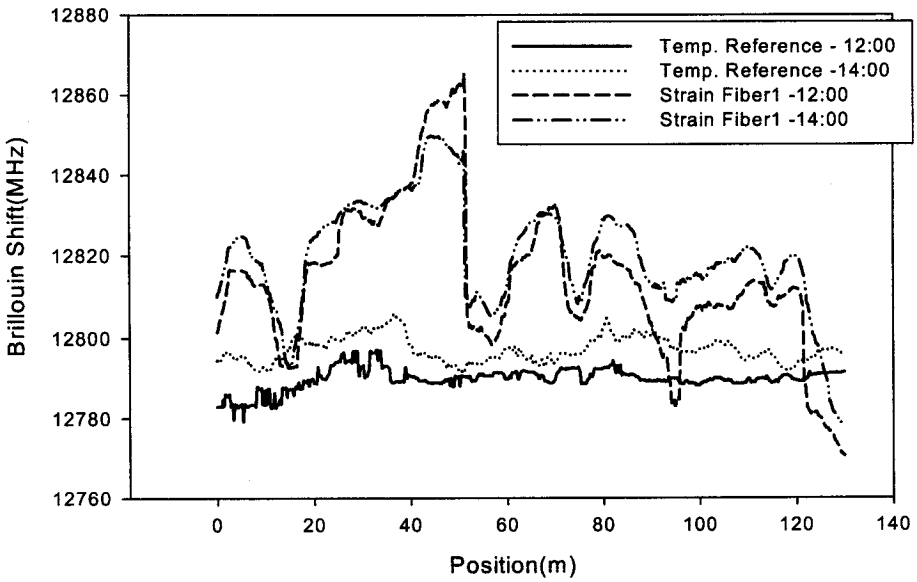

Figure 7.6 Comparison of Brillouin shift distribution measured with the temperature reference fiber and the strain sensing fiber.

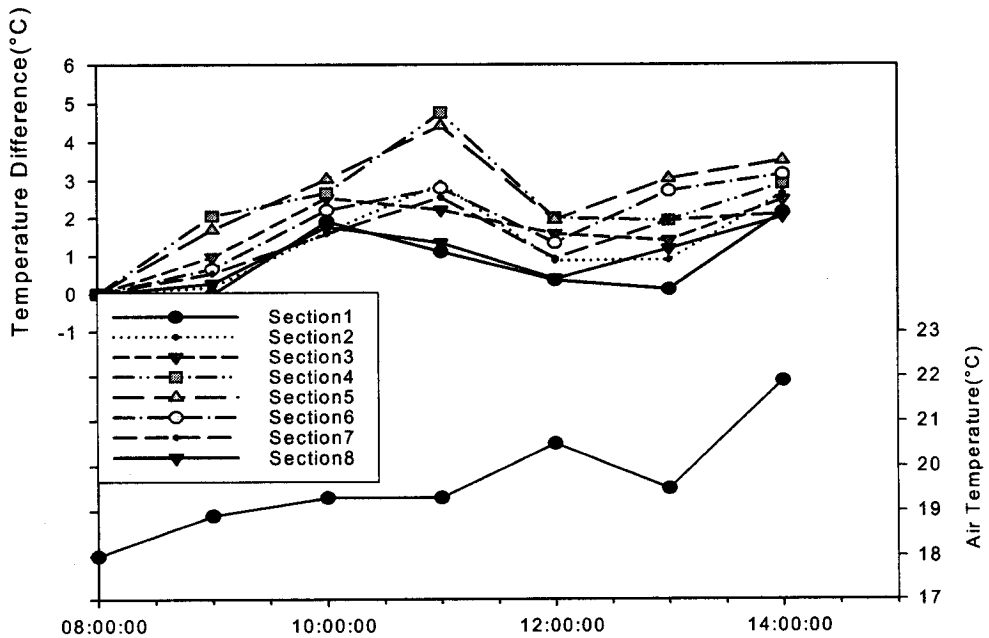

Figure 7.7 Comparison of air temperature and relative temperature change of the containment structure of the nuclear generator in six hours.

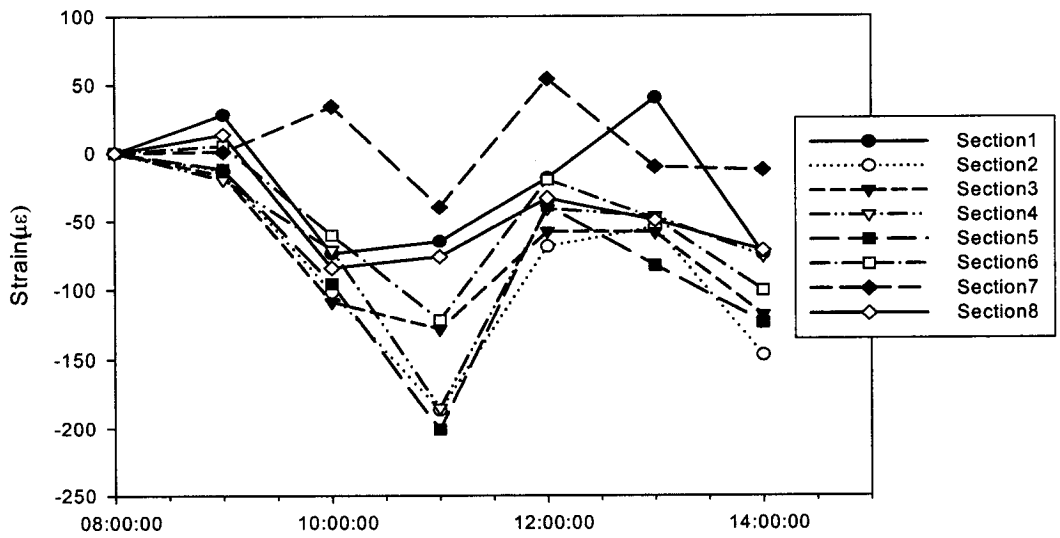

Figure 7.8 Relative strain changes in six hours for eight sections of the nuclear generator wall.

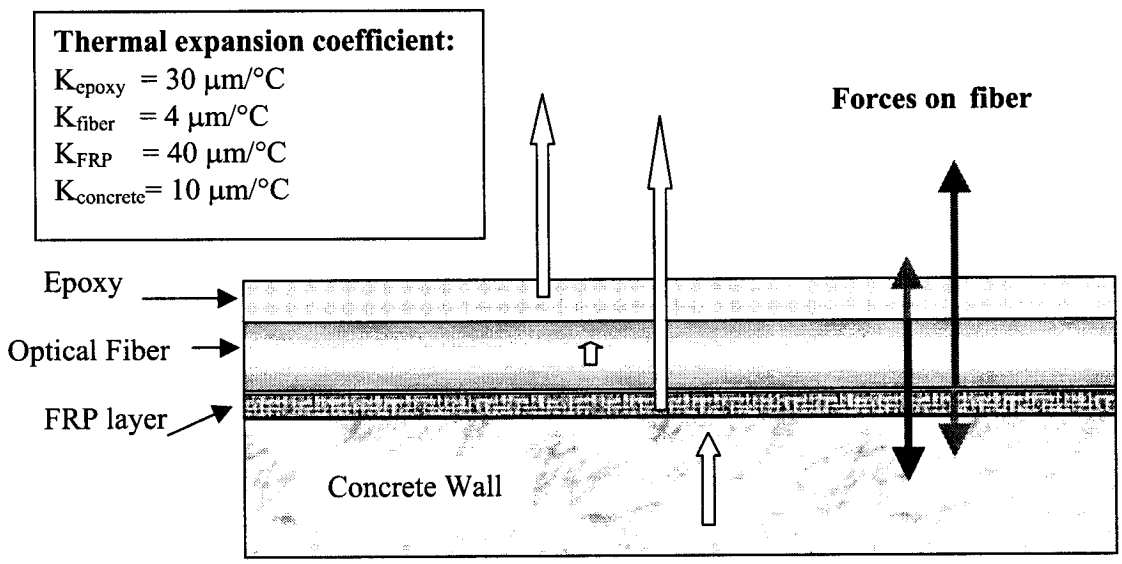

Figure 7.9 There are different thermal expansion coefficients for different materials. They are 10 μm/°C for concrete, 40μm/°C for FRP layer, 30 μm/°C for epoxy, and 4 μm/°C for optical fiber. Four forces acted on the optical fiber, when the temperature changed.

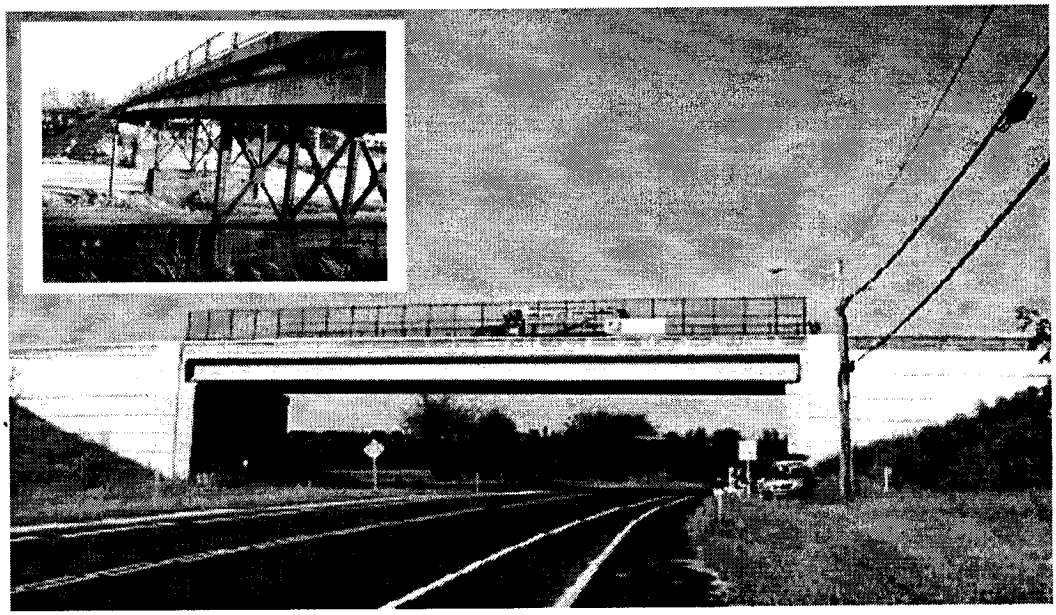

Figure 7.10 The new Rollinsford Bridge was opened to traffic in Dec. 2000. It's a 33.5 m single span concrete bridge using HPC in the NEBT concrete girders, and both CFRP grids and HPC in the deck. The old Rollinsford Bridge, built in the 1930's, was a 4 span, 52.4m long, two-lane steel girders and steel-reinforced concrete deck bridge.

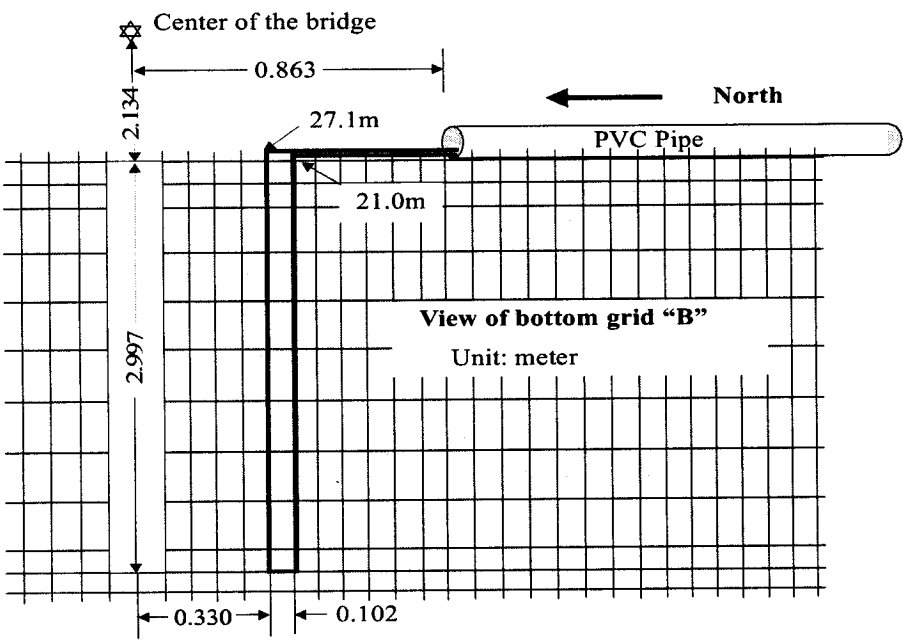

Figure 7.11 Layout of the optical sensing fiber "Loop A" under the bottom grid "B".

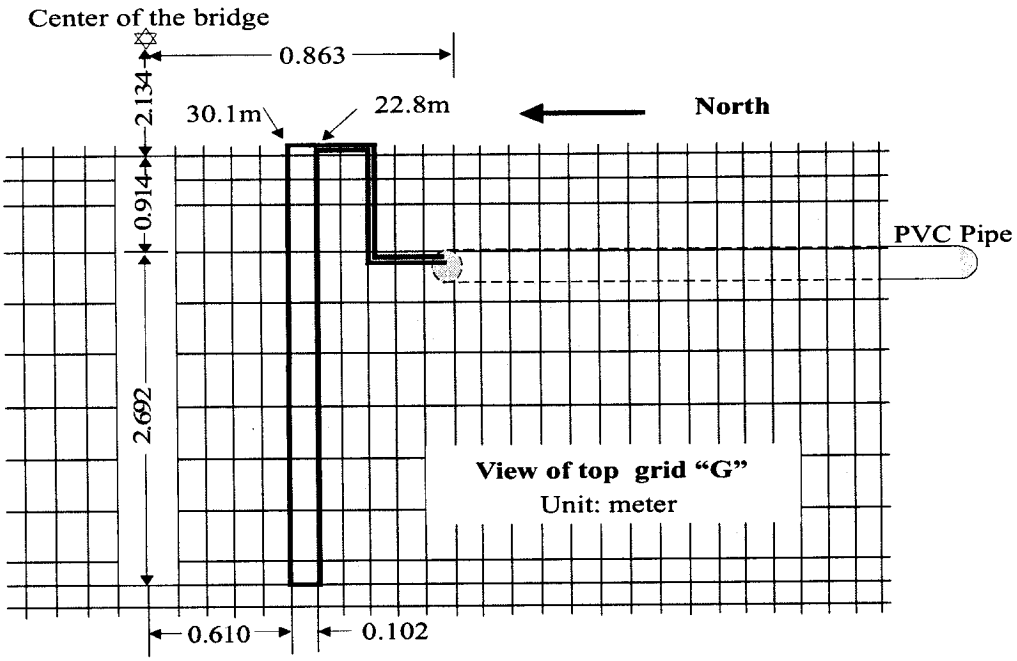

Figure 7.12 Layout of the optical sensing fiber "Loop B" on the bottom surface of the top bridge grid "G".

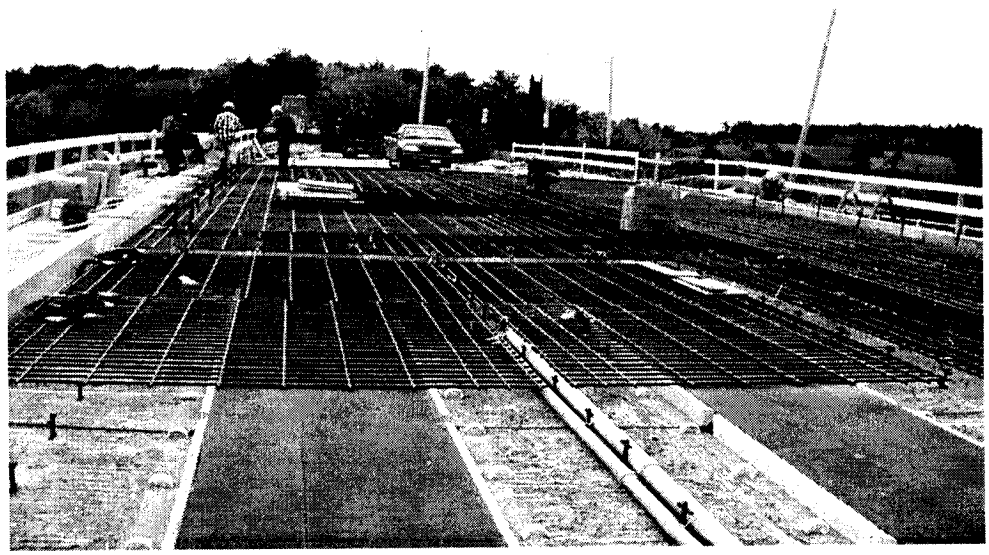

Figure 7.13 The CFRP grids and the PVC conduit were placed on the girders.

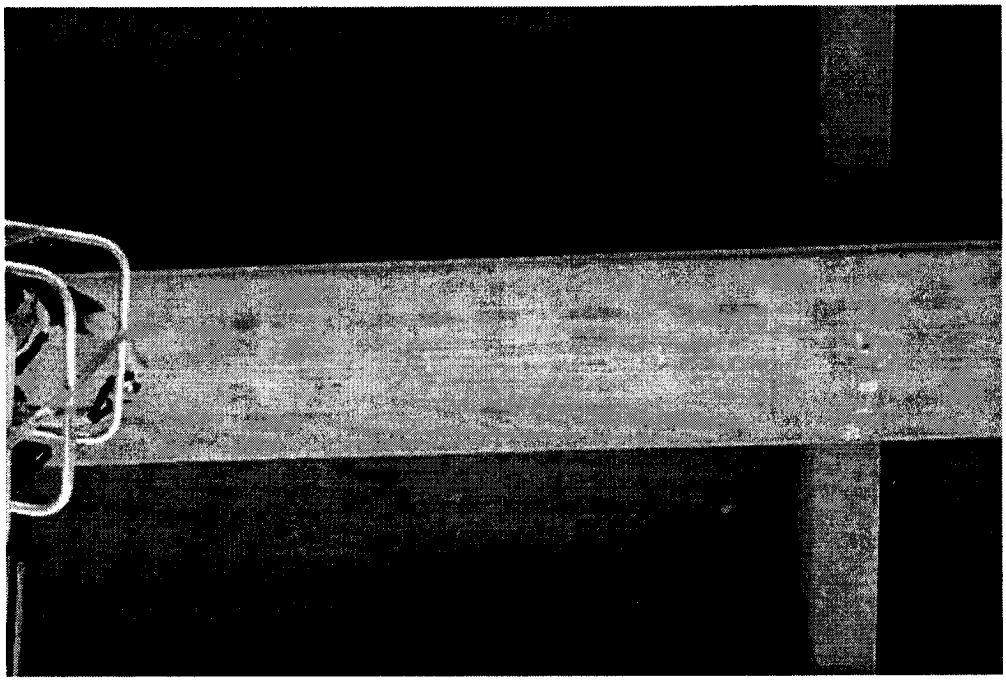

Figure 7.14 Bonding the Loop C optical fiber on the bottom surface of the bridge girder.

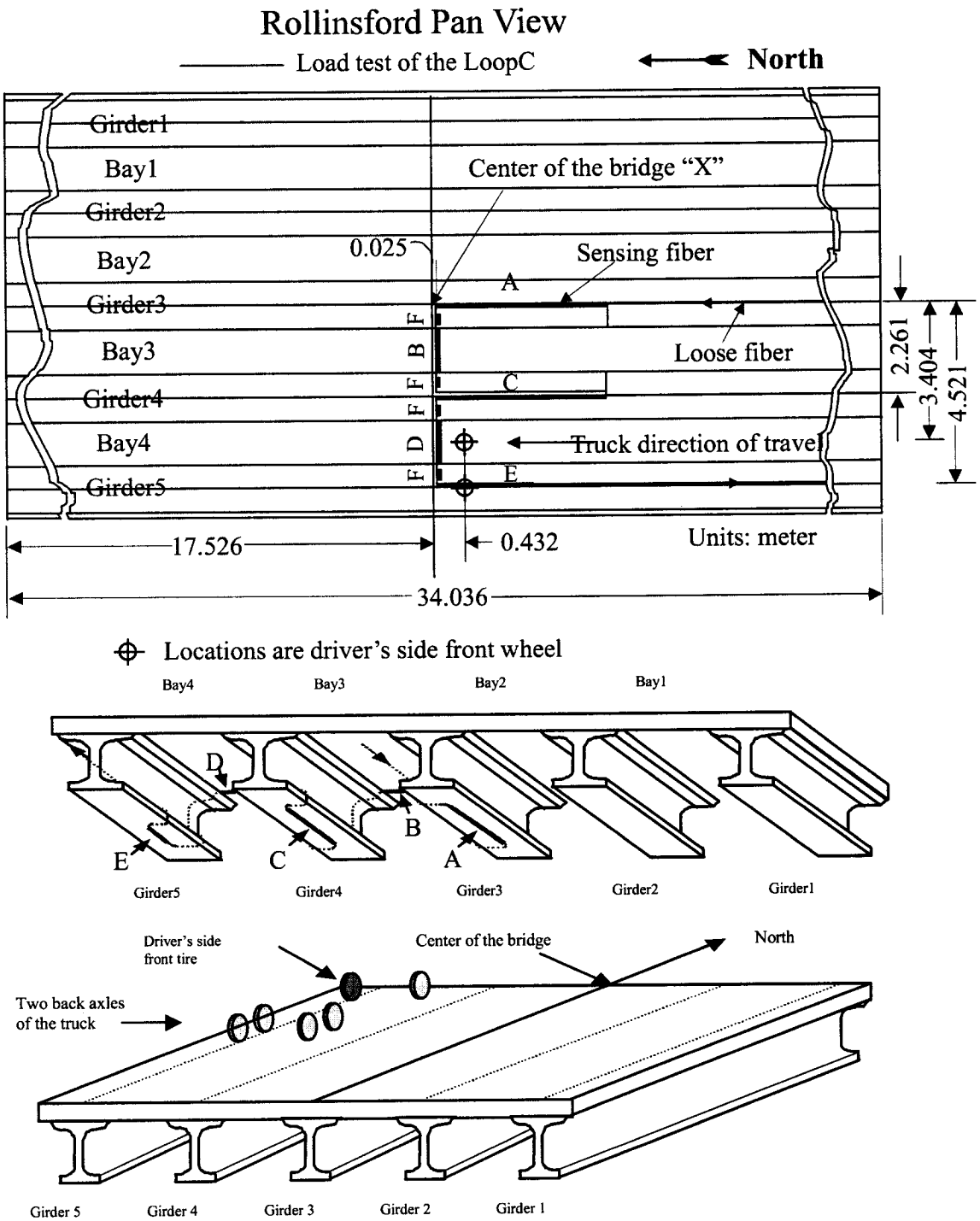

Figure 7.15 Layout of the optical sensing fiber Loop C and load method.

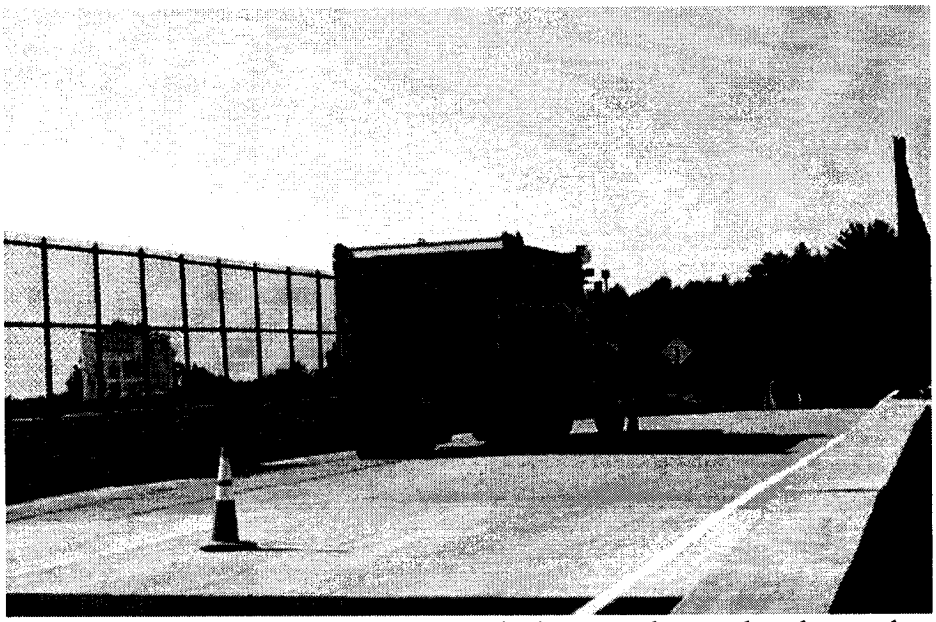

Figure 7.16 A 333.4kN (75kip) three-axle dump truck was placed at predetermined locations near the mid span of the bridge. The travel direction of the truck was north.

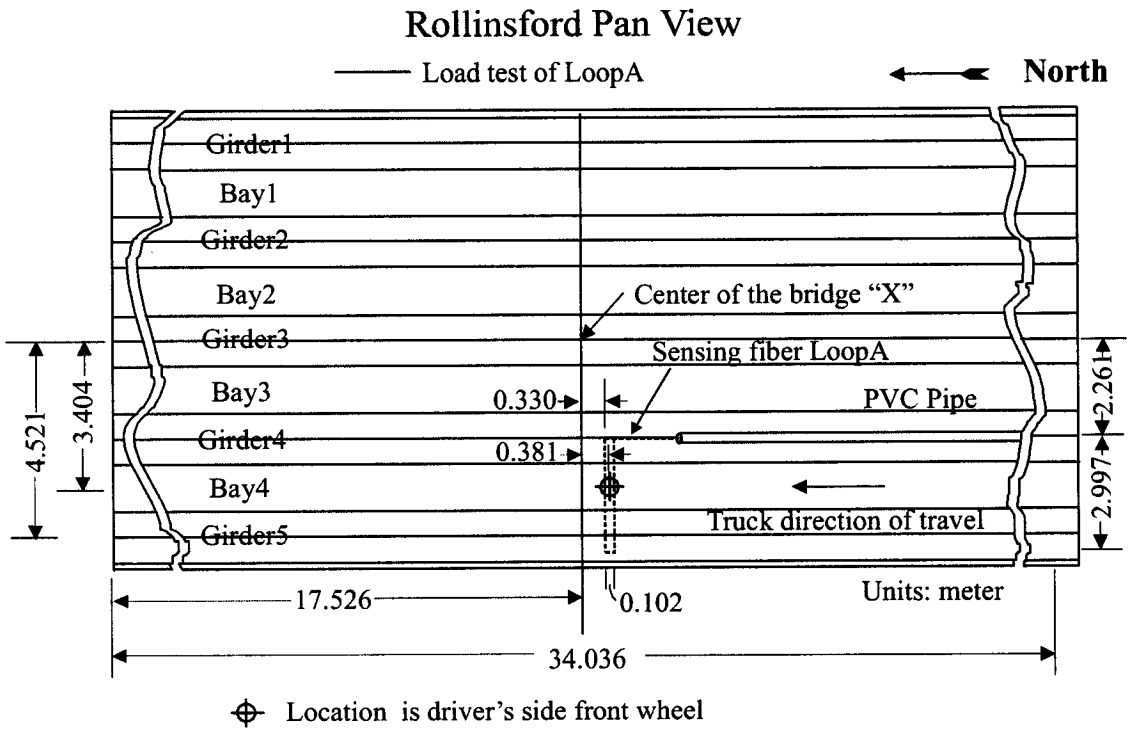

Figure 7.17 Layout of the optical sensing fiber Loop A and the location of the dump truck when the load test was applying.

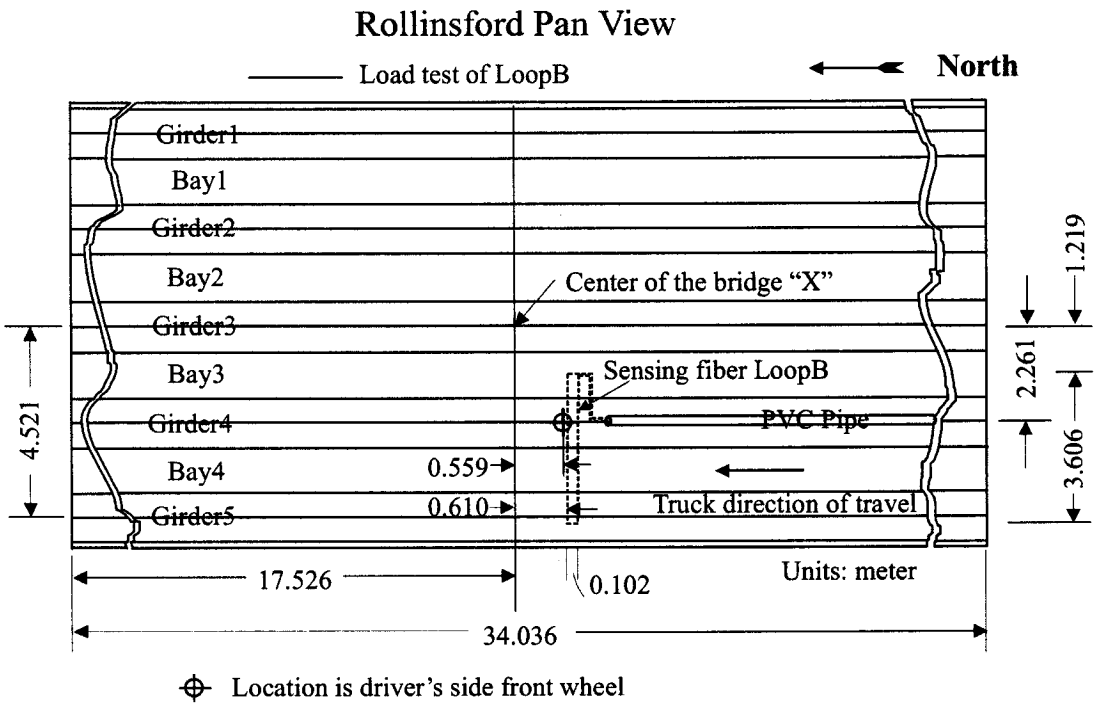

Figure 7.18 Layout of the optical sensing fiber Loop B and the location of the dump truck when the load test was applying.

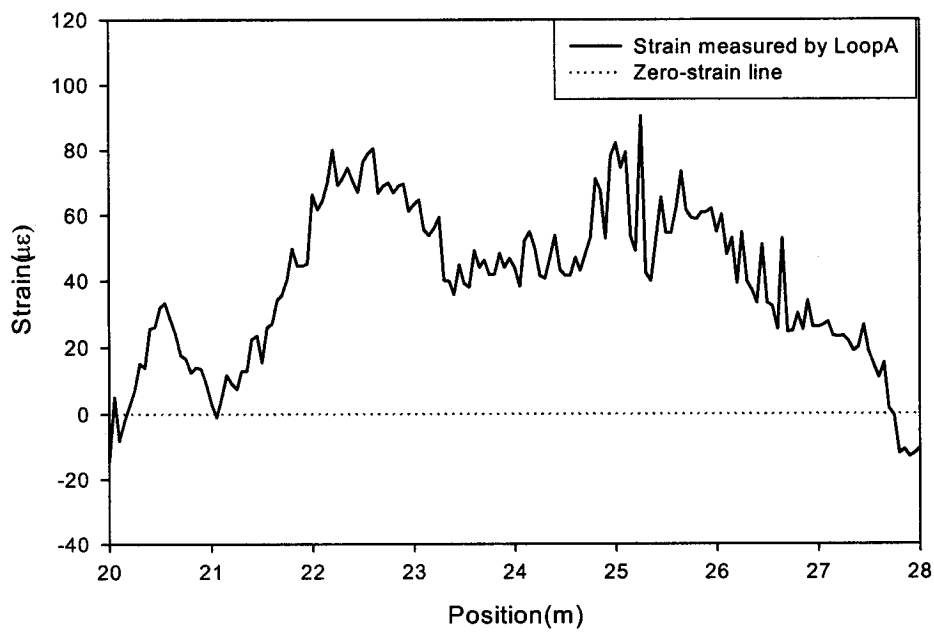

Figure 7.19 Relative strain difference versus positions along the sensing fiber Loop A

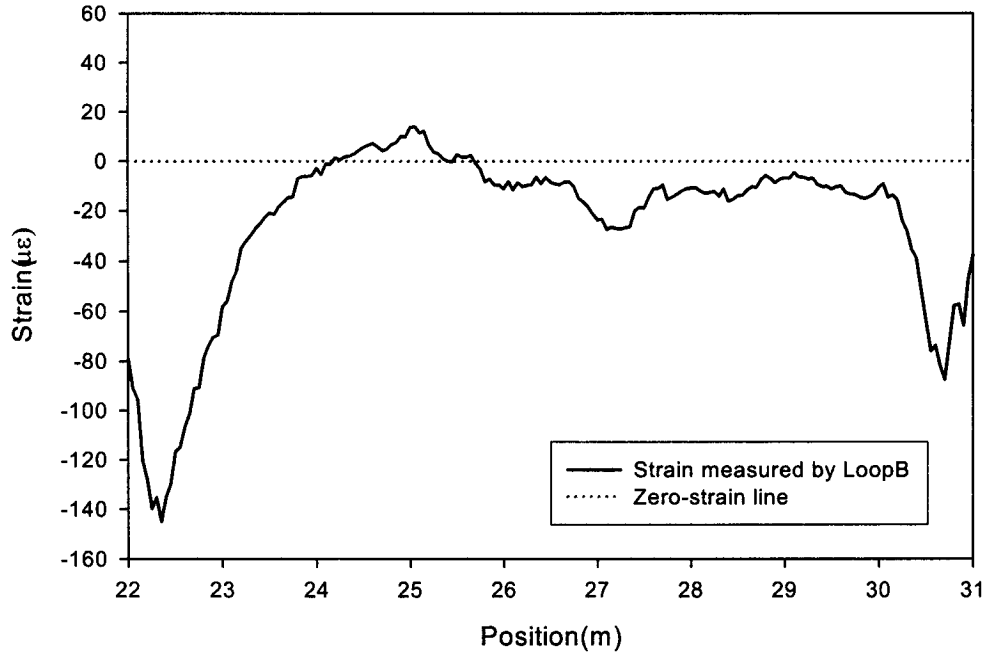

Figure 7.20 Relative strain difference versus positions along the sensing fiber Loop B

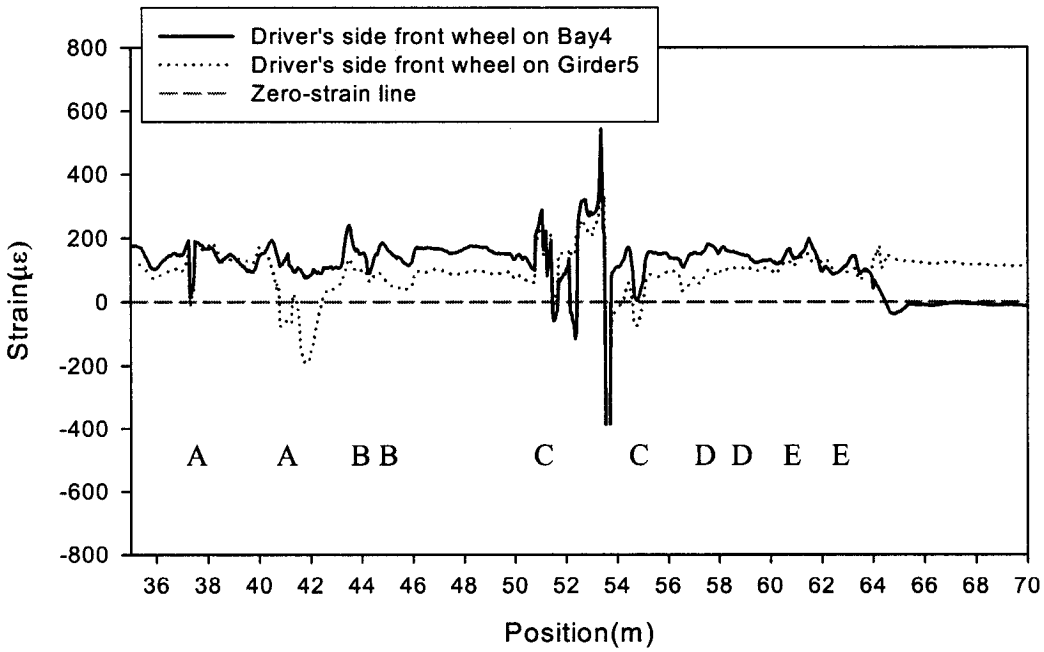

Figure 7.21 Relative strain difference versus positions along the sensing fiber Loop C

Chapter 8

Conclusion and Future Work

This thesis has presented the characterization and optimization of Brillouin scattering based distributed fiber optic sensing system and some of its applications both in laboratory and in the field.

8.1 Summary

To evaluate the performance of equipment or a measurement system, it is important to examine its measurement accuracy and repeatability. There are about 35 different user adjustable settings that can be used to configure the control software for a specific sensing application and would directly impact the performance of our distributed Brillouin sensing system. In Chapter 4, we have studied several parameters involving the pulse generation subsystem, such as, bias, leakage, PW voltage, pulsewidth, and repetition frequency. Bias is found to be the most important parameter. We also discussed the relationships between the repeatability of distributed Brillouin sensing system and parameters such bias, polarization states, averages and frequency lock methods.

In Chapter 5 and Chapter 6, we discussed two important applications of the distributed Brillouin sensing in the lab. Chapter 5 presents the strain measurement of a 1.65 m reinforced concrete beam using a Brillouin scattering based distributed fiber strain sensor with a 50 cm spatial resolution. The strain distribution has been measured for one-point and two-point loading patterns for optical fibers embedded in pultruded glass fiber reinforced polymer (GFRP) rods and those bonded to steel reinforcing bars. This experiment has successfully demonstrated the ability of the distributed Brillouin sensing system to measure strain at different locations along a concrete beam. Both methods, fiber embedded in GFRP rod and

fiber bonded to steel reinforcing bars, were found to effectively protect the optical fiber strand. The distributed fiber sensor strain resolution varied between ± (7 ~ 20) με depending on the fiber installation method and the strain gradient. The strain values measured from the optical fiber matched well with conventional strain gauge readings for the reinforced steel, while fibers embedded in GFRP rods worked well under uniform strain, but not so well under non-uniform strain.

In Chapter 6 the first in-situ measurement of in-plane stain variation during the curing process of AS4-3501 composite panels applied in the lab with distributed Brillouin sensing was demonstrated. In this experiment, the distributed Brillouin scattering technique was successfully applied to monitor the strain and temperature variation during the curing process of carbon fiber and epoxy composite materials. A signal processing and data analysis method was used to generate the net strain profiles at different stages of the cure process. The work has demonstrated that a 15 cm spatial resolution is capable to detect in-situ the relatively small strains associated with resin curing shrinkage during gelation and vitrification.

Applying the distributed Brillouin sensor in the field is our conclusive ambition for the application of this technique. Chapter 7 reports two successful field trials of our distributed Brillouin sensing system. The first application presents the preliminary results of strain and temperature monitoring of a nuclear containment structure with a distributed fiber optical sensor based on Brillouin scattering. Three single mode fiber loops were attached to the concrete structure to represent the strain and temperature variations versus time and locations. Two bare fibers served as strain sensor and the third fiber as the temperature reference sensor. The total length of the fiber was 1100 meters. The measurement is conducted continuously for 12 hours. Spatial resolution of 18 cm and strain resolution 50με has been achieved. This study shows that when the distributed Brillouin scattering sensor is used for long-term strain monitoring in the field, the temperature distribution as a function of time and position must be measured as a reference, so that the temperature contribution to Brillouin frequency can be subtracted from the strain distribution measurement. The choice of the glue to form the bond between the sensing fiber and the concrete structure is crucial for accurate strain reading of FRP/concrete. The thermal expansion coefficient of the glue should be smaller than the

FRP/concrete, so that the concrete structure rather than the glue contributes the major strain variations.

The second part of Chapter 7 reports the first temperature compensated strain measurement during the load testing of the Rollinsford Bridge with the distributed Brillouin sensing system. In this field application, three telecom single mode optical fibers were used to measure the strain variations in the bridge deck with and without loading. Temperature compensation was obtained through the measurement of loose fibers between the glued section and lead fibers. During load test a 333.4 kN (75 kips) three-axle dump truck was placed at predetermined locations near the mid span of the bridge. The strain distribution of the bridge deck as a function of the loading, location and time was monitored continuously during load tests of the bridge with a spatial resolution of 15 cm and a strain resolution of $\pm 25\mu\varepsilon$ ($\mu m/m$). In this experiment, DBS technique shows good ability to distinguish the complicated strain distribution in detail for a real bridge. For all three optical fiber loops, the maximum strain values achieved during load test were 80~200 $\mu\varepsilon$ much lower (< 2%) than the ultimate strain of FRP material (NEFMAC Technical Leaflet 2000). Through signal processing the strain measurement has been compensated for the temperature errors.

8.2 Future work

There are two main future works following the research of this thesis. They are further improvement and application of distributed Brillouin sensing system.

For improvement of DBS sensing, the further work will focus on: 1) switching the system from 1319 nm to 1550 nm due to lower prices of components and small volume, 2) packaging the distributed Brillouin sensing system into a portable unit that will be convenient for some special measurement and the field test, 3) optimization of the system including both hardware and software improvement, i.e., advanced components will save the time of measurement and raise the accuracy and stability of the system, as well rewriting some part of the software, 4) characterization of the system is on the way. Further investigation will quantify the influence

of other parameters, such as additional power control of the probe and pump lasers that are found impacting the performance of the system.

Utilization of new sensing media, such as PM fibers and Crystal fibers, for distributed Brillouin sensing could dramatically improve the accuracy of temperature and strain measurement. Outstanding properties and nonlinear effects make these fibers attractive for both engineers and researchers. It is believed that those fibers will improve the ability of DBS system.

Opening up new application realms is most important for distributed Brillouin sensing technique. By now most applications focus on civil engineering and aerospace industry. We are starting to use the distributed Brillouin sensing system to new fields, such as oil pipeline, fire detection, and defense safety. For the applications in civil engineering domain, the research is ongoing on the use of the distributed fiber optic sensing system to more effectively measure strain in smart structural applications with particular emphasis on cracked reinforced concrete flexural members. Special attention is being paid to minimize bond slippage and more work is being done to ensure more effective signal processing and data analysis.

Bibliography

[Afshaarvahid and Munch 2001] S. Afshaarvahid and J. Munch, "A transient, three-dimensional model of stimulated Brillouin scattering", *Journal of Nonlinear Optical Physics & Materials*, **10** (1) 2001.

[Agrawal 1995] Agrawal, G. P., *Nonlinear Fibre Optics*, 2nd ed., Academic Press, Boston pp. 1-59, 89-127, 238-306, 316-362, 370-399, 404-427 1995.

[Agrawal 1997] Govind P. Agrawal, *Fiber-Optic Communication Systems*, 2nd ed., John Wiley & Sons, Inc. 1997.

[Ansari and Yuan 1998] F. Ansari, and L. Yuan, "Mechanics of bond and interface shear transfer in optical fiber sensors", *Journal of Engineering Mechanics*, **124**, 385-394 1998.

[Bansal and Doremus 1986] Bansal, N. P. and Doremus, R. H., *Handbook of Glass Properties*, Academic Press, 1986.

[Bao, Webb and Jackson 1993a] Bao, X., Webb, D. J. and Jackson, D. A., "22-km distributed temperature sensor using Brillouin gain in an optical fiber", *Optics Letters*, **18** (7), 552-554 1993.

[Bao, Webb and Jackson 1993b] Bao, X., Webb, D. J. and Jackson, D. A., "32-km distributed temperature sensor based on Brillouin loss in an optical fiber" *Optics Letters*, **18** (18), 1561-1563 1993.

[Bao, Webb and Jackson 1994a] Bao, X., Webb, D. J. and Jackson, D. A., "22 km distributed strain sensor using Brillouin loss in an optical fiber" *Optics Communications*, **104**, 298-302 1994.

[Bao, Webb and Jackson 1994b] Bao, X., Webb, D. J. and Jackson, D. A., "Combined distributed temperature and strain sensor based on Brillouin loss in an optical fiber" *Optics Letters*, **19** (2), 141-143 1994.

[Bao et al. 1995] Bao, X., Dhliwayo, J., Heron, N., Webb, D. J. and Jackson, D. A., "Experimental and theoretical studies on a distributed temperature sensor based on Brillouin scattering" *Journal of Lightwave Technology*, **13**, 1340-1348 1995.

[Bao et al. 1999] Bao, X., Brown, A., DeMerchant, M. and Smith, J. "Characterization of the Brillouin loss spectrum of single mode fibre by use of very short (<10-ns) pulses," *Optics Letters*, **24**, 510-512 1999.

[Bao et al. 2001] X. Bao, M. DeMerchant, A. Brown, and T. Bremner, "Tensile and Compressive Strain Measurement in the Lab and Field with the Distributed Brillouin Scattering Sensor", *Journal of Lightwave Technology*, Vol. **19**, NO. 11, 1689-1704 2001.

[Bao, Huang and Zeng 2002] X. Bao, C. Huang, and X. Zeng, "Simultaneous strain and temperature monitoring of the composite cure with a Brillouin-scattering-based distributed sensor", *Optical Engineering*, **41** (7) 2002.

[Barnoski and Jensen 1976] Barnoski, M. K. and Jensen, S. M. "Fiber waveguides: A novel technique for investigating attenuation characteristics" *Applied Optics*, **15**, 2112-2115 1976.

[Bernini et al. 2002] R. Bernini, L. Crocco, A. Minardo, F. Soldovieri, and L. Zeni, "Frequency-domain approach to distributed fiber-optic Brillouin sensing", *Optics Letters*, **27** (5) 288-290 2002.

[Brown et al. 1998] Brown, A., DeMerchant, M., Bao, X., and Bremner. T., "Advances in distributed sensing using Brillouin scattering," in *Smart Structures and Materials 1998: Sensory Phenomena and Measurement Instrumentation for Smart Structures and Materials*, R.O. Claus, W.B. Spillman, Jr. Eds. *Proceedings of SPIE*, **3330**, 294-300 1998.

[Brown et al. 1999] Brown, A., DeMerchant, M., Bao, X. and Bremner, T., "Analysis of the precision of a Brillouin scattering based distributed strain sensor," *Proceedings of SPIE*, **3670** 359-365 1999.

[Brown et al. 2000] Brown, A., DeMerchant, M., Bao, X., and Steffen R. E., "Strain monitoring of the Rollinsford Bridge using distributed sensing", *Applications of Photonic Technology 4*, Roger A. Lessard, George A. Lampropoulos, Editors, *Proceedings of SPIE*, **4087**, 1149-1156 2000.

[Brown 2000] Anthony W. Brown, " Development of a Brillouin Scattering Based Distributed Fiber Optic Strain Sensor", Ph.D. Thesis, Physics Department, University of New Brunswick, Fredericton, NB. 2000.

[Chatfield 1978] C. Chatfield, *Statistics for technology*, 2nd ed., John Wiley & Sons, New York, 1978.

[Chen and Bao 1998] L. Chen and X. Bao, "Analytical and numerical solutions for steady state stimulated Brillouin scattering in a single-mode fiber", *Optics Communications*, **152** 65-70 1998.

[Chen et al. 1999] J. Y. Chen, S. V. Hoa, C. K. Jen, and H. Wang, "Fiber-optic and ultrasonic measurements for in-situ cure monitoring of Graphite/Epoxy composite", *J. Compos. Mater.*, **33** (20) 1860-1881 1999.

[Chhoa et al. 2001] C. Y. Chhoa, X. Bao, T. W. Bremner, A. W. Brown, M. D. DeMerchant, A.L. Kalamkarov, and A.V. Georgiades, "Strain Measurement in Concrete Structure Using Distributed Fiber Optic Sensing Based on Brillouin Scattering with Single Mode Fibers Embedded in Glass Fiber Reinforcing Vinyl Ester Rod and Bonded to Steel Reinforcing Bars", *Health Monitoring and Management of Civil Infrastructure Systems*, Steven B. Chase, A. Emin Aktan, eds., Proc. SPIE. **4337** 466-476 2001.

[Chiao et al. 1964] R. Y. Chiao, C. H. Townes, and B. P. Stoicheff, "Stimulated Brillouin scattering and coherent generation of intense hypersonic waves", *Physical Review Letter*, **12**, 592 1964.

[Crasto and Kim 1993] A. S. Crasto and Y. K. Kim, "On the determination of residual stresses in fiber-reinforced thermoset composites", *J. Reinf. Compos.* 12, 545-548 1993.

[Culverhouse et al 1989] Culverhouse, D., Farahi, F., Pannell, C. N. and Jackson, D. A., "Potential of stimulated Brillouin scattering as sensing mechanism for distributed temperature sensors" *Electronics Letters*, **25** (14), 913-915 1989.

[Cusano et al. 2001] A. Cusano, P. Salvarezza, G. Breglio, A. Cutolo, A. Calabro, M. Giordano, S. DeNicola, and L. Nicolais, " An integrated fiber optic sensing system for in situ characterization of the curing process of thermoset based composites", Smart Structures and Materials 2001: Sensory Phenomena and Measurement Instrumentation for Smart Structures and Materials, Eric Udd, Daniele Inaudi, Editors, Proceedings of SPIE, **4328,** 275-284 2001.

[Davis 1996] Christopher C. Davis, Lasers and Electro-Optics, Fundamentals and Engineering, Cambridge University, 1996.

[DeMerchant et al. 1998] DeMerchant, M., Brown, A., Bao, X., and Bremner. T. "Automated system for distributed sensing," in *Smart structures and Materials 1998: Sensory Phenomena and Measurement Instrumentation for Smart Structures and Materials*, R.O. Claus, W.B. Spillman, Jr. Eds. *Proceedings of SPIE*, **3330**, 315-322 1998.

[DeMerchant et al. 1998a] DeMerchant, M., Brown, A., Bao, X., and Bremner. T., "Distributed sensing for smart structures", in Proceedings of CanSmart Workshop Smart Materials and Structures, G. Akhras, ed., 71-80 Quebec, Canada, 1998.

[DeMerchant et al. 1999a] M. DeMerchant, A. Brown, X. Bao, and T. Bremner, "Structural monitoring by use of a Brillouin distributed sensor," *Applied Optics*, **38**, 2755-2759, 1999.

[DeMerchant et al. 1999b] DeMerchant, M., Brown, A., Bao, X. and Bremner, T. "Brillouin scattering based strain sensing", Proceeding of SPIE, **3670**, 352-358 1999.

[DeMerchant 2000] Michael D. DeMerchant, "Distributed Strain Sensing for Civil Engineering Applications", Ph.D. Thesis, Civil Engineering Department, University of New Brunswick, Fredericton, NB. 2000.

[DeMerchant et al. 2000a] M. DeMerchant, A. Brown, J. Smith, X. Bao, and T. W. Bremner, "Brillouin scattering based distributed sensing for civil structures," *Canadian J. Civil Engineering*, **27** (5) 2000.

[Dhliwayo, et al. 1996] Dhliwayo, J., Webb, D. J., and Jackson, D. A., "Statistical analysis of temperature measurement errors in a Brillouin scattering based distributed temperature sensor" in *Distributed and Multiplexed Fiber Optic Sensors VI*, A.P. Kersey and J. P. Dakin, eds., *Proceedings of SPIE,* **2838**, 276-283 1996.

[Faupel and Fisher 1997] J. H. Faupel and F. E. Fisher, *Engineering Design*, 2nd ed., p. 897, John Wiley and Sons, New York, 1997.

[Fellay, et al. 1997] Fellay, A., Thévenaz, L., Facchini, M., Niklès, M., and Robert, P., "Distributed sensing using stimulated Brillouin scattering: towards ultimate resolution" in *12th International Conference on Optical Fibre Sensors*, OSA Technical Digest Series **16**, 324-327 1997.

[Fotiadi et al. 2002] A. A. Fotiadi, R. Kiyan, O. Deparis, P. Mégret, and M. Blondel, "Statistical properties of stimulated Brillouin scattering in single-mode optical fibers above threshold", *Optics Letters*, **27** (2), 83-85 2002.

[Gaeta and Boyd 1991] Gaeta, A. L. and Boyd, R. W., "Stochastic dynamics of stimulated Brillouin scattering in an optical fiber," *Phys. Rev. A.,* **44** 3205-3209 1991.

[Garus, et al. 1997] Garus, D., Golgolla, T., Krebber, K., and Schliep, F., "Brillouin optical frequency-domain analysis for distributed temperature and strain measurements" *Journal of Lightwave Technology*, **15** (4), 654-662 1997.

[Ghafoori-Shiraz and Okoshi 1986] Ghafoori-Shiraz, H. and Okoshi, T., "Fault location in optical fibres using optical frequency domain reflectometry," *Journal of Lightwave Technology*, **4** (3), 316-322 1986.

[Gogolla and Krebber 2000] T. Gogolla and K. Krebber, "Distributed Beat Length Measurement in Single-Mode Optical Fibers Using Stimulated Brillouin-Scattering and Frequency-Domain Analysis", *Journal of Lightwave Technology*, **18** (3), 320-328 2000.

[Gysel 1990] P. Gysel, R. K. Staubli, "Statistical properties of Rayleigh backscattering in single-mode fibers", *Journal of Lightwave Technology*, **8**, 561 1990.

[Hartog 1983] Hartog, A.H., "A distributed temperature sensor based on a liquid-core optical fibre" *Journal of Lightwave Technology*, **1**, 498 1983.

[Horiguchi and Tateda 1989] Horiguchi, T. and Tateda, M., "Optical-fiber-attenuation investigation using stimulated Brillouin scattering between a pulse and a continuous wave" *Optics Letters*, **14**, 408-410 1989.

[Horiguchi et al. 1989] Horiguchi, T., Kurashima, T. and Tateda, M., "Tensile strain dependance of Brillouin frequency shift in silica optical fibers" *IEEE Photonics Technology Letters*, **1**, 107-108 1989.

[Horiguchi et al. 1992] Kurashima, T., Horiguchi, T., Izumita, H., Furukawa, S. and Koyamada, Y., "Brillouin optical-fiber time domain reflectometry," Proceedings of *the International Quantum Electronics Conference*, Vienna, 42-44. June 1992.

[Horiguchi et al. 1995] T. Horiguchi, K. Shimizu, T. Kurashima, M. Taleda, and Y. Koyamada, " Development of a distributed sensing technique using Brillouin scattering", *Journal of Lightwave Technology*, **13** 1296-1302 1995.

[Hotate and Hasegawa 1999] Hotate, K. and Hasegawa, T., "Measurement of Brillouin gain spectrum distribution along an optical fiber with a high spatial resolution using a novel correlation-based technique" in *13th International Conference on Optical Fiber Sensors*, Kyongju, Korea, *Proceedings of SPIE*, **3746**, 337-340 1999.

[Hotate and Tanaka 2001] K. Hotate and M. Tanaka, "Correlation-based continuous-wave techniques provide high spatial resolution for distributed fiber-optic sensing", *SPIE's Oemagazine* 36-40 2001.

[Hotate and Tanaka 2002] K. Hotate and M. Tanaka, "Distributed Fiber Brillouin Strain Sensing with 1-cm Spatial Resolution by Correlation-Based Continuous-Wave Technique," IEEE Photonics Technology Letters, **14** (2) 179-181 2002.

[Huang et al. 2001] C. Huang, X. Bao, X. Zeng, A. Arcand, and P. Lee-Sullivan, "Simultaneous temperature and strain monitoring of composite cure using a Brillouin-scattering-based distributed fiber optic sensor," *Smart Structures and Materials 2001: Sensory Phenomena and Measurement Instrumentation for Smart Structures and Materials,* Eric Udd, Daniele Inaudi, Editors, *Proceedings of SPIE*, **4328**, 70-78 2001.

[Johnston 2001] A. Johnston, *Private Communication*, Institute of Aerospace Research, National Research Council, Canada, 2001.

[Kaiser and Maier 1972] Kaiser, W. and Maier, M., *Laser Handbook*, Arecchi, F. T. and Schultz-Dubois, E. O. Eds., North-Holland, Amsterdam, Volume 2, 1972.

[Kalamkarov et al. 1998] A.L. Kalamkarov, H.Q. Liu, and D.O. MacDonald, "Experimental and analytical studies of smart composite reinforcement", *Composites Part B*, **29B**, 21-30 1998.

[Kee et al. 2000a] Kee, H. H., Lees, G. P., and Newson, T. P., "All-fiber system for simultaneous interrogation of distributed strain and temperature sensing by spontaneous Brillouin scattering" *Optics Letters*, **25** (10), 695-697 2000.

[Kee et al. 2000b] Kee, H. H., Lees, G. P., and Newson, T. P., "Technique for Measuring Distributed Temperature with 35-cm Spatial Resolution Utilizing the Landau-Placzek Ratio", *IEEE Photonics Technology Letters,* **12** (7), 873-875 2000.

[Kersey 1996] Kersey, A. D., "A review of recent developments in fiber optic sensor technology", *Optical Fiber Technology*, **2**, 291-317 1996.

[Kim et al 2001] Sang-Hoon Kim, Jung-Ju Lee, and Il-Bum Kwon, "Structural Monitoring of Bending Beam Using Brillouin Distributed Optical Fiber Sensors", in *Proceedings of Smart Materials and Structures*, Institute of Physics, UK Publications, 2001.

[Krohn 2000] David A. Krohn, *Fiber optic sensors: fundamentals and applications*, 3rd ed., the international society for measurement and control, 2000

[Kurashima et al. 1990a] Kurashima, T., Horiguchi, T. and Tateda, M., Thermal effects on the Brillouin frequency shift in jacketed optical silica fibers. *Applied Optics*, **29**, 2219-2222 1990.

[Kurashima et al. 1990b] Kurashima, T., Horiguchi, T. and Tateda, M., Distributed-temperature sensing using stimulated Brillouin scattering in optical silica fibers. *Optics Letters*, **15**, 1038-1040 1990.

[Kurashima et al. 1993] Kurashima, T., Horiguchi, T., and Izumita H., Furukawa S., and Koyamada Y., "Brillouin Optical-Fiber Time Domain Reflectometry", *IEICE TRANS. COMMUN.*, Vol. E76-B, No. **4**, 382-390 1993.

[Kurashima et al. 1997] T. Kurashima, T. Usu, K. Tanaka, A. Nobiki, M. Sato, K. Nakai, "Application of fiber optic distributed sensor for strain measurements in civil engineering" in *Smart Materials, Structures, and Integrated Systems*, Hariz, Ahsan; Varadan, Vijay K.; Reinhold, Olaf, eds., Proc. SPIE. **3241**, 247-258 Adelaide, Australia, 1997.

[Landau and Placzek 1934] L. D. Landau and G. Placzek, *Z Phys Sowjetunion*, 5, 172 1934.

[Lecoueche, et al. 2000] Lecoueche, V., Webb, D. J., Pannell, C. N. and Jackson, D. A., "Transient response in high-resolution Brillouin-based distributed sensing using probe pulses shorter than the acoustic relaxation time" *Optics Letters*, **25** (3), 156-158 2000.

[Lee and Chi 2000] C. C. Lee and S. Chi, "Measurement of Stimulated-Brillouin-Scattering Threshold for Various Types of Fibers Using Brillouin Optical-Time-Domain Reflectometer", *IEEE Photonics Technology Letters,* **12** (6), 672-674 2000

[Lee et al. 2001] C. C. Lee, P. W. Chiang, and S. Chi, "Utilization of a Dispersion-Shifts Fiber for Simultaneous Measurement of Distributed Strain and Temperature Through Brillouin Frequency Shift", *IEEE Photonics Technology Letters,* **13** (10), 1094-1096 2001.

[Lees, et al. 1997] Lees, G. P., De Souza, K., and Newson, T. P., "Novel optical fiber distributed temperature sensor based on the Landau-Placzec ratio" in *Proceedings of the 1997 Conference on Lasers and Electro-Optics*, 325 1997.

[LIGHTWAVE 1997] LIGHTWAVE Electronics, *Users manual of Diode-pumped fiber-coupled non-planar ring laser*, 48 1997.

[Liu et al. 2002] Z. Liu, G. Ferrier, X. Bao, X. Zeng, Q. Yu, A. Kim, "Brillouin Scattering Based Distributed Fiber Optic Temperature Sensing for Fire Detection" presented at 7th International Symposium on Fire Safety Science, Worcester, Massachusetts, USA, June 2002.

[Loayssa et al. 2001] A. Loayssa, D. Benito and M. J. Garde, "High-resolution measurement of stimulated Brillouin scattering spectra in single-mode fibers", *IEE Proc. Optoelectron.*, **148** (3), 143-148 2001.

[Maughan et al 2001a] S. M. Maughan, H. H. Kee, and T. P. Newson, "A Calibrated 27-km Distributed Fiber Temperature Sensor Based on Microwave Heterodyne Detection of Spontaneous Brillouin Backscattered Power", *IEEE Photonics Technology Letters,* **13** (5), 511-513 2001.

[Maughan et al 2001b] S. M. Maughan, H. H. Kee, and T. P. Newson, "57-km single-ended spontaneous Brillouin-based distributed fiber temperature sensor using microwave coherent detection", Optics Letters, **26** (6), 331-333 2001.

[Mijovic et al. 1993] J. Mijovic, J. M. Kenny, A. Maffezzoli, and F. Bellucci, "The principles of dielectric measurements for in situ monitoring of composite processing", *Composites Science & Technol.* **49** (3), 277-279 1993.

[Mufti et al. 1997] A. A. Mufti, G. Tadros, and P. R. Jones, "Field assessment of fiber-optic Bragg grating strain sensors in the Confederation Bridge", *Canadian Journal of Civil Engineering*, **24** (6), 963-966 1997.

[Niklès, et al. 1994] Niklès, M., Thèvenaz, L., and Robert, P. "Simple distributed temperature sensor based on Brillouin gain spectrum analysis" in *Proceedings of OFS'94*, Glasgow, Scotland, 138-141 1994.

[Niklès, et al. 1997] Niklès, M., Thèvenaz, L., and Robert, P., "Brillouin gain spectrum characterization in single-mode optical fibers," *Journal of Lightwave Technology*, **15** (10), 1842-1851 1997.

[NTT NEWS RELEASE 2001] NTT Information Sharing Laboratory Group, " New "distributed fiber optic strain sensor" about half the cost and providing three times the measurement accuracy of a conventional sensor", NTT, 2001.

[Ohno et al. 1999] Ohno, H., Uchiyama, Y., and Kurashima, T., "Reduction of the effect of temperature in a fibre optic distributed sensor used for strain measurements in civil structures" in *Smart Structures and Materials 1999: Sensory Phenomena and Measurement Instrumentation for Smart Structures and Materials*, R. O. Claus and W. B. Spillman, eds., *Proceedings of SPIE*, **3670**, 486-496 1999.

[Ohno et al. 2001] H. Ohno, H. Naruse, M. Kihara, and A. Shimada, "Industrial Applications of the BOTDR Optical Fiber Strain Sensor", Optical Fiber Technology, **7** 45-64 2001.

[Pannell et al. 1993] C. N. Pannell, St. J. Russell, and T. P. Newson, "Stimulated Brillouin scattering in optical fibers: the effects of optical amplification", *J. Opt. Soc. Am. B.* **4**, 684-690 1993.

[Pannell et al. 1998] C. N. Pannell, J. Dhliwayo, and D. J. Webb, "The accuracy of parameter estimation from noisy data, with application to resonance peak estimation in distributed Brillouin sensing", *Meas. Sci. Technol.* **9** 50-57 1998.

[Parker, et al. 1997] Parker, T. R., Farhadiroushan, M., Faceed, R., Handerek, V.A., and Rogers, A. J., "Temperature and strain dependance of the power level and frequency for spontaneous Brillouin scattering in optical fibers," *Optics Letters*, **22** (11), 787-789 1997.

[Parker, et al. 1998] Parker, T. R., Farhadiroushan, M., Faceed, R., Handerek, V. A., and Rogers, A. J., "Simultaneous distributed measurement of strain and temperature from noise-initiated Brillouin scattering in optical fibers" *IEEE Journal of Quantum Electronics*, **34** (4), 654-659 1998.

[Press et al. 1996] Press, W. H., Teukolsky, S. A., Vetterling, W. T. and Flannery, B. P., *Numerical Recipes in C: The Art of Scientific Computing*. Cambridge University Press, New York, 1996.

[Rich and Pinnow 1974] Rich, T. C. and Pinnow, D. A., "Evaluation of fiber optical waveguides using Brillouin spectroscopy," *Applied Optics*, **13** (6), 1376-1378 1974.

[Russell 1993] J. Russell, "Cure shrinkage of thermoset composites", *SAMPE Q.* 20, 28 1993.

[Shand 1958] E. B. Shand, *Glass Engineering Handbook*, The Maple Press Company, York 1958.

[Shimizu et al. 1993] Shimizu, K., Horiguchi, T., Koyamada, Y., and Kurashima, T., "Coherent self-heterodyne detection of spontaneously Brillouin scattered light waves in a single-mode fiber," *Optics Letters*, **18** (3), 185-187 1993.

[Siegman 1986] Anthony E. Siegman, *Lasers*, published by University Science Books, Mill Valley CA 1986.

[Smith 1972] R. G. Smith, "Optical power handling capacity of low loss optical fibers as determined by stimulated Raman and Brillouin scattering", *Applied Optics*, **11** 2489-2494 1972.

[Smith 1999] Smith, J., "Characterization of the Brillouin loss spectrum for simultaneous distributed sensing of strain and temperature" M.Sc. thesis, University of New Brunswick 1999.

[Smith et al. 1999a] Smith, J., Brown, A., DeMerchant, M., and Bao, X. "Simultaneous strain and temperature measurement using a Brillouin scattering based distributed sensor" in *Smart Structures and Materials 1999: Sensory Phenomena and Measurement Instrumentation for Smart Structures and Materials*, R.O. Claus, W.B. Spillman, Jr. Eds. *Proceedings of SPIE*, **3670**, 366-373 1999.

[Smith et al. 1999b] Smith, J., A. Brown, M. DeMerchant, and X. Bao, "Simultaneous Distributed Strain and Temperature Measurement," *Applied Optics*, **38** (25), 5372-5377 1999.

[Tang 1966] C. L. Tang, "Saturation and spectral characteristics of the Stokes emission in the stimulated Brillouin process", **37**, 2945-2955 1966.

[Tanaka and Hotate 2002] M. Tanaka and K. Hotate, "Application of correlation-Based Continuous-Wave Technique for Fiber Brillouin Sensing to Measurement of Strain Distribution on a Small Size Material", *IEEE Photonics Technology Letters*, **14** (5), 675-677 2002.

[Technical leaflet of AQ8602] Technical leaflet of AQ8602 Optical Fiber Strain/Loss Analyzer, KT-1699-2 9803 KL 230, Ando Electric Co., Ltd., Tokyo, Japan.

[Thévenaz, et al. 1998] Thévenaz, L., Niklès, M., Fellay, A., Facchini, M., and Robert, P., "Truly distributed strain and temperature sensing using embedded optical fibers" in *Smart Structures and Materials 1998: Sensory Phenomena and Measurement Instrumentation for Smart Structures and Materials*, R. O. Claus and W. B. Spillman, eds., *Proceedings of SPIE*, **3303**, 301-314 (1998).

[Udd 1991] Fiber optic sensors: An Introduction for Engineers and Scientists, Edited by Eric Udd, A Wiley-Interscience Publication, John Wiley & Sons, Inc.

[Udd 1995] Udd, E., "An overview of fibre-optic sensors" *Review of Scientific Instrumentation*, **66**, 4015-4030 1995.

[UTP 1997] Uniphase Telecommunications Products, Electro-optics Products Division, "Designer's Guide to External Modulation", 4–13 1997.

[Vanderlinde 1993] Vanderlinde, J., *Classical Electromagnetic Theory*, John Wiley & Sons, Toronto (1993).

[Wait and Newson 1996] Wait, C. P. and Newson, T. P., "Landau Placzek ratio applied to distributed fibre sensing" *Optics Communications*, **122**, 141-146 1996.

[Wait and Newson 1997] Wait, C. P. and Newson, T. P., "Reduction of coherent noise in the Landau-Placzec ratio method for distributed fibre optic temperature sensing" *Optics Communications*, **131**, 285-289 1997.

[Yariv 1984] A. Yariv and P. Yeh, Optical Waves In Crystals, New York: John Wiley & Sons, 1984.

[Zeng et al. 2002] X. Zeng, X. Bao, C. Y. Chhoa, T. W. Bremner, A. W. Brown, M. D. DeMerchant, G. Ferrier, A. L. Kalamkarov, and A. V. Georgiades, "Strain measurement in a concrete beam using the Brillouin scattering based distributed fiber sensor with single mode fibers embedded in GFRP rod and bonded to steel reinforcing bars", *Applied Optics*, **41** (24), 5105-5114 2002.

[Zeng et al. 2002a] X. Zeng, Q. Yu, G. Ferrier, and X. Bao, "Strain and temperature monitoring of a concrete structure using a distributed Brillouin scattering sensor", in *proceedings of the 1st International Workshop on Structural Health Monitoring of Innovative Civil Engineering Structures,* Winnipeg, Canada, in print 2002.

[Zeng et al. 2002b] X. Zeng, Q. Yu, G. Ferrier, X. Bao, R. E. Steffen, and M. Bowman, "Strain Measurement of the Load Test on the Rollinsford Bridge Using the Distributed Brillouin Sensor", in *proceedings of the 1st International Workshop on Structural Health Monitoring of Innovative Civil Engineering Structures,* Winnipeg, Canada, in print 2002.

Appendix A: Statistics (Index from SigmaPlot® User's Manual)

Mean

The arithmetic mean, or average, of all the cells in the column, excluding the missing values.

This is defined by: $\bar{x} = \frac{1}{n}\sum_{i=1}^{n} x_i$

Standard Deviation

The sample standard deviation is defined as the square root of the mean of the square of the differences from their mean of the data samples x_i in the column. Missing values are ignored.

$$s = \sqrt{\frac{i}{n-1}\sum_{i=1}^{n}(x_i - \bar{x})^2}$$

Standard Error

The standard error is the standard deviation of the mean. It is the sample standard deviation divided by the square root of the number of samples. For sample standard deviation s:

$$StdErr = \frac{s}{\sqrt{n}}$$

95% Confidence

The value for a 95% confidence interval. The end points of the interval are given by:

$$\bar{x} \pm t(v,z)\frac{s}{\sqrt{n}}$$

where $\bar{x}$ is the mean, s is the sample standard deviation, and $t(v,z)$ the t statistic for $v = n-1$ degrees of freedom and $z = 1.96$ standard normal percentile equivalent.

99% Confidence

The value for a 99% confidence interval. The end points for this interval are computed from the equation for the 95% confidence interval using $z = 2.576$.

Minimum

The value of the numerically smallest data value in the column, ignoring missing values.

Maximum

The value of the numerically largest data value in the column.

Appendix B: Strain/temperature error calculation

Normally, the errors incurred in measuring the center frequency of the spectrum are small [Smith 1999]. However, there are always some errors inherent in the process of fitting the test data to the theoretical profile. From the relationship

$$\begin{aligned} \nu_B &= \nu_{B0} + \frac{d\nu_B}{d\varepsilon}\cdot\varepsilon \\ \nu_B &= \nu_{B0} + \frac{d\nu_B}{dT}\cdot T, \end{aligned} \tag{B1}$$

we can obtain the new equations in strain yields

$$\begin{aligned} \varepsilon &= \frac{\nu_B - \nu_{B0}}{d\upsilon_B / d\varepsilon} \\ T &= \frac{\nu_B - \nu_{B0}}{d\upsilon_B / dT}. \end{aligned} \tag{B2}$$

The standard errors in the measurement of strain σ_ε/temperature σ_T are determined using [Chatfield 1978]

$$\begin{aligned} \sigma_\varepsilon &= [(\frac{1}{d\nu_B / d\varepsilon})^2(\sigma_B^2 + \sigma_{B0}^2) + (\frac{\nu_B - \nu_{B0}}{(d\nu_B / d\varepsilon)^2})^2\sigma_{d\nu\varepsilon}^2]^{1/2} \\ \sigma_T &= [(\frac{1}{d\nu_B / dT})^2(\sigma_B^2 + \sigma_{B0}^2) + (\frac{\nu_B - \nu_{B0}}{(d\nu_B / dT)^2})^2\sigma_{d\nu T}^2]^{1/2}. \end{aligned} \tag{B3}$$

where $\sigma_B, \sigma_{B0}, \sigma_{d\nu\varepsilon}$, and $\sigma_{d\nu T}$ are the standard errors in the Brillouin frequency measurement $\nu_B, \nu_{B0}, d\nu_B / d\varepsilon$, and $d\nu_B / dT$, respectively. For example, in a strain measurement, $\nu_B, \nu_{B0}, d\nu_B / d\varepsilon$, are 12900 MHz, 12800MHz, and 0.0564, respectively. σ_B, σ_{B0}, and $\sigma_{d\nu\varepsilon}$ are 0.22 MHz, 1.12 MHz, and 0.0002. From equation B3, the standard error of this measurement is obtained $o_\varepsilon \approx 21\mu\varepsilon$.